

SILICON CARBIDE ON INSULATOR  
QUANTUM PHOTONICS WITH COLOR CENTERS

A DISSERTATION  
SUBMITTED TO THE DEPARTMENT OF ELECTRICAL  
ENGINEERING  
AND THE COMMITTEE ON GRADUATE STUDIES  
OF STANFORD UNIVERSITY  
IN PARTIAL FULFILLMENT OF THE REQUIREMENTS  
FOR THE DEGREE OF  
DOCTOR OF PHILOSOPHY

Daniil Lukin

June 2022

© Copyright by Daniil Lukin 2022  
All Rights Reserved

I certify that I have read this dissertation and that, in my opinion, it is fully adequate in scope and quality as a dissertation for the degree of Doctor of Philosophy.

---

(Jelena Vučković) Principal Adviser

I certify that I have read this dissertation and that, in my opinion, it is fully adequate in scope and quality as a dissertation for the degree of Doctor of Philosophy.

---

(Olav Solgaard)

I certify that I have read this dissertation and that, in my opinion, it is fully adequate in scope and quality as a dissertation for the degree of Doctor of Philosophy.

---

(Amir Safavi-Naeni)

Approved for the Stanford University Committee on Graduate Studies

# Abstract

Color centers — crystal defects that act as artificial atoms trapped in the solid state — are contenders for realizing network-based quantum computation. An outstanding challenge has been the integration of color centers into scalable nanophotonic circuits, a prerequisite for efficient entanglement generation between the nodes of a quantum network. Silicon Carbide (SiC), a material traditionally used for abrasives, LEDs and transistors, has the potential to realize such circuits in a wafer-scale, CMOS-compatible platform. However, material fabrication challenges precluded the realization of high-quality SiC photonics. We overcome these limitations by developing new nanofabrication techniques and establish SiC as a high-performance classical photonics material. This development of classical photonic devices in SiC constitutes the first part of this dissertation. Then, we adapt the classical photonics techniques to fabricate devices that host coherent color centers, to demonstrate the basic building blocks of quantum networks based on color centers in SiC photonics. We isolate coherent single emitters in SiC photonic cavities, observe near-unity emitter-cavity cooperativity, and demonstrate superradiance of a pair of color centers in a single microresonator. Taken together, these results suggest that SiC is a candidate for closing the long-standing “classical-quantum photonics gap”, characterized by a large disparity between the excellent performance of classical photonic devices and comparatively non-scalable and inefficient performance of the quantum-photonic counterparts. In the final part of the dissertation, we discuss electrical control of single color centers in SiC, a key element of the realization of homogeneous, scalable qubits compatible with large-scale, foundry-fabricated color-center quantum circuits.

# Acknowledgments

First and foremost, I would like to thank my adviser Prof. Jelena Vučković. Jelena has been extremely caring and supportive throughout my entire PhD and I am very thankful for her mentorship. Throughout the journey, Jelena guided me and kept me on the right path, while allowing me to make many of my own decisions and mistakes (those mistakes, in fact, have been the most formative experiences). Jelena prioritizes her students' learning and well-being over raw research output of her group, (is that why the group has such great research output?). I am grateful for Jelena's trust, her willingness to help at any time, for always being understanding and supportive. I didn't know just how incredibly lucky I was when I first joined Jelena's research group.

I would like to thank the senior members of the Vučković group for their mentorship: Kevin Fischer and Rahul Trivedi for teaching me quantum optics theory; Constantin Dory for introducing me to quantum optics and nanophotonics experiments; Shuo Sun for his guidance in experiment, theory, and understanding current challenges in the field. I would also like to express a special thank you to Kiyoul Yang. Over the years, I have learned a great deal from Kiyoul both professionally and personally. I am grateful for Kiyoul's friendship and very excited for the next step in his career as he begins his own research group.

I would also like to express my gratitude to the member of the Vučković group who was my mentee for the past three years, Joshua Yang. Josh and I attempted the exploration of many an uncharted territory in the wild west of the nanofabrication facilities at Stanford. Out there, you need a partner you can rely on. I could always count on Josh if I needed help, and I hope I have been reliable to him as well. Josh is a very talented researcher, I

have learned a lot from him, and it has been a great pleasure to work together over the years. I am excited to continue our collaborations.

I am grateful for the stimulating discussions with many colleagues in the Vučković group, for working together side by side and helping each other overcome challenges: Alison Rugar, Daniel Riedel, Shahriar Aghaeimeibodi, Kasper Van Gasse, Sattwik Deb Mishra, Konstantinos Lagoudakis, Marina Radulaski, Hope Lee, Christopher Anderson.

I would also like to thank my collaborators outside of the Vučković group. I have learned a lot from you, and hope that our collaborations will continue. Working together has enabled projects that could not otherwise have been possible. Thank you Dr. Ashot Markosyan, Prof. Martin Fejer, Prof. Georgy Astakhov, Prof. Jörg Wrachtrup, Dr. Florian Kaiser, Dr. Naoya Morioka, Dr. Charles Babin, Di Liu, Dr. Öney O. Soykal, Prof. Jawad Ul-Hassan, Prof. Nguyen Tien Son, Dr. Takeshi Ohshima, Dr. Hiroshi Abe, Dr. Erick Romero, Leo Sementilli, Prof. Maxim Shcherbakov, Dr. Giovanni Sartorello, Dr. Natalie Piqué, Prof. Theodor Hänsch, Dr. Lucas Deniel.

All of my projects began (and some ended) in the nanofabrication cleanrooms at Stanford: The Stanford Nanofabrication Facilities (SNF) and the Stanford Nano Shared Facilities (SNSF). SNF and SNSF are amazing facilities because of the team of staff that run it. The staff at SNF and SNSF are extremely supportive of students' projects, and without their support, flexibility, and readiness to help many of my projects would not have been possible. I'd like to especially thank the staff who I have interacted with most during my time at Stanford: Mahnaz Mansourpour, Michelle Rincon, Phil Himmer, Xiaoqing Xu, Mike Dickey, Elmer Enriquez, Carsen Kline, Cliff Knollenberg, Lavendra Yadav Mandyam, Saeed Nejad, Gary Sosa, Maurice Stevens, Mary Tang, Uli Thumser, Rich Tiberio, Stanley Lin, Grant Shao, Jay Tower.

I am also grateful for the members of the SigmaCamp community, which I have been lucky to be part of for the past 10 years. At SigmaCamp we volunteer our time to teach and inspire a passion for STEM in the youngest generation. Whereas with respect to my research only time will tell if it will make a positive societal impact, I know for sure that what we do at SigmaCamp is valuable and important.

I would like to thank my family for their support, and for the upbringing without which I

wouldn't be pursuing a PhD. Finally, I would like to express my gratitude to my fiancée (and collaborator) Melissa Guidry. Life (and research) are meaningful because we go through it together.

# Contents

<b>Abstract</b>	<b>iv</b>
<b>Acknowledgments</b>	<b>v</b>
<b>1 Introduction</b>	<b>1</b>
1.1 Color centers . . . . .	2
1.2 Motivation for combining spin defects with photonics . . . . .	4
1.3 Optically-addressable spins in Silicon Carbide . . . . .	7
<b>2 Silicon Carbide on Insulator</b>	<b>15</b>
2.1 Previous approaches to SiC-on-Insulator . . . . .	15
2.2 SiCOI via grinding and polishing . . . . .	18
2.3 Measuring the absorption limit of bulk 4H-SiC . . . . .	20
2.4 Mask optimization for high-performance photonics . . . . .	21
2.5 Nonlinear photonics in SiC . . . . .	23
2.5.1 Second harmonic generation . . . . .	23
2.5.2 Optical parametric oscillation in SiC . . . . .	26
2.5.3 Low-power OPO and soliton generation in SiC . . . . .	30
2.6 Summary and outlook for SiC photonics . . . . .	32
<b>3 SiC quantum photonics</b>	<b>35</b>
3.1 Isolated defects in SiC-on-Insulator . . . . .	36
3.2 Purcell enhancement of single color centers . . . . .	36
3.2.1 $V_{\text{Si}}$ level structure and Purcell factor analysis . . . . .	40

3.2.2	Numerical fit for $g^{(2)}(\tau)$ . . . . .	41
3.3	Optically-coherent color centers in thin-film photonics . . . . .	42
3.3.1	Device fabrication . . . . .	43
3.3.2	Experimental setup . . . . .	44
3.3.3	Purcell enhancement of coherent $V_{\text{Si}}$ emitters . . . . .	46
3.3.4	Approaching cooperativity of unity in SiC . . . . .	50
3.4	Photon interference between two SiC color centers . . . . .	52
3.4.1	Two-emitter single photon interference modeling . . . . .	57
3.4.2	Entanglement protocol between two emitters with $\phi = \pi/2$ . . . . .	59
3.4.3	Spin selective temporally-filtered resonance fluorescence . . . . .	61
<b>4</b>	<b>Electrical control of the <math>V_{\text{Si}}</math></b> . . . . .	<b>63</b>
4.1	Experimental setup . . . . .	64
4.2	DC Stark shift . . . . .	65
4.3	Observation of Floquet states under AC drive . . . . .	68
4.3.1	Spectral stability under AC drive . . . . .	69
4.4	Two-photon scattering from a modulated two-level system . . . . .	71
4.5	Signature of ground state interference in $g^{(2)}(\tau)$ . . . . .	73
4.5.1	Observation of interference of multiple ground states via $g^{(2)}$ . . . . .	74
4.6	All-optical orbital control of the $V_{\text{Si}}$ under AC modulation . . . . .	75
4.6.1	Experimental details . . . . .	77
<b>5</b>	<b>Conclusions and outlook</b> . . . . .	<b>79</b>
5.1	Optimizing the single quantum node . . . . .	79
5.2	Scaling-up quantum photonic processors . . . . .	83
5.3	Prospects for monolithic frequency conversion and photonic reconfigurability . . . . .	88
5.4	Perspective on fully-integrated quantum photonics . . . . .	90
5.5	Conclusion . . . . .	92
	<b>Bibliography</b> . . . . .	<b>93</b>

# List of Tables

- 1.1 Optically-addressable spin defects in SiC . . . . . 8
- 2.1 Intrinsic optical loss of HPSI 4H-SiC . . . . . 21
- 2.2 Comparison of integrated soliton device performance . . . . . 30

# List of Figures

1.1	<b>Bound states in an atomic defect.</b> (a) Diagram of an F-center in NaCl. (b) The F-center ground state: A trapped electron. (c) The excited state: An electron-hole pair has eigenstates similar to that of a hydrogen atom with a modified effective mass and charge. (d) Diagram of a Silicon Vacancy ( $\text{SiV}^-$ ) in diamond. The 10 bound valence electrons contributed by the the carbon atoms and the silicon atom, as well as an additional electron acquired from the environment, form a 11-electron state, shown in (e). Figure reproduced from [188] . . . . .	3
-----	---	---

1.2	<b>Quantum photonics with optically-addressable spins.</b> (a) A suitable defect features a spin-selective optical transition, where a photon degree of freedom (i.e. polarization, frequency, or time-bin) is entangled with a ground-state spin featuring a long coherence time. The defect’s optical lifetime is determined by the magnitude of its optical dipole moment, which in turn is dictated by the orbital structure of the excited and ground state. (b) A quantum photonic network consists of multi-qubit registers, each consisting of an optically-addressable electron spin strongly-coupled to nearby nuclear spins. The registers are integrated together in a network via an efficient waveguide or fiber interface. The network is equipped with beamsplitters and switches (which may be one and the same depending on the implementation) for long-distance entanglement and circuit reconfigurability. Low losses at all stages (including efficient photon collection from the defect, low-loss photon propagation in waveguide, and high detector efficiency) are essential for fault-tolerant computation, efficient quantum simulation, and long-distance quantum communications. (c) Due to the weak confinement of optical photons in dielectric structures, light from a quantum emitter does not couple efficiently to a simple dielectric waveguide. Instead, a nanophotonic cavity or a slow-light waveguide mode must be used to enhance the emission into the waveguide mode via the Purcell effect. Orbital graphic in (a) adapted from [131] . . . . .	5
1.3	<b>Optically-active spins in SiC.</b> The 4H-SiC crystal lattice, showing the inequivalent configurations of the divacancy, silicon vacancy ( $V_{Si}$ ), and chromium ion. . . . .	9
1.4	<b>The silicon vacancy (<math>V_{Si}</math>) in SiC.</b> The spin-1/2 manifold and spin-3/2 manifold emit at different frequencies. In the diagram, the transition emission wavelength is represented by the color (red or blue), although the actual frequency difference of the optical transitions is very small ( emission lines spectrally separated by just 1 GHz). . . . .	10

1.5	<b>The illustration of a cluster-state generation protocol.</b> If prepared in the $1/2$ ( $3/2$ ) ground state, upon excitation with an above-resonant laser, the $V_{Si}$ will emit a blue (red) photon. If the ground state is prepared in a spin-state superposition, the photon will be a superposition of red and blue. By repeatedly exciting the $V_{Si}$ while applying a ground state gate after each emission, a variety of chains of entangled photons, such as the cluster state, can be generated [47] . . . . .	11
1.6	<b>Electronic fine structure model and intersystem crossing mechanism of the <math>V_{Si}</math>.</b> The radiative decay rates for both spin- $3/2$ and $-1/2$ channels are labeled as $\gamma_r$ . The ground and excited state ZFS are given by $D_g$ and $D_e$ , respectively. Additional potential spin relaxation processes between allowed doublets (via spin-orbit coupling) are shown by circular arrows. Dashed and solid black arrows correspond to ISC channels assisted by the longitudinal and orthogonal components (with respect to the $c$ -axis) of the spin-orbit coupling and optical emission polarization. . . . .	13
2.1	<b>Three approaches to preparing the SiCOI material platform.</b> (i) Ion slicing (known by its trademark name SmartCut) produces uniform thin films with thickness limited by the stopping range of hydrogen ions, as dictated by the ion energy. However, losses are significant due to the absorption from implantation-induced crystal defects. (ii) Direct growth of 3C-SiCOI via heteroepitaxy on silicon can produce arbitrary thickness uniform films, but lattice mismatch results in poly-crystalline films. (iii) The grind-and-polish method can be used to produce SiC with pristine crystal quality, but results in non-uniform thickness on the wafer scale. <i>Figure reproduced from [112].</i> . . .	17
2.2	<b>Images of the thin films fabrication process on a die-scale.</b> (a) $10 \times 10$ mm SiC dies bonded to the thermally-oxidized silicon wafer. (b) The wafer after thinning and polishing, with films approximately $15 \mu\text{m}$ thick. (c) Close-up image of one die after reactive-ion etch thinning (thickness approximately $1 \mu\text{m}$ ). The non-uniformity arising from edge effects is clearly visible. (d) A $3 \times 3$ mm chip after device fabrication. . . . .	19

2.3	<b>Measurement of the intrinsic loss of 4H-SiC.</b> (a) Diagram of the PCI measurement setup, described in detail in Ref. [120]. (b) A crystal of 4H-SiC with dimensions of $5 \times 5 \times 10$ mm undergoing the measurement. Multiple reflections of the red probe laser inside the crystal are visible. . . . .	22
2.4	<b>Microring resonators and inverse-designed vertical couplers in 4H-SiC-on-insulator.</b> (a) A scanning electron micrograph (SEM) of two SiC microring resonators (false-colored) with diameters of 55 $\mu\text{m}$ and 100 $\mu\text{m}$ before $\text{SiO}_2$ encapsulation. (b) A schematic of the device cross-section after $\text{SiO}_2$ encapsulation. (c) Transmission spectrum of a ring with diameter 100 $\mu\text{m}$ , width 3.0 $\mu\text{m}$ , and height 530 nm, around a $\text{TE}_{00}$ resonance with an intrinsic Q of $1.1 \cdot 10^6$ and loaded Q of $9.7 \cdot 10^5$ . The wavelength is relative to 1532 nm. (d) A close-up SEM image of the inverse-designed vertical coupler, highlighted in (a). The coupler converts a near-diffraction-limited free-space Gaussian beam (focused via a 50x objective with $\text{NA} = 0.5$ ) into the fundamental waveguide mode. (e) Camera image of the coupler operating at peak efficiency, showing little back-reflection from the input coupler, and a nearly-Gaussian beam at the output. (f) We measure the single-mode coupling efficiency to be 31% at the target wavelength of 1550 nm, in close agreement with finite-difference time domain (FDTD) simulation. The interference fringes observed in experiment are attributed to back-reflection in the couplers. . . . .	24

2.5	<b>Efficient second-order frequency conversion in microring resonators.</b>	
	<p><b>a</b> SEM of a ring resonator designed for second-harmonic generation. The fundamental <math>TE_{00}</math> mode at 1555 nm is converted to a <math>TM_{20}</math> mode at 777.5 nm, and coupled out via a single-mode, effective index-matched waveguide. Inset: Optical image of the second-harmonic out-coupled via an inverse-designed vertical coupler (ring outline is overlaid for clarity). <b>b</b> Numerical simulation of the phase-matching condition for the 1555 nm <math>TE_{00}</math> and the 777.5 nm <math>TM_{20}</math> modes, demonstrating mode-matching for a waveguide width of 560 nm. Inset: Simulated mode profiles. <b>c</b> Dependence of second-harmonic power in the output waveguide on the pump power in the input waveguide. A quadratic fit reveals a conversion efficiency of <math>360\% \text{ W}^{-1}</math>. Inset: The second-harmonic signal imaged on a spectrometer. . . . .</p>	26
2.6	<b>Microcomb formation in a 4H-SiC microring.</b>	
	<p>(a) Measured integrated dispersion (green points) of the <math>TE_{10}</math> mode versus the relative mode number <math>\mu</math>, where <math>\mu = 0</math> corresponds to the pump mode. The orange curve is a numerical simulation, from which we extract <math>D_2/2\pi = 61 \text{ MHz}</math> and <math>D_3/2\pi = -0.01 \text{ MHz}</math>. Center inset: Close-up of the measured dispersion datapoints. Left inset: Numerical simulation of the <math>TE_{10}</math> mode cross-section. (b) Measured OPO spectra (blue) at different injected powers, featuring three distinct stages in the microcomb formation. A <math>\text{sech}^2</math> fit (red envelope) is overlaid onto the chaotic frequency comb for comparison to the characteristic soliton spectral shape. Simulation (red) of the soliton. . . . .</p>	28

- 2.7 **Sub-mW parametric oscillation threshold power** (a) SiC parametric oscillation induced by pumping at the wavelength of 1553.3 nm. Top panel shows OPO just above the threshold power (510  $\mu$ W total power in the waveguide). Middle and lower panels show measured optical spectra with loaded pump power of approximately 570 and 600  $\mu$ W, respectively. (b) High-resolution scan of the fundamental TE mode with a loaded (intrinsic) quality factor of 3.19 (5.61) million. The mode is seen to be nearly critically-coupled to the waveguide. The scan laser wavelength is calibrated using a wavemeter, and the red curve is a fit to a Fano lineshape. The asymmetry of the resonance shape is attributed to interference with back-reflection of the vertical couplers. . . . . 29
- 2.8 **SiC soliton microcomb** (a) The optical spectrum of a single soliton state with 2.3 milliwatts operation power. (b) RF spectrum (resolution bandwidth = 100 kHz) of the entire soliton comb confirms a low-noise state, compared to the non-locked modulation instability (MI) state. (c) Measured frequency dispersion belonging to the soliton forming mode family ( $TE_{00}$ ) is plotted versus the relative mode number. The red curve is a fit using  $D_1/2\pi = 358.663$  GHz and  $D_2/2\pi = 8$  MHz. Simulation of the soliton mode families is plotted (green curve), and the simulation fairly agrees with the measurement results. (d) Upper panel presents pump power transmission versus tuning across a resonance used for the soliton formation. Lower panel shows comb power trace in which the pump laser scans over the resonance from the short wavelength (blue detuned) to the long wavelength (red detuned). The shaded region (orange) depicts the spectral region where the single soliton exists. . . 31

2.9	<b>Timeline of the first decade of SiC photonics.</b> The first demonstration of a SiC photonic device using the Smart Cut approach with 6H-SiC [176]. Soon after, suspended resonators in 3C-SiC-on-Si were demonstrated [29]. Strong intrinsic absorption of low quality Smart Cut and heteroepitaxial 3C films was hypothesized to limit the achievable Q-factors. Using thicker 3C-SiC epilayers or thinning down bulk-crystal 4H-SiC, enabled record Q factors in 3C-SiC [56, 57], ultra-high Q PhCs [174], and low-loss 4H-SiC-on-Insulator waveguides [110]. Devices with Q factors exceeding $10^6$ were shown, enabling the demonstration of optical parametric oscillation and microcomb formation [67]. Reproduced from [176, 29, 57, 174, 110, 67] . . . . .	32
2.10	<b>SiC photonics demonstrations: Q-factor metric over the years.</b> Each reference is categorized by the SiC polytype (4H, 6H, or 3C); type of resonator (WGM - whispering gallery mode resonator, PhC - photonic crystal cavity, wg - waveguide, or ring resonator); and whether the resonator is coupled to color centers (quantum), or not (classical). Circled in black are the demonstrations presented in this dissertation. The following references are presented in the chart: Song 2011 [176]; Cardenas 2013 [29]; Radulaski 2013 [148]; Yamada 2014 [211]; Lu 2014 [107]; Cardenas 2015 [28]; Clausine 2016 [27]; Bracher 2017 [21]; Song 2018 [175]; Fan 2018 [56]; Zheng 2020 [223]; Song 2019 [174]; Lukin 2019 [110]; Crook 2020 [38]; Powell 2020 [147], Fan 2020 [57]; Guidry 2020 [67]; Wang 2021 [198]; Guidry 2022 [66]; Cai 2022 [26]; Lukin 2022 [113].	33
2.11	<b>Wafer-scale SiC-on-Insulator using photoelectrochemical etching.</b> . . . . .	34
3.1	<b>Photoluminescence spectra of color centers in pillars fabricated in 4H-SiCOI;</b> $h$ - $V_{Si}$ ( $V1'/V1$ ) and $k$ - $V_{Si}$ ( $V2$ ) show narrow linewidths and low-intensity phonon sidebands. Insets: Scanning electron micrograph (SEM) of micropillars and corresponding material stack. . . . .	37

3.2	<b>Light-matter interaction of a single color center with a nanophotonic resonator.</b> <b>a</b> SEM of a suspended nanobeam array and close-up image of the devices from above. <b>b</b> Stacked spectra while tuning a nanobeam photonic crystal cavity resonance via gas condensation through the V1'. Individual color centers are indicated via 1-4. Inset: While tuning the cavity resonance through V1, we observe minimal enhancement of V1, which confirms that the dipole moment of the transition is orthogonal to the TE mode of the cavity. <b>c</b> Lifetime measurements with the cavity on- and off-resonance. Fitted lifetimes are $\tau_{\text{off}} = 6.66$ ns and $\tau_{\text{on}} = 2.45$ ns. <b>d</b> Spectra extracted from <b>b</b> with the cavity off- and on-resonance with V1'. <b>e</b> Second-order correlation measurement with the cavity on-resonance with the V1' transition of a single emitter, revealing $g^{(2)}(0) = 0.08$ . . . . .	38
3.3	Level diagram of the $V_{\text{Si}}$ , showing the decay channels of the V1 and V2 transitions. Detailed theoretical analysis of the levels is presented in [45] . . .	40
3.4	A plot of $ E(k_x, k_y) ^2$ (Normalized such that $\int  E(k_x, k_y) ^2 dx dy = 1$ ), where $E(k_x, k_y)$ is the Fourier transform of the electric field just above the nanobeam cavity <b>a</b> off-resonance and <b>b</b> on-resonance. The light line ( $k_x^2 + k_y^2 = \omega^2/c^2$ ) is represented as a dashed line. These simulations indicate that while on-resonance, most of the field above the cavity lies outside of the light cone and thus does not contribute to the power collected by the objective. While off-resonance, the relative amount of power inside the light cone is higher, resulting in a larger collection efficiency. <b>c</b> The collection efficiency for a lens with an NA of 0.9 as a function of dipole-cavity detuning. . . . .	41
3.5	<b>Device fabrication process flow.</b> Colors correspond to materials as follows. Blue: SiC substrate. Light blue: SiC epitaxy. Grey: Si substrate. Orange: HSQ. Green: hardmask. Yellow: photoresist. . . . .	43

3.6	<b>Experimental setup.</b> (a) Diagram of optical paths, laser sources, and detectors. (b) Optical microscope image of a row of disk resonators (three resonators are visible), taken using a commercial optical microscope. (c) Optical image of a single device under illumination as seen through the cryostat objective. (d) Optical image of the device without illumination and laser light coupling into the left waveguide facet, passing through the waveguide and emitting from the right waveguide facet. . . . .	45
3.7	<b>Gas tuning and saturation of photon detection rate.</b> Photon detection rate in a 20 nm spectral window (910-930 nm) around the $V_{Si}$ ZPL during continuous red-tuning of the microdisk resonance wavelength via gas condensation. The Purcell enhancement condition is observed as a sharp peak in time. Smaller peaks correspond to weaker coupling to other detuned emitters. Excitation is performed with a 730 nm, 80 MHz repetition rate femtosecond laser (0.79 mW power measured before the objective). Inset shows background-subtracted peak ZPL photon detection rate for varying laser power.	47
3.8	<b>Spectrally-stable <math>V_{Si}</math> emitters in integrated 4H-SiCOI photonics.</b> (a) Scanning electron micrograph of the device. A waveguide, which wraps around the disk (seen in the optical microscope image, inset), is coupled to the resonator. A microscope objective is used to couple light to and from the flat facets of the waveguide. (b) A cavity photoluminescence spectrum (emitter PLE spectrum) in black (green), taken with a scanning resonant laser with 1.5 $\mu$ W (0.5 pW) of power in the waveguide. We extract a loaded cavity quality factor of $Q = 1.3 \cdot 10^5$ . The prominent peaks at 2.7 and 4.5 GHz detuning are the $A_2$ transitions of the two emitters. The corresponding $A_1$ transitions are labelled with arrows. In this figure and the rest of this chapter, the laser detuning is relative to 327.113 THz (916.5 nm). (c) Lifetime measurements for emitter A (blue) and emitter B (red) on- and off-resonance with the cavity. The gray region represents the excitation pulse. (d) A 1-hour PLE scan of each emitter (while the other is selectively ionized into the dark state), with the cavity positioned on-resonance with the emitter. . . . .	48

3.9	<b>Emitter linewidths on- and off-resonance with the cavity.</b> (a) A continuous PLE scan of the two emitters with the cavity far-detuned. (b) A histogram of fitted single-scan linewidths. Indicated in the figure is the mean fitted linewidth and its standard error. (c) Histogram of time-averaged scans for PLE data presented in Fig. 1(d) of the main text, showing spectral broadening caused by lifetime reduction of the optical transition. Emitter B transition is broader due to the stronger Purcell enhancement. . . . .	49
3.10	<b>Dipole induced transparency (DIT) in SiC.</b> (a) A wide laser scan across the cavity resonance, showing the transmission spectrum through the device (black). The $V_{Si}$ phonon sideband emission is simultaneously detected (green, multiplied by 50x). Excitation of the resonator mode is performed through a scattering imperfection on the disk edge and transmission through the waveguide is detected. (b) Close-up scan at the cavity center for different emitter detunings. Orange and green traces are offset by +0.1 and +0.2 MHz, respectively. . . . .	50
3.11	<b>Superradiant emission of two <math>V_{Si}</math> color centers.</b> (a) Second-order correlation of the photon emission along one waveguide direction displays bunching at zero time delay, a signature of superradiance. Inset: zoom-in of the superradiance feature. (b) The relative phase $\phi$ of the emitters impacts the cross-correlation photon statistics between the opposite waveguide directions and can produce anti-bunched emission. The solid line in a,b is the numerical fit based on a five-level model[101] of the $V_{Si}$ . (c) The level structure representing the pair of two-level-system emitters decaying into degenerate clockwise (red arrows) and counterclockwise (blue arrows) optical modes. The corresponding transition rates are indicated next to the arrows, where $\Gamma$ is the unmodified single-emitter decay rate into a propagating mode. (d) Theoretically-predicted phase-dependent cross-correlation between clockwise and counterclockwise modes for a pair of ideal two-level emitters. . . .	52

3.12	<b>Manipulating the single-photon emission of a pair of emitters. (a)</b>	Weakly exciting the emitters with a resonant pulse (grey) through the CW mode will prepare the system in the superposition $(e^{i\phi}  eg\rangle +  ge\rangle)/\sqrt{2}$ , which will result in asymmetric emission rates. <b>(b)</b> By independently controlling the excitation phase of the two emitters positioned such that $\phi = \pi/2$ , the microresonator incorporates the functionality of a single-photon router. The phase of the free-space excitation pulse is represented by the color, where green, grey, and orange correspond to $\pi/2$ , 0, and $-\pi/2$ , respectively. . . . .	54
3.13	<b>Chiral single-photon scattering from a pair of emitters in a WGM resonator (a)</b>	The emitter pair is excited through the CW mode. Photons scattered into the CW (red) and CCW (blue) mode are time-correlated to the excitation pulse, tracing out the temporal shape of the emitted single-photon wavepacket. The solid red and blue lines represent the simulated expectation values $\langle a_{CW}^\dagger a_{CW} \rangle$ and $\langle a_{CCW}^\dagger a_{CCW} \rangle$ , respectively. The asymmetric CW and CCW emission arises from non-trivial emitter phase difference, inferred to be $(0.34\pi \bmod \pi)$ . The simulated case where $\phi = 0$ is shown as a grey dotted curve, in which case the emission is symmetric. <b>(b)</b> The PLE spectrum of the two emitters shows frequency separation of 0.44 GHz, which is used as a fixed parameter in the simulation of the wavepacket in (a). <b>(c,d)</b> Same as panels (a,b) but for emitter frequency separation of 0.19 GHz, with inferred phase $\phi = (0.28\pi \bmod \pi)$ . . . . .	55

3.14 **Spin selective temporally-filtered resonance fluorescence.** (a) Diagram of the experimental configuration. Temporally-modulated laser sideband at 18 GHz is generated using a phase electro-optic modulator (EOM) driven by an arbitrary signal generator (AWG). The sideband is spectrally filtered and sent to the device. The detected photons arrival times are correlated with the excitation pulse (Swabian Time Tagger): The earlier photon arrivals corresponding to the excitation pulse are discarded. (b) Resonance fluorescence spectrum of a single  $V_{Si}$  (blue data points) taken with 1 ns FWHM excitation pulses. The shaded areas correspond to the excitation pulse transform limit (0.44 GHz FWHM). The green data points are the simultaneously-acquired phonon side-band emission. Due to the strong Purcell enhancement of the defect, the phonon side-band detection rate is significantly lower than that of the ZPL. . . . . 62

4.1 **Electrical experimental setup.** The output from an arbitrary waveform generator (Keysight) is amplified (Minicircuits) and delivered to the cryostat via SMA RF cables. The signal is sampled via a -10 dB directional coupler to verify the quality of the amplified signal. Coaxial feedthrough connections allow signal transfer to the inside of the Montana Instruments cryostat. Inside the cryostat, the signal is routed through a flexible coaxial cable to a microwave PCB with a 50 ohm transmission line that terminates open on the 4H-SiC substrate. Three attocube piezoelectric actuators allow for three-axis motion of the sample. . . . . 65

4.2	<b>Optical experimental setup.</b> For PLE measurements, a CW laser (M Squared Lasers) scanned around 861 nm or 916 nm is used to excite the color centers. APDs (Excelitas SPCM-AQRH-14) are used for single photon experiments as well as two-photon correlation (switching between two modes is done with a flip beamsplitter. A scanning confocal setup is used to spatially raster the excitation and detection spots across the sample surface to identify single emitters. For optical pulsed measurements, a picosecond pulsed laser with 80 MHz repetition rate (Spectra Physics, Tsunami) is used. For the Ramsey interference experiment, a combination of a retroreflector on a mechanical stage and a mirror mounted on a piezoelectric crystal produces a pair of pulses with precisely-controlled delay. For the Rabi oscillations experiment requiring only one pulse, one of the paths is blocked. A pair of EOMs (Conoptics, LTA Series EOM) is used for pulse-picking with a 60 dB extinction. Throughout all experiments, above resonant pulsed excitation is used to stabilize the charge of the emitter, produced using a CW laser (MBR) at 740 nm and an AOM. Abbreviations: EOM: electrooptic modulator. AOM: acoustooptic modulator. BS: beamsplitter. CW: continuous wave. APD: avalanche photodiode. . . . .	66
4.3	<b>DC Stark tuning characteristics of the <math>h</math>-<math>V_{Si}</math>.</b> <b>a</b> The $h$ - $V_{Si}$ level structure. <b>b</b> Continuous PLE measurement over the course of 5 hours. <b>c</b> The intensity of the transitions averaged over the 5-hour acquisition, revealing inhomogeneous linewidths of the $A_1$ and $A_2$ transitions to be 259 MHz and 273 MHz, respectively. <b>d.</b> The $V_{Si}$ frequency is Stark tuned by 200 GHz by applying electric field parallel to the defect's symmetry axis. The detuning is relative to 347.821 THz. Left inset: electrostatic simulation of the field produced by micro-fabricated electrodes. Right inset: the 'kink' observed near bias of 0 V, also seen in the $k$ - $V_{Si}$ . A closer investigation of this feature is shown in Fig. 4.5. . . . .	67

4.4	<b>DC Stark tuning characteristics of the <math>k</math>-<math>V_{S_i}</math></b> <b>a</b> The $k$ - $V_{S_i}$ level structure. <b>b</b> Continuous PLE measurement over the course of 5 hours. <b>c</b> The intensity of the transitions averaged over the 5-hour acquisition, revealing inhomogeneous linewidths of the $A_1$ and $A_2$ transitions to be 117 MHz and 100 MHz, respectively. <b>d</b> Tuning characteristics of $V_{S_i}$ for a range of $\pm 5$ V. The ‘kink’ is observed near 0 V as in the $h$ - $V_{S_i}$ . The range indicated by the dashed box is investigated in Fig. 4.5. The detuning is given relative to 326.908 THz. . . . .	68
4.5	<b>Confirming the non-hysteretic nature of the DC Stark shift near 0 V bias.</b> As the bias on the electrodes is swept linearly from 0.5 V to 1.25 V and back, it can be seen that the nonlinear behavior is present when scanning in both directions, and thus is not caused by hysteresis. The detuning is given relative to 326.905 THz. . . . .	69
4.6	<b>Floquet eigenstates of the <math>h</math>-<math>V_{S_i}</math> under sinusiodal drive.</b> Spectral signatures of Floquet states in the $k$ - $V_{S_i}$ for $\Delta(t) = A \sin(\Omega t)$ harmonic drive, for swept $\Omega$ under a fixed amplitude of $A = 3$ GHz (upper), and swept $A$ with fixed $\Omega/2\pi = 750$ MHz (lower). Color corresponds to the normalized photon counts emitted into the phonon sideband.Color corresponds to the normalized photon counts from the PLE. . . . .	70
4.7	<b>Floquet eigenstates of the <math>h</math>-<math>V_{S_i}</math> under sinusiodal drive.</b> <b>a</b> Spectral signatures of Floquet states in the $h$ - $V_{S_i}$ for $\Delta(t) = A \sin(\Omega t)$ harmonic drive, for swept $\Omega$ under a fixed amplitude of $A = 3$ GHz. <b>b</b> Spectral signatures of Floquet states with logarithmically swept microwave drive power with fixed $\Omega/2\pi = 1$ GHz. Color corresponds to the normalized photon counts from the PLE. . . . .	71
4.8	<b>Large amplitude drive of <math>k</math>-<math>V_{S_i}</math></b> <b>a</b> PLE spectra of a single $k$ - $V_{S_i}$ driven at a frequency of 10 GHz and amplitudes of 8 and 16 GHz. . . . .	71

4.9	<b>Spectral diffusion under fast modulation.</b> <b>a</b> Continuous PLE measurement over 5 hours of $h$ - $V_{Si}$ under microwave drive of frequency 1.5 GHz and power 10 dBm. <b>b</b> Time averaged spectrum. A minor deviation from the theoretical model is seen due to power broadening, present only for the stronger sidebands due to the comparatively stronger coupling to the laser field. <b>c</b> A close-up of panel (a) around the Floquet sideband for the A2 transition, identified with a red stripe in panel (b). <b>d</b> Lorentzian fit to the time-averaged spectrum of the transition reveals a linewidth of $105 \pm 0.8$ MHz. <b>e</b> Continuous PLE measurement over 5 hours of the A2 transition of the same emitter but without modulation. <b>f</b> Lorentzian fit to the time-averaged spectrum of the transition shows a similar inhomogenous linewidth of $102 \pm 0.3$ MHz. Frequency is given relative to 347.920 THz . . . . .	72
4.10	<b>Two-photon scattering off a single Stark-modulated <math>V_{Si}</math>.</b> Measurement of the second-order photon correlation — $g^{(2)}(\tau)$ — under weak coherent excitation in the slow (15 MHz), intermediate (150 MHz) and fast (1.5 GHz) modulation regimes. The modulation-independent oscillations at short time delays originate from the interference of the multiple states in the ground manifold, as discussed in the Supplementary Information. In the limit of long time delay, $g^{(2)}(\tau)$ of a modulated emitter becomes periodic. To resolve the fine oscillatory features, we average the $g^{(2)}(\tau)$ data over many microwave periods (up to $\tau = 200\mu s$ ), shown in the right panel. . . . .	73

4.11	<b>Radiative level structure of the <math>V_{Si}</math> in different magnetic field configurations.</b> <b>a</b> In a magnetic field aligned with the symmetry axis ( <i>i.e.</i> $B_x = 0$ ), the optical transitions are spin-conserving. When resonantly addressing the $\pm 3/2$ transitions, the $\pm 1/2$ transitions are far detuned and are not excited. <b>b</b> When a low off-axis magnetic field is applied, the ground state spins are hybridized. The excited $\pm 3/2$ states, however, remain unhybridized due to the much larger excited state ZFS. The non-uniform hybridization is indicated in purple for illustrative purposes. The resulting optical level structure comprises total of 8 optical transitions varying only slightly (order of 10 MHz) in frequency. Crucially, unlike in the axial field case shown in (a), ground states are interacting via spin-non-conserving optical transitions.	74
4.12	<b>Signatures of ground states interference in <math>g^{(2)}</math>.</b> Top dataset is used to extract the three unknown rates of the $V_{Si}$ described in the text. Then, a higher laser power is applied, and a fit to the model is obtained using the external parameters $B_z, B_x, \Omega$ , whose resulting values are shown in the second dataset. Then, with laser power held at the higher level, axial magnetic field was adjusted, and the measurement was repeated (bottom dataset) . . . . .	75
4.13	<b>Stark-modulated <math>V_{Si}</math> interacting with short optical pulses.</b> <b>a.</b> Optical Rabi oscillations of a single unmodulated $V_{Si}$ excited by a 3 ps laser pulse. <b>b.</b> To observe the effects of fast Stark modulation on the orbital state, we measure Ramsey interference by driving the $V_{Si}$ with two identical $\pi/2$ resonant pulses separated by a course delay of 200 ps. The Ramsey interference contrast will strongly depend on the modulation period relative to the interpulse delay. <b>c.</b> Observed Ramsey interference for various modulation frequencies, as well as for the unmodulated emitter. The data series are offset vertically for clarity. When the interpulse delay is an integer multiple of the modulation period, the observed interference is identical to that of the unmodulated $V_{Si}$ . <b>d.</b> Ramsey interference for modulation frequency swept from DC to 10 GHz. As predicted theoretically, full interference contrast is recovered at 5 and 10 GHz. . . . .	76

4.14	<b>Ramsey pulse sequence.</b> First, an above resonant pulse initializes the emitter into an equal mixture ground state. A pair of 3 ps pulses (x-axis not to scale) manipulate the emitter orbital state. The single photon detector is gated to only detect the transient signal from the $V_{Si}$ (optical lifetime 6 ns).	78
5.1	<b>Approaches to scaling-up spin-based quantum photonic technologies</b> (a) Diamond nanophotonic cavity with a single silicon vacancy defect and an adiabatically-coupled fiber interface. [137] (b) Free-space coupled Fabry-Pérot microcavity enhancing the emission of an NV center in diamond [152]. Inset: the concave mirror can also be fabricated directly on the tip of a fiber [78]. (c) Pick-and-place heterogeneous on-chip integration of diamond microchips containing silicon and germanium vacancy centers on top of aluminum nitride photonic waveguides [196] (image courtesy of Noel Wan). (d) A heterogeneous approach without pick-and-place can be realized by using a secondary layer of photonic interconnects to post-select working quantum nodes [110]. (e) A conceptual diagram demonstrating how the example photonic network shown in Fig. 1.2b could be realized in a fully monolithic platform. In order to account for non-unity fabrication yield, $N$ redundant nodes are fabricated in the place of one node, and a $N \times 1$ switch (composed of cascaded $2 \times 1$ switches) selects one working node. Reproduced from: (a) [137], (b) [152, 78] (d) [110].	85
5.2	<b>A conceptual diagram showing two applications that can be readily implemented with the 4H-SiCOI architecture.</b> <b>a</b> On the left, the realisation of spin-spin entanglement scheme between two emitter-cavity systems. On the right, emission from a single $V_{Si}$ is delivered to a high-Q triply-resonant ring resonator to achieve frequency conversion to the telecommunication frequencies. Although for maximum circuit efficiency it is best to forgo silicon nitride interconnects, this approach may enable short term multi-qubit integration until near-unity single-qubit yield is attained <b>b</b> Material stack illustration for the proposed platform.	88

5.3 **Modal phase-matching for difference-frequency generation.** *Left:*

For a waveguide height of 350 nm, sidewall angle of  $\theta = 7^\circ$ , and radius of 27.5  $\mu\text{m}$  with  $\text{SiO}_2$  cladding, the phase-matching condition  $(n_T\omega_T + n_p\omega_p - n_e\omega_e)/2\pi = 0$  THz is achieved for a waveguide width of 725 nm. *Right:* The

absolute value of the primary electric field component in the ring cross-section for each mode. The spatial overlap diagram features the real component of

$\sum_{ijk} \chi_{ijk}^{(2)} E_{1i}^* (E_{2j}^* E_{3k} + E_{2k}^* E_{3j})$  prior to integrating over the volume. . . . . 89

# Chapter 1

## Introduction

Quantum information processing (QIP) is among the most rapidly developing areas of science and technology. It is perhaps the final frontier in the quest to harness the fundamental properties of matter for computation, communication, data processing, and molecular simulation. Any physical system governed by the laws of quantum mechanics can in principle be a candidate for QIP; to date, however, the most advanced QIP demonstrations have been implemented via superconducting qubits [6], trapped ions and atoms [220, 16], and photons (via linear-optical quantum computing) [68]. Recently, optically-addressable crystal defects have emerged as a novel platform for QIP [8, 9, 199, 49], interfacing some of nature’s best quantum memories (a protected solid-state spin [225, 22, 125]) with a robust flying qubit (photon) that can transport the quantum information [73]. Notably, solid-state defects lend themselves to on-chip integration, promising future scalability. Optically-addressable spin defects are thus noteworthy candidates for several QIP proposals, including network-based quantum computing [135, 139, 138], cluster state generation [25, 160, 164] and quantum communications [130, 19], and, in light of recent demonstration of fault-tolerant operation of a color center spin register using the NV center[1], distributed quantum computation.

In recent years, the field of defect-based QIP has made extraordinary strides toward realizing such proposals. Breakthroughs include the demonstration of long-distance entanglement of solid state spins [73]; high fidelity single-shot readout ( $F > 0.9995$ ) of a color center spin state and memory-enhanced quantum communication [17]; nanophotonic

quantum memories based on rare-earth ensembles [226] ; entanglement distillation between distant electron-nuclear two-qubit nodes [81]; a 10-qubit quantum register based on nuclear spins coupled to a single color center, with single-qubit coherence exceeding one minute [22]; and fault-tolerant operation of a color center spin register [1]. Although scalability is cited as a strength of optically-addressable spin defects, the field has yet to demonstrate a breakthrough toward this end: So far, entanglement has been realized between at most three optically-connected color centers in fiber networks [145], and at most two optically connected color centers a chip [52, 97]. A central issue is the efficient interaction between defects and photons. The photon emission of a dipole source is difficult to direct into a single optical mode, a prerequisite for photon interference. The resulting low collection efficiencies translate into prohibitively low rates of higher-dimensional entanglement generation. However, by integrating a defect with a nanophotonic cavity, one can greatly enhance the photon emission rate into the cavity mode via the Purcell effect, thereby funneling the majority of emitted photonics into the desired optical channel. This powerful technique has, for instance, enabled single-shot readout of single rare-earth ions [84, 150], which are too dim outside of a cavity to even observe individually. Many of the aforementioned recent breakthroughs in defect-based QIP have been enabled by integration with nanophotonics [17, 226, 52, 97]. Notably, the aforementioned three-node network demonstration [145] has been performed without coupling to photonic resonators, which suggests an optimistic outlook for the future once each node takes advantage photonic integration.

Defect-based integrated quantum photonics [199, 49] is thus a recent and exciting union of two distinct and rapidly developing fields: the study of quantum spintronics [9, 8] and the development of classical integrated photonics [197, 72, 104, 102]. In the rest of this chapter, we motivate in more detail the integration optically-addressable spin defects with nanophotonics, and then provide a brief overview of the various color centers present in Silicon Carbide.

## 1.1 Color centers

Color centers — atomic point defects in crystals — have been studied for almost a century, but only recently were the particularly interesting color centers in Diamond and Silicon

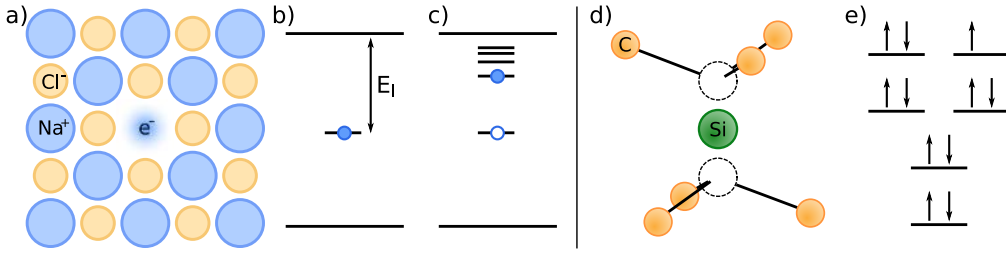


Figure 1.1: **Bound states in an atomic defect.** (a) Diagram of an F-center in NaCl. (b) The F-center ground state: A trapped electron. (c) The excited state: An electron-hole pair has eigenstates similar to that of a hydrogen atom with a modified effective mass and charge. (d) Diagram of a Silicon Vacancy ( $\text{SiV}^-$ ) in diamond. The 10 bound valence electrons contributed by the the carbon atoms and the silicon atom, as well as an additional electron acquired from the environment, form a 11-electron state, shown in (e). Figure reproduced from [188]

Carbide discovered and found to be promising for applications in single-photon sources and optically-addressable qubits. A color center resembles a single optically-addressable atom, well-isolated from the environment. The possibility of existence of bound states at a crystal lattice defect is made intuitive from the perspective of the Bloch theorem, which states that a periodic potential admits a continuum of propagating, non-scattering electronic states; when translational symmetry is broken, a bound state can form. However, in order for a defect to be a “color center”, it must admit at least two bound states that have an allowed optical transitions between them in the visible or IR frequency. This restricts suitable candidate materials to those with a large bandgap.

The first studied color centers are single-atom defects in an ionic crystal (referred to as F-centers, for German *fabre*); An example of an F-center is a missing Chlorine atom in a crystal of table salt, NaCl (Figure 1.1(a)–(c)). Upon removal of a sodium atom, the vacancy is filled with an electron from the environment, and the state has a binding energy of  $E_I$ . The set of bound states can be viewed as hydrogen-atom-like single electron states, where the electron is orbiting around a hole “nucleus”. [222]

In order to gain an understanding of the electronic structure of more complex color centers, such as the well-studied Silicon Vacancy center in diamond ( $\text{SiV}^-$ ) [74], one can use the linear combination of atomic orbitals (LCAO) method. Each of the six carbon atoms contributes one  $\text{sp}^3$ -hybridized orbital, and we assume that the interstitial Si modifies these

orbitals slightly and contributes its valence electrons to them. Thus, we have six orbitals and  $6 + 4 + 1$  electrons, from the C atoms, the Si atom, and the environment, respectively. This system can thus be equivalently modeled as a 1-hole system. Using group theoretical analysis [74] based on the crystal symmetry of the defect, one can understand the color center’s orbital degeneracy. In the case of the  $\text{SiV}^-$ , the group theory analysis arrives at two non-degenerate orbitals and two pairs of degenerate orbitals, as seen in Figure 1.3(e).

## 1.2 Motivation for combining spin defects with photonics

An optically-addressable defect, such as a color center, illustrated in Fig. 1.2a, features a ground state manifold with a long coherence time which can emit spin-entangled photons. This manifests as spin-dependent photon emission, where either the polarization or frequency of the photon encodes the electron spin state (alternatively, time-bin entanglement can be used [192]). The electronic spin can also be coupled to one or more nearby nuclear spins [9, 173, 22]. Thus the defect can serve as a multi-qubit register, for applications in error-corrected quantum computation (as part of a quantum photonic network, Fig. 1.2b) [138] or as a source of photonic cluster states [25, 160] for quantum communications and linear-optical quantum computing.

Spin-entangled optical photons are ideal carriers of quantum information for generating remote entanglement: Their high energy renders them insensitive to decoherence at room temperature (enabling routing of quantum information via the same commercial fibers that route classical data) and makes it possible to measure them with high quantum efficiency [51]. However, efficient manipulation and routing of optical photons is not a trivial problem. Distributed Bragg reflectors, such as photonic crystals, can be used to engineer a fully-reflecting boundary to confine and route light [121], but the high photon energy dictates the small feature size of these confining structures, requiring more sophisticated nanofabrication methods. Furthermore, since three-dimensional photonic crystals [121] (which create a complete  $4\pi$  steradian bandgap) are not yet practical, all means to confine light on a

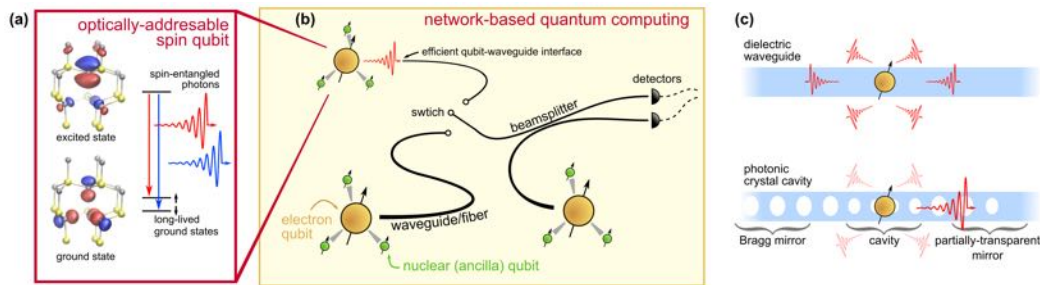


Figure 1.2: **Quantum photonics with optically-addressable spins.** (a) A suitable defect features a spin-selective optical transition, where a photon degree of freedom (i.e. polarization, frequency, or time-bin) is entangled with a ground-state spin featuring a long coherence time. The defect's optical lifetime is determined by the magnitude of its optical dipole moment, which in turn is dictated by the orbital structure of the excited and ground state. (b) A quantum photonic network consists of multi-qubit registers, each consisting of an optically-addressable electron spin strongly-coupled to nearby nuclear spins. The registers are integrated together in a network via an efficient waveguide or fiber interface. The network is equipped with beamsplitters and switches (which may be one and the same depending on the implementation) for long-distance entanglement and circuit reconfigurability. Low losses at all stages (including efficient photon collection from the defect, low-loss photon propagation in waveguide, and high detector efficiency) are essential for fault-tolerant computation, efficient quantum simulation, and long-distance quantum communications. (c) Due to the weak confinement of optical photons in dielectric structures, light from a quantum emitter does not couple efficiently to a simple dielectric waveguide. Instead, a nanophotonic cavity or a slow-light waveguide mode must be used to enhance the emission into the waveguide mode via the Purcell effect. Orbital graphic in (a) adapted from [131]

chip still rely on weak confinement via total internal reflection along at least one spatial dimension. Although a waveguide based on total internal reflection is a theoretically lossless and experimentally practical structure for routing photons on-chip, it is not straightforward to make a defect efficiently emit photons into the waveguide in the first place. This can be intuitively understood by decomposing the dipole radiation pattern in the plane-wave basis and noting that only a modest fraction of dipole emission goes into those plane wave modes which get totally internally reflected, while the rest are scattered into a free space continuum of modes. In order to increase the fraction of photons emitted into the desired mode (referred to as the  $\beta$  factor), one must rely on more advanced techniques, through careful control over the electromagnetic local density of states (LDOS). By embedding an emitter into a nanophotonic cavity that is coupled strongly to a waveguide, or by enhancing the LDOS in the waveguide itself [5], it is possible to enhance the defect’s single-mode emission while maximally suppressing all other scattering (Fig. 1.2c). Using this approach,  $\beta$  factors approaching unity (to the point where they are negligible compared to other losses) have been achieved [84, 17]. Since photon emission is reciprocal to photon absorption, a defect well-coupled to a waveguide (or cavity) is equivalently suitable for reflection-based spin-photon entanglement via dipole-induced transparency [195].

The control of LDOS of the quantum emitter not only minimizes the undesirable interactions with free-space modes, but also reduces the effects of other emitter nonidealities caused by its interaction with the solid-state environment. There are several mechanisms that degrade a defect’s performance as a spin-photon interface: First, environmental fluctuations induce decoherence of the emitted photons, manifesting as the broadening of optical linewidths beyond the Fourier-transform limit (thus reducing the emitted photon indistinguishability). Second, many emitters have non-radiative pathways, via for example phonon-assisted spin-mixing transitions [45]. As a result, most emitters have a non-unity *quantum efficiency*, meaning not every excitation yields a photon. Third, coupling of the optical transition to optical phonons creates an additional decay pathway, whereby a photon is emitted in combination with one or more phonons. This emission is broad in spectrum ( $> 0.1$  eV) and cannot be used for entanglement purposes. The fraction of “useful” — direct — emission into the zero-phonon line (ZPL) is referred to as the Debye-Waller Factor (DWF). The

DWF depends on the electronic orbital structure of the defect, and thus varies greatly for different defect types. Modification of the LDOS via, for example, integration of the defect into a cavity, enhances the emission rate into the ZPL via the Purcell effect, thus boosting the effective DWF and the quantum efficiency of the defect. Furthermore, since the emission enhancement is accompanied by lifetime reduction, the negative effect of spectral diffusion and homogeneous broadening on photon indistinguishability is also reduced.

Thus, the key purpose of combining a spin defect with photonic resonators is to increase its interaction with indistinguishable photons to enable efficient entanglement of remote defects. Here, “remote” signifies a distance greater than approximately 10 nm [136], beyond which direct dipole-dipole interaction between two defects is too weak.

### 1.3 Optically-addressable spins in Silicon Carbide

Silicon carbide, in its numerous polytypes, has proven to be a versatile host to optically-addressable, long-lived spin qubits [8, 9, 30]. Here, we briefly review the developments in spin-based quantum technologies in SiC. We focus on the two most well-studied color centers to-date, the silicon vacancy and the divacancy; we also highlight several emergent defects, such as the chromium ion, that may offer new functionalities. A summary of the properties of select defects in SiC is presented in Table 1.1. We note here that the more complex SiC polytypes like 4H and 6H have multiple inequivalent lattice sites within a crystal unit cell (illustrated in Fig. 1.3). Consequently, each defect in Table 1.1 is a family of several defect types with similar but not identical properties. In addition to inequivalent lattice sites, rotational symmetries of the crystal give rise to multiple orientations of the same defect, the properties of which are otherwise identical.

#### The Divacancy

The neutral divacancy is composed of adjacent silicon and carbon vacancies, denoted by  $V_{\text{Si}}V_{\text{C}}^0$ . The combination of  $C_{3v}$  symmetry, six active electrons, and spin-1 electronic structure render the optical and spin properties of the defect similar to the nitrogen vacancy (NV) center in diamond. However, the optical transitions are in the 1100 nm range, which is more favorable than the diamond NV center’s 637 nm emission for optical communications and

Table 1.1: **Optically-addressable spin defects in SiC**

Defect	ZPL (nm)	Polytype	Debye Waller Factor (DWF)	Inverse lifetime (MHz)	Measured linewidth (MHz)	Stark shift (GHz)	Spin $T_2$ (ms)	Refs.
$V_{Si}^-$	862-917	4H, 6H, 15R	0.06- 0.09	27	51	200	20	[177, 12, 172, 167, 131, 11, 40, 191, 165, 129, 159, 114]
$V_{Si}V_C^0$	1078- 1132	4H, 6H, 3C	0.07	11	20	850	$5 \cdot 10^3$	[89, 53, 35, 55, 87, 79, 36, 40, 126, 3, 125, 4]
$N_C V_{Si}^-$	1180- 1468	4H, 6H, 3C	-	75	-	-	0.001 ( $T_2^*$ )	[194, 219, 218, 39, 200]
$Cr^{4+}$	1042, 1070	4H	0.75	0.002	31	-	0.081	[90, 44]
$V^{4+}$	1278- 1388	4H, 6H	$< 0.50$	0.9-14	750	-	-	[180, 209]

for integration into nanophotonic structures; The DWF of 0.07 [36] is also an improvement over the NV center. Single divacancies with narrow optical linewidths and spin coherence up to 1 ms have been observed in SiC crystals without isotope purification [36]. Recently, the discovery of dressed clock transitions have enabled the demonstration of divacancy coherence of 64 ms in material with natural isotope content [125]. Divacancy ensembles have been used to achieve a high degree of polarization of the SiC nuclear spin bath [55, 79]. Ensemble entanglement with nuclear spins at ambient conditions has been shown [87], as well as the control of single divacancy-coupled nuclear spins [20]. Electrical and mechanical spin control of the divacancy have been demonstrated [88, 54, 205]. Recently, single-shot readout of the divacancy was demonstrated, enabling the observation of a five-second coherence time of the defect using dynamical decoupling [4]. In a major step toward wafer-scale optical and electrical integration of color centers, commercial *p-i-n* junction SiC devices have been engineered to host individually-addressable divacancies with nearly lifetime-limited optical transitions, millisecond spin-coherence times, as well as optical and electrical charge control[3]. Furthermore, these devices can produce a Stark shift as large as 850 GHz. This

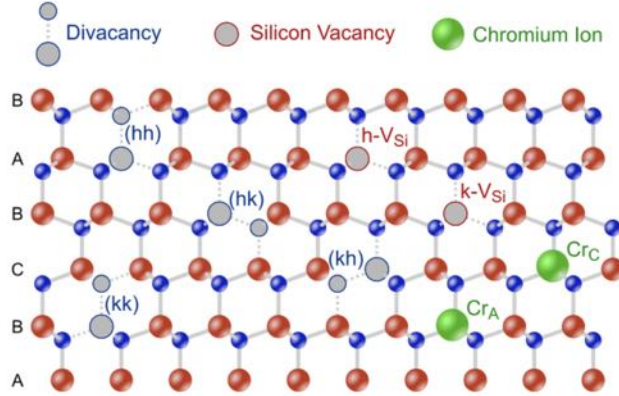


Figure 1.3: **Optically-active spins in SiC.** The 4H-SiC crystal lattice, showing the inequivalent configurations of the divacancy, silicon vacancy ( $V_{\text{Si}}$ ), and chromium ion.

is the first demonstration of such a combination of state-of-the-art optically-addressable spin-qubit properties in a single scalable semiconductor platform, opening opportunities for multi-qubit integration once combined with LDOS-enhancing photonic structures.

### Emerging defects

Numerous other defects in SiC are currently under investigation for applications in quantum photonics. The nitrogen-vacancy center ( $N_{\text{C}}V_{\text{Si}}^-$ ) in SiC has been identified as a color center with a favorable emission frequency near the telecommunications S-band [194, 39, 218, 219]. Recently, coherent spin control has been observed in  $N_{\text{C}}V_{\text{Si}}^-$  ensembles [200]. Further studies are necessary to investigate the cause of the low brightness of the  $N_{\text{C}}V_{\text{Si}}^-$  as compared to its diamond counterpart; it may be due to a low quantum efficiency (i.e., a large percentage of the excited state decay is into the non-radiative intersystem crossing) or a long-lived metastable state. Another defect, the chromium ion ( $\text{Cr}^{4+}$ ), has been identified as a promising quantum memory.  $\text{Cr}^{4+}$  has an optical excited state lifetime of 155  $\mu\text{s}$ , and emits 75% of photons into the ZPL in the near-IR [90, 44]. This suggests that integration of the  $\text{Cr}^{4+}$  into nanophotonic structures may enable a large reduction of lifetime, which is essential for the efficient readout of single spins without a cycling transition [150]. However, the intrinsic optical and spin coherence of  $\text{Cr}^{4+}$  defects remains an outstanding question; So far, only high density  $\text{Cr}^{4+}$  ensembles have been studied, where the optical linewidths are  $10^4$  times

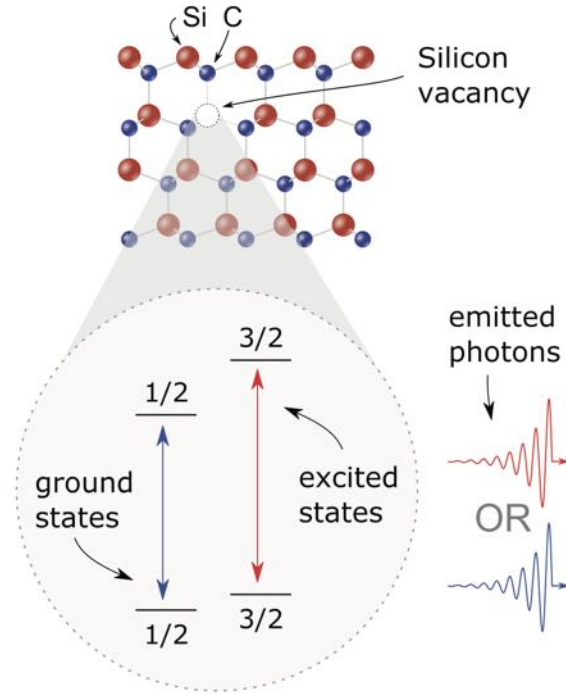


Figure 1.4: **The silicon vacancy ( $V_{\text{Si}}$ ) in SiC.** The spin-1/2 manifold and spin-3/2 manifold emit at different frequencies. In the diagram, the transition emission wavelength is represented by the color (red or blue), although the actual frequency difference of the optical transitions is very small (emission lines spectrally separated by just 1 GHz).

broader than lifetime-limited, and the measured spin-coherence time of 81  $\mu\text{s}$  is limited by spin-spin interactions in the ensemble [44]. Finally, we highlight the vanadium impurity in SiC,  $V^{4+}$ , which is notable for its emission in the O-band and unusual optical lifetime of 108 and 167 ns (for the brighter inequivalent lattice sites) [209]. Particularly interesting is the strong sensitivity of the  $V^{4+}$  optical transition to nearby nuclear spins, suggesting potential applications for optically-resolved nuclear spin registers [209].

### The Silicon Vacancy

The negatively-charged silicon vacancy ( $V_{\text{Si}}^-$ , written  $V_{\text{Si}}$  henceforth), a single missing silicon atom with an extra electron at the vacancy site, has been observed in the 4H, 6H, and 15R polytypes of SiC. Its electronic configuration is modeled by five active electrons (three holes) resulting in a unique spin-3/2 system [93], which has enabled novel sensing protocols

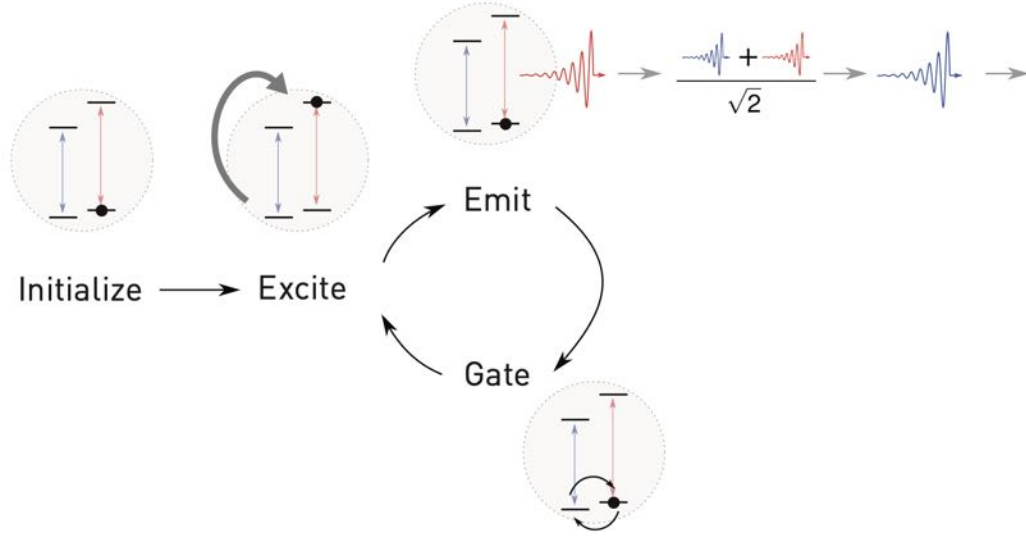


Figure 1.5: **The illustration of a cluster-state generation protocol.** If prepared in the  $1/2$  ( $3/2$ ) ground state, upon excitation with an above-resonant laser, the  $V_{Si}$  will emit a blue (red) photon. If the ground state is prepared in a spin-state superposition, the photon will be a superposition of red and blue. By repeatedly exciting the  $V_{Si}$  while applying a ground state gate after each emission, a variety of chains of entangled photons, such as the cluster state, can be generated [47]

[166, 168] and the realization of a spin qudit [171]. The spin-photon interface of the  $V_{Si}$  is illustrated in Fig. 1.4, and an illustration of how it be used for cluster state generation is shown in Fig. 1.5. In single isolated defects, a spin-coherence time of 1.4 ms has been measured at 10 K [10]. In  $V_{Si}$  ensembles, spin-coherence time as high as  $T_2 = 20$  ms has been observed using dynamic decoupling techniques [167]. Numerous approaches to generate  $V_{Si}$  have been studied, including irradiation using electrons [207, 35], neutrons [63], as well as ionized hydrogen [92] and helium[10]. In an effort to optimize  $V_{Si}$  generation, the impact of different irradiation approaches on spin coherence has been systematically investigated [82]. Direct laser writing [34], ion implantation [201, 10], and proton beam writing [92] have been investigated for deterministic defect placement. Recently, the theoretically predicted [178] excited state fine structure of the  $V_{Si}$  was experimentally confirmed in both inequivalent lattice sites in 4H-SiC [11, 131], enabling high-fidelity spin initialization [131] via the spin-selective intersystem crossing pathways [178, 45]. The observation of narrow optical

transitions [131, 11, 129], allowed for the demonstration of highly-indistinguishable photon emission with above-resonant driving [129], an important step toward implementing cluster-state generation proposals [47, 160]. The theoretically-predicted first-order DC Stark shift [190] has been observed in ensembles [159] (well as in single defects, with a tuning range of 200 GHz [114] is sufficient to overcome spectral inhomogeneity of defect ensembles [131] as will be described in Chapter 4 of this dissertation [114]). Integration into semiconductor devices such as the p-i-n junction has enabled electrical readout of the spin-state [140] and electrical control of the charge state [208] at room temperature.

### Theoretical model for the $h$ -V<sub>Si</sub> structure

The  $h$ -V<sub>Si</sub> Hamiltonian is given as  $H = H_{ZFS} + H_Z + H_d$  in terms of zero field splitting (ZFS)  $H_{ZFS} = \sum_{i=g,e} D_i(S_{i,z}^2 - 5/4)$  and Zeeman interaction  $H_z = \sum_{i=g,e} g\mu_B \vec{B} \cdot \vec{S}_i / \hbar$  spin Hamiltonians[179] in which  $\vec{S}_i$  are the well known spin-3/2 operators in each ground ( $g$ ) and excited ( $e$ ) state subspaces. The optical drive between the ground and the excited states is represented by  $H_d = \sum_i \omega (ae^{-i\omega_d t} |e_i\rangle \langle g_i| + \text{h.c.})$  for a laser of frequency  $\omega_d$  and amplitude  $\Omega$  (Rabi frequency). All radiative and nonradiative (intersystem crossing) decay processes of the V<sub>Si</sub> defect are represented by the Lindblad super-operators and shown in Fig. 1.6. The final Hamiltonian is constructed in the 12 Hilbert space spanned by four excited, four ground, and four metastable states shown in Fig. 1.6 that are previously determined by the electronic structure calculations and group theoretical analysis[178].

All four ( $d_1 - d_4$ ) metastable states with  $ve^2$  ( $A_1$ ),  $v^2e$  ( $E$ ),  $ue^2$  ( $A_1$ ), and  $uve$  ( $E$ ) orbital configurations (symmetry), shown in Fig. 1.6, form the intersystem crossing mechanism of this defect and responsible for the spin polarization. Due to their equal transition moments, both spin  $m_s = \pm 3/2$  ( $|e_2\rangle \rightarrow |g_2\rangle$ ) and  $m_s = \pm 1/2$  ( $|e_1\rangle \rightarrow |g_1\rangle$ ) radiative decay channels have the same rate  $\gamma_r$ . The general relationship between each non-radiative decay channel, within the same doublet orbital manifold, can be obtained by the phonon assisted direct spin-orbit coupling matrix elements, in the form of  $\frac{2\pi}{\hbar} \left| \langle \psi_{g,e} | \sum_j \lambda_z l_j^z s_j^z + \lambda_T l_j^{x,y} s_j^{x,y} | \psi_{d_1-d_4} \rangle \right|^2$  in the symmetry adapted wave-function basis of the  $j = 5$  active electrons of this defect center[178]. Therefore, the symmetry allowed nonradiative decay channels into and out of all the metastable states are identified by their corresponding spin orbit coupling coefficients

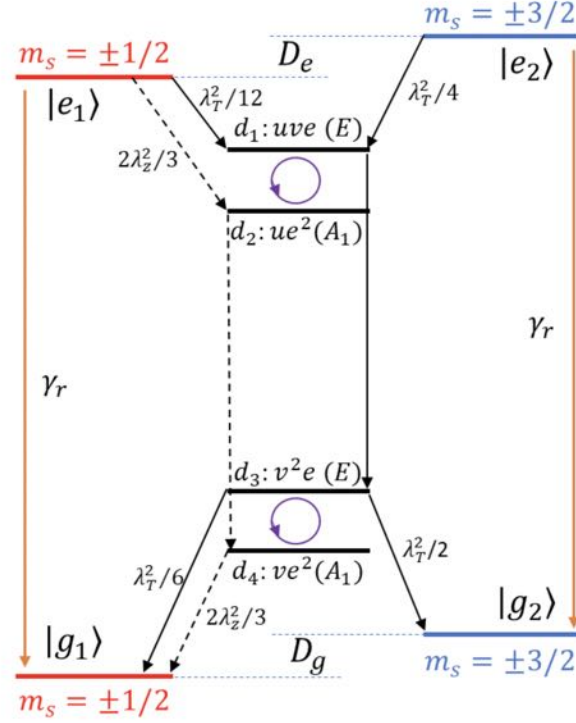


Figure 1.6: **Electronic fine structure model and intersystem crossing mechanism of the  $V_{Si}$ .** The radiative decay rates for both spin-3/2 and -1/2 channels are labeled as  $\gamma_r$ . The ground and excited state ZFS are given by  $D_g$  and  $D_e$ , respectively. Additional potential spin relaxation processes between allowed doublets (via spin-orbit coupling) are shown by circular arrows. Dashed and solid black arrows correspond to ISC channels assisted by the longitudinal and orthogonal components (with respect to the  $c$ -axis) of the spin-orbit coupling and optical emission polarization.

$\lambda_z$  (parallel to the  $c$ -axis) and  $\lambda_T$  (perpendicular to the  $c$ -axis) in Fig. 1.6. We note that, even though we use our 12-dimensional extended Hamiltonian for  $g^{(2)}(\tau)$  calculations here, in the presence of fast spin relaxation among  $d_1 \leftrightarrow d_2$  and  $d_3 \leftrightarrow d_4$  doublet states, the electronic fine structure of the  $V_{Si}$  can be reduced to earlier simplified models [131, 11] that involves only two metastable doublets instead of the four used here. Furthermore, here we assume the decay from upper to lower doublet states is due to emission of photons. Although these transitions can also be assisted by generally slower phonon processes, this does not affect our results here as both possibilities are indirectly taken into account under the overall lifetime of the metastable doublet states found here. Further studies in the future resolving

the detailed breakdown of the metastable state lifetimes may allow for the identification of the underlying dominant decay process between the doublets.

### Comparison of $k$ - $V_{\text{Si}}$ and $h$ - $V_{\text{Si}}$

4H-SiC admits two inequivalent single-atom defects, and consequently the  $V_{\text{Si}}$  appears in two varieties, either on the hexagonal site ( $h$ - $V_{\text{Si}}$ ) or the cubic site  $k$ - $V_{\text{Si}}$ . The  $k$ - $V_{\text{Si}}$  differs from the  $h$ - $V_{\text{Si}}$  in its optical frequency (ZPL at 916 nm compared to 861 nm for  $h$ - $V_{\text{Si}}$ ) as well as the zero-field splitting[190]: Compared with the ground (excited) state splitting of  $h$ - $V_{\text{Si}}$  of 4.5 MHz (1 GHz), the ground (excited) state splitting in  $k$ - $V_{\text{Si}}$  is  $-70$  MHz ( $-1$  GHz)[131, 11]. The  $3/2$  and  $1/2$  optical transitions from the lower excited state manifold, are denoted A1 and A2 for  $k$ - $V_{\text{Si}}$  and A2 and A1 for  $h$ - $V_{\text{Si}}$ . In this dissertation, we focus on the A1 and A2 transitions for obtaining indistinguishable single photon emission from the  $V_{\text{Si}}$ . For these transitions, the Debye Waller Factor is similar for both defects, at 8-9% [165, 191]. The larger ground state splitting of the  $k$ - $V_{\text{Si}}$  is advantageous as it enables high-fidelity driving of spin transitions with shorter microwave pulses.

A key distinction between the  $k$ - and  $h$ -  $V_{\text{Si}}$ , as investigated experimentally and theoretically in Ref. [191], is the energy separation of the upper excited state manifold from the lower excited state manifold (the complete level diagram is illustrated in Ref. [47]): The temperature at which the A1 and A2 optical transitions begin to display reduced coherence is dictated by their energy separation from the upper excited state manifold. Since  $k$ - $V_{\text{Si}}$  has a much larger energy separation, it operates well at higher temperatures. Specifically, while the  $h$ - $V_{\text{Si}}$  begins to degrade at a temperature of around 5 K,  $k$ - $V_{\text{Si}}$  remains coherent up to 20 K, making it much more robust for integration into 4 K liquid helium cryogenic systems.

## Chapter 2

# Silicon Carbide on Insulator

A tried-and-true approach for the development of integrated photonic circuits is through the use of thin films. Silicon wafers were widely available already in the 1970's, but it was not until the commercialization of the single-crystal Silicon-on-Insulator (SOI) platform in the 2000's that integrated silicon photonics took off.[214] High quality crystalline SiC has been commercially available for decades as a result of investment by the semiconductor industry. However, there has not been a demonstration of thin films with the crystal integrity of sublimation- or homoepitaxially-grown bulk crystal. The lack of high quality Silicon Carbide on Insulator (SiCOI) material has been a roadblock for utilizing SiC both in classical photonics and for scalable quantum architectures. This chapter covers the development of high-quality SiCOI via grinding and polishing, and how it enables high-performance SiCOI classical photonics.

### 2.1 Previous approaches to SiC-on-Insulator

Wafer-scale growth and processing of 4H and 6H polytypes of SiC was developed in the 1990's for applications in high-power electronics. Soon after, 4H- and 6H-SiC-on-insulator (SiCOI) were demonstrated [43] using the same ion-implantation (Smart-Cut) method that is used to produce silicon-on-insulator (SOI) wafers. This technology enabled the first demonstration of photonic crystal cavities (PhCs) in SiC [176, 211]. As the development of photonics in

Smart-Cut 4H-SiC continued [28] and Smart-Cut SiCOI became optimized on a wafer-scale [215], the intrinsic optical absorption of the SiC thin films was identified as the limiting factor for high-Q SiC photonics, limiting waveguide losses to  $> 5$  dB/cm [224]. Although further optimization of the implantation conditions may remedy the low material quality [28], it is unclear whether the Smart-Cut method is suitable for producing films of SiC with the same nearly-pristine crystal quality as silicon-on-insulator. The difference between Smart-Cut SOI and SiCOI stems from the drastically different thermal properties of silicon and SiC: The lattice of silicon will soften and heal at the modest temperatures achievable in standard quartz furnaces. SiC, in turn, is one of the most refractory materials, subliming at 2700°C. Repairing the lattice in post-processing without destroying the substrate is thus likely impossible.

Another approach to SiC photonics takes advantage of the heteroepitaxial growth of 3C-SiC films on silicon. A variety of 3C-SiC-on-Si photonics devices have been demonstrated, including PhCs [29, 148] and whispering-gallery-mode resonators [107]. However, this approach also suffers from substantial intrinsic material absorption, due to the high density of crystal defects near the growth interface caused by the Si-SiC lattice mismatch. Recently, a technique based on film transfer and back-side polishing introduced the 3C-SiC-on-insulator platform and enabled waveguides with losses down to 1.5 dB/cm, still likely limited by material absorption [56, 57].

Thus, the approaches to the production of thin film SiCOI have been limited to absorption-induced waveguide losses  $> 1$  dB/cm, which precluded nonlinear optics demonstrations such as optical parametric oscillation and efficient second harmonic generation that constitute a right-of-passage rendering a material platform useful for a variety of applications in integrated photonics.

If crystal lattice imperfections make themselves evident through increased optical absorption in nanophotonics, it does not bode well for the optical coherence properties of color centers. The coherence properties of color centers are highly sensitive even to low densities of unwanted defects. Indeed, in the first demonstration of SiC color centers coupled to a nanophotonic resonator — using PhCs fabricated in 3C-SiC-on-Si — the color center optical coherence was shown to be severely degraded by the lattice mismatch between Si and SiC

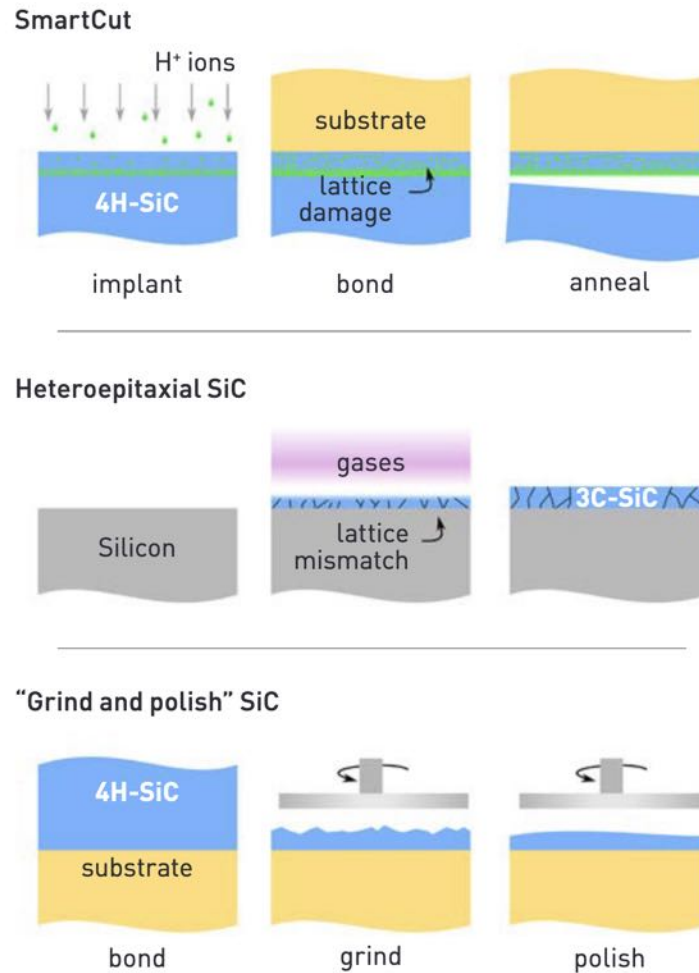


Figure 2.1: **Three approaches to preparing the SiCOI material platform.** (i) Ion slicing (known by its trademark name SmartCut) produces uniform thin films with thickness limited by the stopping range of hydrogen ions, as dictated by the ion energy. However, losses are significant due to the absorption from implantation-induced crystal defects. (ii) Direct growth of 3C-SiCOI via heteroepitaxy on silicon can produce arbitrary thickness uniform films, but lattice mismatch results in poly-crystalline films. (iii) The grind-and-polish method can be used to produce SiC with pristine crystal quality, but results in non-uniform thickness on the wafer scale. *Figure reproduced from [112].*

[27]. Similarly, color centers with good optical coherence have not been observed in Smart-Cut SiCOI, a consequence of the lattice damage induced by Smart-Cut ion-implantation: The dose required in the Smart-Cut process ( $10^{16} - 10^{17}$  ions/cm<sup>2</sup>) exceeds the dose used to generate spatially-resolvable single defects by four orders of magnitude. As noted above, it is possible to reduce the crystal damage from ion implantation by performing implantation at elevated temperatures [29]. However, optical coherence properties of color centers in SiCOI films produced with heated implantation have not yet been investigated.

## 2.2 SiCOI via grinding and polishing

The process for fabrication of 4H-Silicon Carbide on Insulator begins with fusion bonding of bulk 4H-SiC to an oxidized Si handle wafer, followed by thinning and chemical-mechanical polishing. The resulting material stack is a layer of 4H-SiC on top of a buried silicon oxide (SiO<sub>2</sub>) layer on silicon. The dimensions of the device and the buried oxide layers may be varied arbitrarily, enabling a variety of photonic applications.

Initially, we performed the demonstration on a chip-scale, bonding SiC dies to a silicon substrate. The process proceeds as follows: We begin with a 4 inch wafer of on-axis, research-grade, high-purity-semi-insulating (HPSI) 4H-SiC from Cree, Inc., and dice it into 10 mm x 10 mm dies. Dies are thoroughly cleaned, and approximately 20 nm of thermal SiO<sub>2</sub> is grown. Separately, a SiO<sub>2</sub>-on-Si handle wafer is prepared by thermal oxidation. The dies are bonded to the handle wafer at room temperature with manual pressure. The bond is strengthened by annealing at 900 °C, which results in a robust SiO<sub>2</sub>-SiO<sub>2</sub> fusion bond. The wafer is then processed in a wafer grinder (DAG810 from Disco Corp.), to thin the SiC to a thickness of 15 μm. The wafer is then chemically-mechanically polished (POLI-400L from G&P Tech.). Finally, SiC film is further thinned down to the desired thickness via reactive ion etching in SF<sub>6</sub>/O<sub>2</sub> plasma (PlasmaTherm Versaline ICP). The images of the SiC wafer at different stages of processing is shown in Fig. 2.2. In an industrial setting, a final thickness variation of ~ 1 μm across a 100 mm wafer should be possible. The methodology has also been implemented on the wafer scale [174]. Recently, researchers have shown uniformity of several microns across the entire wafer [198].

After the preparation of thin films of 4H-SiC, we proceed to the fabrication of photonic

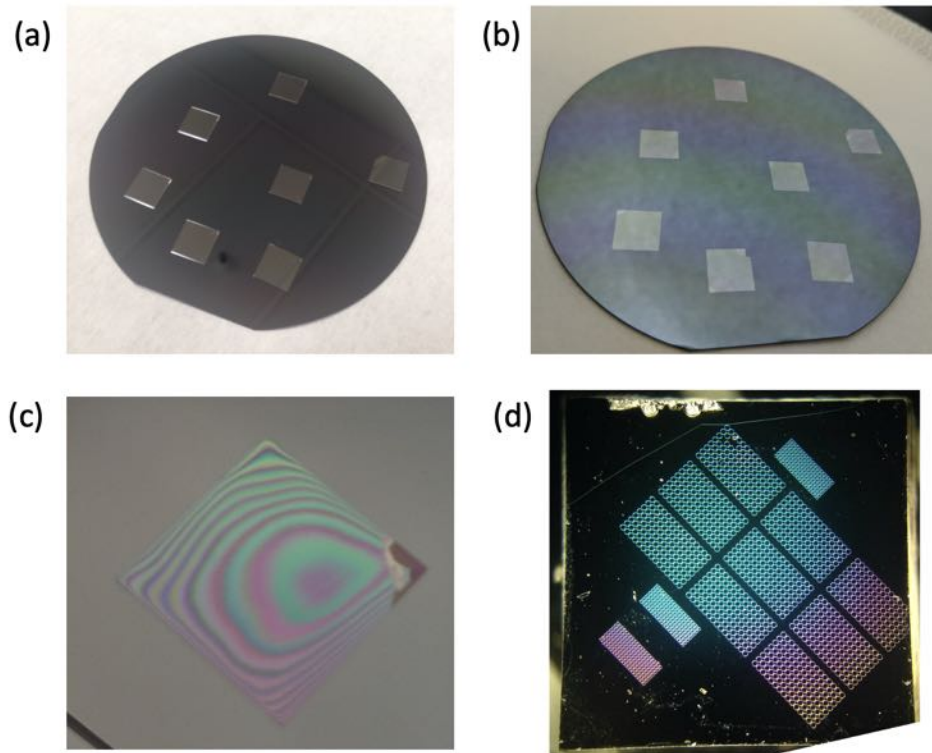


Figure 2.2: **Images of the thin films fabrication process on a die-scale.** (a)  $10 \times 10$  mm SiC dies bonded to the thermally-oxidized silicon wafer. (b) The wafer after thinning and polishing, with films approximately  $15 \mu\text{m}$  thick. (c) Close-up image of one die after reactive-ion etch thinning (thickness approximately  $1 \mu\text{m}$ ). The non-uniformity arising from edge effects is clearly visible. (d) A  $3 \times 3$  mm chip after device fabrication.

resonators to determine whether the improved material enables lower-loss photonics than previous approaches. Microring resonators are fabricated from 4H-SiCOI with a SiC thickness of 350 nm and a buried SiO<sub>2</sub> thickness of 3 μm. We define the pattern via electron beam lithography (JEOL 6300-FS) in HSQ resist (FOX-16, Dow Corning Corp.). Note that the only means of chemically removing the HSQ after the SiC etch is via HF, which would cause undesirable etching of the exposed buried oxide layer. To circumvent this issue, we spin a 30 nm layer of PMMA resist prior to spinning HSQ resist. The HSQ pattern is transferred into SiC via SF<sub>6</sub>/O<sub>2</sub> plasma. Then, the HSQ is lifted off by dissolving the PMMA layer in solvent. As a final step, we deposit 3 μm of SiO<sub>2</sub> cladding. Coupling to the ring resonators was performed via two point-coupled waveguides (below critical coupling), terminated with inverse-designed grating couplers. The Mach Zehnder interferometer used for spectral calibration of ring resonator measurements produces sinusoidal fringes with free-spectral-range of 194.1 MHz, and the free-spectral-range was calibrated using an adaption of the radio-frequency spectroscopy method.[98] Three TE mode families are observed in rings with diameter 55 μm, width 2.5 μm, and height 350 nm. The maximum quality factor (Q factor) of  $7.8 \cdot 10^5$  is measured for the fundamental mode, corresponding to propagation loss of 0.5 dB/cm (calculated using the simulated effective refractive index of the mode) as follows:

$$\text{waveguide loss (dB/cm)} = 10 \cdot \log_{10}(\exp(-2\pi n_{\text{eff}}/(Q\lambda)) \cdot [1 \text{ cm}])$$

This is an order of magnitude improvement over the state of the art in 4H-SiC waveguides at the time, where material absorption is cited as the limiting factor. [28, 56] Thus, we conclude that the pristine, mono-crystalline thin film material indeed enables improved performance of photonic devices.

### 2.3 Measuring the absorption limit of bulk 4H-SiC

After demonstrating that low-loss photonics are possible in SiC via the presented thin-film fabrication approach that preserves the bulk-crystal material quality, the natural question that arises is: What is the material-absorption limit of bulk 4H-SiC? To answer this question, we perform high resolution characterization of the intrinsic absorption of SiC via

photothermal common-path interferometry (PCI), which has been used to detect absolute absorption down to 1 ppm/cm [120]. In PCI, a low-power probe beam is used to sense the heating effect from the absorption of a high-power pump beam, as shown in Fig. 2.3a. The pump beam, with comparatively smaller waist, is chopped, periodically modulating the heating effect, which induces self-interference of the probe beam via the photothermal effect. We perform absorption measurements on sublimation-grown HPSI 4H-SiC (Shanghai Famous Trade Co. LTD) with resistivity exceeding  $10^5 \Omega\cdot\text{m}$  (Fig. 2.3b). The measured absorption is shown in Table 2.1. We note that the absolute accuracy of PCI requires a low-transparency calibration sample or precise knowledge of material properties, including the refractive index, the thermo-optic coefficient, the coefficient of thermal expansion, and the thermal conductivity. Based on previously-reported values of these parameters for 4H-SiC [202, 204, 100, 203], we conservatively estimate the absolute accuracy of the reported values to be  $\pm 25\%$ . However, the relative precision is within 1%. This allows us to observe wavelength-dependent anisotropy in absorption (3.68 at 1550 nm and 2.02 at 1064 nm). Such strong wavelength-dependent anisotropy suggests that residual optically-active defects with polarization-dependent near-IR and telecom absorption [219, 89, 206], rather than the bulk SiC lattice, may be the dominant source of loss; however, further investigation is necessary. Our high-resolution absorption measurements indicate that Q-factors exceeding  $10^7$  are possible in SiC. Defect-free epitaxial SiC layers used in quantum technologies [206, 131, 3] may enable photonics with even higher Q factors.

Table 2.1: **Intrinsic optical loss of HPSI 4H-SiC**

Wavelength	Polarization	Absorption (dB/cm)
1064 nm	$\perp$ c-axis	0.063
	$\parallel$ c-axis	0.031
1550 nm	$\perp$ c-axis	0.074
	$\parallel$ c-axis	0.020

## 2.4 Mask optimization for high-performance photonics

After the first demonstration of high-Q photonics in SiC, we began to explore fabrication optimization methods to further improve the photonics performance. We altered the fabrication process as follows: Instead of using HSQ as the resist, we opted for Aluminum

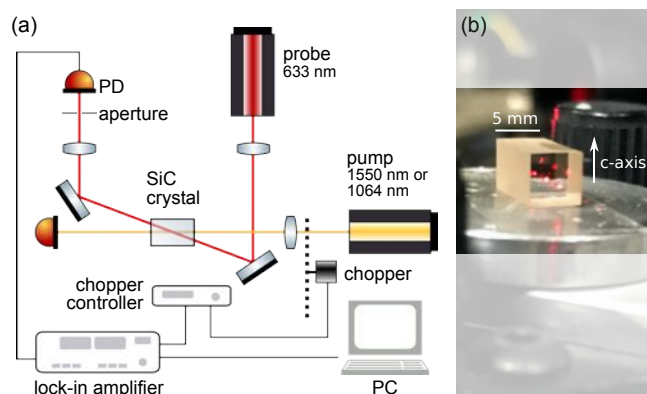


Figure 2.3: **Measurement of the intrinsic loss of 4H-SiC.** (a) Diagram of the PCI measurement setup, described in detail in Ref. [120]. (b) A crystal of 4H-SiC with dimensions of  $5 \times 5 \times 10$  mm undergoing the measurement. Multiple reflections of the red probe laser inside the crystal are visible.

hardmask with ZEP520 e-beam resist. The choice of ZEP was motivated by the reliability of its performance, especially important in the non-ideal conditions of a university cleanroom. The choice of Aluminum was motivated by its good resistance to  $\text{SF}_6$  plasma and the availability of a high-selectivity Aluminum plasma etch recipe provided for the Plasmatherm ICP-RIE etcher by the manufacturer. The switch to the Aluminum hardmask had further benefits: The Aluminum layer provides additional charge dissipation, and eliminates issues with adhesion and thermally-induced shrinking previously encountered with HSQ. One challenge we encountered is that the Aluminum would form bumps on the surface as a result of the post-spin bake of ZEP resist. We found that the deposition of a 5 nm layer of Titanium before and after the Aluminum deposition fully solved the problem. For the e-beam lithography, we switched to the Raith Voyager 50 keV instrument due to its spiral circle-writing capabilities. For the SiC etch, we reduce the etch power to target a slow etch at about 45 nm/minute etch, to decrease heating of the sample and to improve selectivity. We measured a hard-mask selectivity of 9 against SiC (compared to 2 for HSQ). Using this method, devices in SiC films as thick as 1.5  $\mu\text{m}$  can be fabricated. The modification of the lithography and etch process has enabled much higher reliability, better feature fidelity, and smoother sidewalls.

Figure 2.4a shows microring resonator devices before oxide encapsulation (cross-sectional diagram of the device shown in Fig. 2.4b). Q factors as high as  $1.1 \cdot 10^6$  are measured (Fig. 2.4c), which corresponds to waveguide loss of 0.38 dB/cm (in later experiments, we have observed Q-factors exceeding 5 million (Fig. 2.7)). Routing light to and from the chip is done via efficient and broadband inverse-designed vertical couplers [182, 46], designed for operation at normal incidence with a peak single-mode coupling efficiency of 31%, as illustrated in Fig. 2.4(d-f). Accurate pattern transfer and high aspect ratio nanostructures enabled by the new fabrication approach were essential for the demonstration of the close agreement between the simulated and measured efficiency at the target wavelength of 1550 nm.

## 2.5 Nonlinear photonics in SiC

SiC possesses a high second-order nonlinearity of 12 pm/V [162] as well as high linear and nonlinear refractive indices [67] ( $n = 2.6$  and  $n_2 = 6.9 \cdot 10^{-15}$  cm<sup>2</sup>/W at 1550 nm), which makes it suitable for highly efficient, compact second-order and third-order nonlinear photonic devices. In this section, we describe nonlinear photonic demonstrations that were enabled by the presented SiC-on-Insulator photonics platform.

### 2.5.1 Second harmonic generation

Here, we demonstrate efficient second-harmonic generation at sub-milliwatt powers using modal phase-matching in a high-Q microring resonator (Fig. 2.5a). Towards this end, we design the dimensions of the ring to induce geometric dispersion to balance the intrinsic material dispersion and allow for phase-matching across a wide frequency separation. To utilise the  $d_{31}$  nonlinear term in c-cut 4H-SiC, we design for phase-matching between the fundamental quasi-transverse-electric mode (TE<sub>00</sub>) at 1555 nm and a quasi-transverse-magnetic mode TM<sub>20</sub> at 777.5 nm. Finite-element method simulation using anisotropic Sellmeier equations[202] for air-clad 4H-SiC shows that effective refractive index matching is possible between these modes for a waveguide thickness of 350 nm, a waveguide width of 560 nm, and a microring radius of 27.5  $\mu$ m (see Fig. 2.5b). Two bus waveguides are designed to selectively

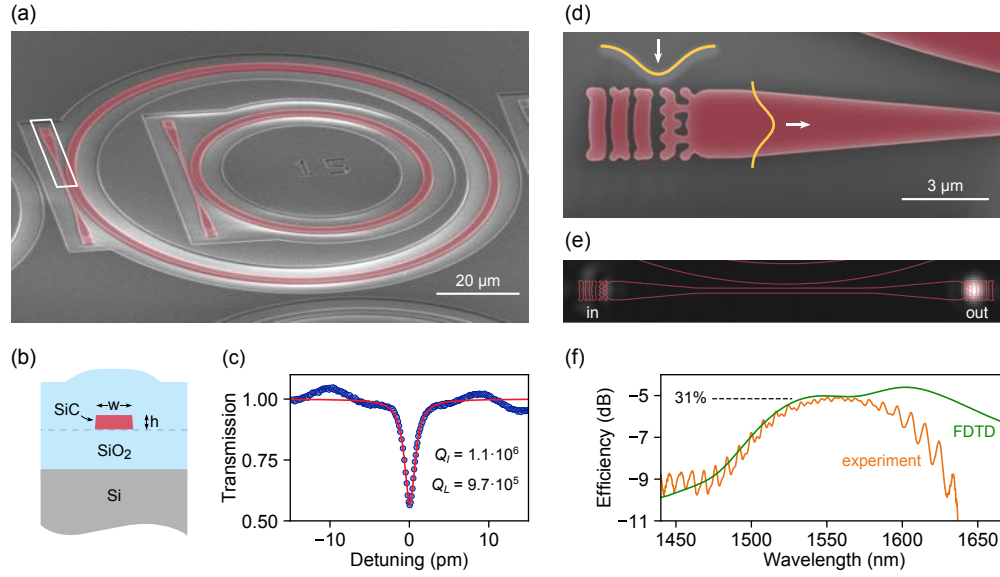


Figure 2.4: **Microring resonators and inverse-designed vertical couplers in 4H-SiC-on-insulator.** (a) A scanning electron micrograph (SEM) of two SiC microring resonators (false-colored) with diameters of 55  $\mu\text{m}$  and 100  $\mu\text{m}$  before SiO<sub>2</sub> encapsulation. (b) A schematic of the device cross-section after SiO<sub>2</sub> encapsulation. (c) Transmission spectrum of a ring with diameter 100  $\mu\text{m}$ , width 3.0  $\mu\text{m}$ , and height 530 nm, around a TE<sub>00</sub> resonance with an intrinsic Q of  $1.1 \cdot 10^6$  and loaded Q of  $9.7 \cdot 10^5$ . The wavelength is relative to 1532 nm. (d) A close-up SEM image of the inverse-designed vertical coupler, highlighted in (a). The coupler converts a near-diffraction-limited free-space Gaussian beam (focused via a 50x objective with NA=0.5) into the fundamental waveguide mode. (e) Camera image of the coupler operating at peak efficiency, showing little back-reflection from the input coupler, and a nearly-Gaussian beam at the output. (f) We measure the single-mode coupling efficiency to be 31% at the target wavelength of 1550 nm, in close agreement with finite-difference time domain (FDTD) simulation. The interference fringes observed in experiment are attributed to back-reflection in the couplers.

point couple either the pump or second harmonic, each equipped with inverse-designed grating couplers[46] optimised for the appropriate wavelength (see Fig. 2.5a). Via transmission measurements through each bus waveguide at the respective design wavelength, we measure loaded Q factors of  $8 \cdot 10^4$  for the pump at near-critical coupling and  $2 \cdot 10^4$  for the second harmonic, undercoupled with a transmission of  $T = 0.5$ . The devices were designed to be compatible with air-clad inverse-designed vertical couplers. By varying the pump power, we obtain a linear power dependence of the SHG with the square of the pump power, as expected in the undepleted pump limit (see Fig. 2.5c). The SHG efficiency is defined as the ratio between the generated second-harmonic power in the output waveguide versus the square of the pump power in the input waveguide; thus the efficiency of our SHG process is measured to be  $360\% \text{ W}^{-1}$ .

The efficiency of second harmonic generation in a doubly resonant cavity may be derived using temporal coupled mode theory[154]. At low input powers in the undepleted pump limit (marked by a quadratic dependence of output power  $P_2$  on input power  $P_1$ ), the second harmonic conversion efficiency is given by

$$\frac{P_2}{P_1^2} = 32 \frac{Q_1^4 Q_2^2}{Q_{1,c}^2 Q_{2,c}} \frac{|\beta|^2}{\omega_1}$$

where  $\omega_1$  is the frequency of the pump ( $\omega_2 = 2\omega_1$ ),  $\beta$  is the cavity mode coupling factor, and  $Q_k$  is the total Q of the  $k$ th cavity mode, described by  $\frac{1}{Q_k} = \frac{1}{Q_{k,c}} + \frac{1}{Q_{k,i}}$  where  $Q_{k,c}$  is proportional to the decay rate into the output waveguide and  $Q_{k,i}$  is proportional to the loss rate due to all other loss channels (including material absorption). Via transmission measurements through each bus waveguide at the respective designed wavelength (assuming that coupling into the non-designed bus waveguide for a given wavelength is negligible), we measure  $Q_1 = 8.5 \cdot 10^4$ ,  $Q_{1,c} = 1.3 \cdot 10^5$ ,  $Q_2 = 3.5 \cdot 10^4$ , and  $Q_{2,c} = 2.3 \cdot 10^5$ . The general representation of  $\beta$  for a three-wave mixing process is derived via perturbation theory to be

$$\beta = \frac{1}{4} \frac{\int d^3x \epsilon_0 \sum_{ijk} \chi_{ijk}^{(2)} E_{1i}^* (E_{2j}^* E_{3k} + E_{2k}^* E_{3j})}{\sqrt{\int d^3x \epsilon |E_1|^2} \sqrt{\int d^3x \epsilon |E_2|^2} \sqrt{\int d^3x \epsilon |E_3|^2}}$$

where  $i, j, k \in \{x, y, z\}$ ,  $\chi^{(2)}$  is the second-order nonlinearity of the material, and  $E_{lm}$  represents the electric field component polarized along  $m$  of the  $l$ th mode. In the SHG

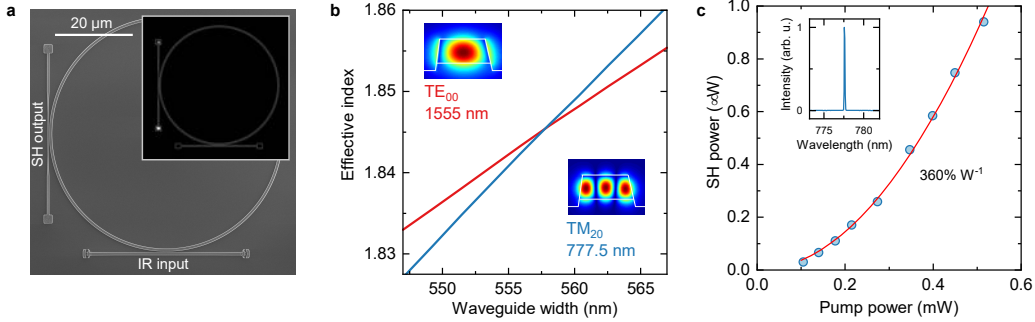


Figure 2.5: **Efficient second-order frequency conversion in microring resonators.** **a** SEM of a ring resonator designed for second-harmonic generation. The fundamental  $TE_{00}$  mode at 1555 nm is converted to a  $TM_{20}$  mode at 777.5 nm, and coupled out via a single-mode, effective index-matched waveguide. Inset: Optical image of the second-harmonic out-coupled via an inverse-designed vertical coupler (ring outline is overlaid for clarity). **b** Numerical simulation of the phase-matching condition for the 1555 nm  $TE_{00}$  and the 777.5 nm  $TM_{20}$  modes, demonstrating mode-matching for a waveguide width of 560 nm. Insets: Simulated mode profiles. **c** Dependence of second-harmonic power in the output waveguide on the pump power in the input waveguide. A quadratic fit reveals a conversion efficiency of  $360\% \text{ W}^{-1}$ . Inset: The second-harmonic signal imaged on a spectrometer.

process, this representation is simplified by setting  $E_1 = E_2$ . Using a finite-element method simulation, we solve for the mode profiles in a curved waveguide at the relevant wavelengths (see Fig. 5.3) and use them to calculate  $|\beta| = 4 \text{ J}^{-1/2}$ . Using the above model, the theoretical efficiency of our SHG process is approximately  $700\% \text{ W}^{-1}$ . This discrepancy is likely a result of nonuniformity in the microring waveguide dimensions at different azimuthal angles, which degrades overall phase-matching.[115] With improved Q-factors and optimized fabrication techniques, the conversion efficiency may be significantly improved.

### 2.5.2 Optical parametric oscillation in SiC

In order to generate degenerate four-wave mixing OPO, one must achieve frequency and phase matching between the pump, signal, and idler modes in the resonator. The frequency matching condition  $2\omega_p = \omega_s + \omega_i$  follows from conservation of energy. The phase matching condition ensures proper volumetric mode overlap and, for OPO within one mode family of a microring, reduces to the statement of conservation of angular momentum  $2\mu_p = \mu_s + \mu_i$ , where  $\mu$  is the azimuthal mode number [85]. The spectral characteristics of the OPO and

subsequent microcomb are determined by the dispersion relative to the pump mode ( $\mu_p = 0$ )

$$\omega(\mu) = \omega_0 + \sum_{k=1} \frac{D_k}{k!} \mu^k \quad (2.1)$$

where the  $k^{\text{th}}$ -order dispersion is  $D_k$ . Here,  $D_1$  is the free spectral range (FSR) of the resonator. When  $D_2$  dominates all higher-order terms and is positive (negative), the mode dispersion is said to be anomalous (normal).

We engineer microrings to possess anomalous dispersion in the  $\text{TE}_{10}$  mode across the telecommunications band for broadband microcomb generation [75]. The dispersion calculations include material anisotropy [202], and are performed in cylindrical coordinates to include the effect of the microring bending radius. For 100  $\mu\text{m}$  diameter microrings, target height of 530 nm and width of 1850 nm (with a sidewall angle of  $10^\circ$ ) are chosen. To predict the OPO behavior, we obtain a transmission spectrum across the full range of the tunable laser (1520-1570 nm), and extract the dispersion of the  $\text{TE}_{10}$  mode by measuring the frequencies of the resonances. To measure dispersion with high precision, we rely on a Mach Zehnder interferometer “ruler”, the free spectral range of which is measured using an adaption of the radio-frequency spectroscopy method [216]. Figure 2.6a shows the integrated dispersion  $D_{int} = \omega(\mu) - (\omega_0 + D_1\mu)$  with respect to mode number, to visualize all  $k \geq 2$  dispersion terms. Numerical simulation of the integrated dispersion for the target microring dimensions is plotted for comparison, showing agreement.

The intrinsic (loaded) Q factor of the  $\text{TE}_{10}$  mode is measured to be  $2.7 \cdot 10^5$  ( $1.8 \cdot 10^5$ ). At the OPO threshold power, primary sidebands emerge at  $\mu = \pm 12$ . As more power is injected into the microring, a primary comb at the multi-FSR sideband spacing emerges (Fig. 2.6b). At 75 mW, spectrally-separated sub-combs are formed around the primary lines. At the maximum injected power, the sub-combs fill out and interfere around the pump, which is evidence of chaotic comb generation [75]. The thermo-optic effect we observe in our devices may require the use of active capture techniques [217] for soliton formation, and lithographic control of device structure can eliminate avoided mode crossings, which may otherwise impede soliton capture. Using the experimental parameters of our device, we simulate the soliton frequency comb using the Lugiato-Lefever equation [32], neglecting Raman and  $\chi^{(2)}$  effects. The simulated soliton is shown in the last plot in Fig. 2.6b.

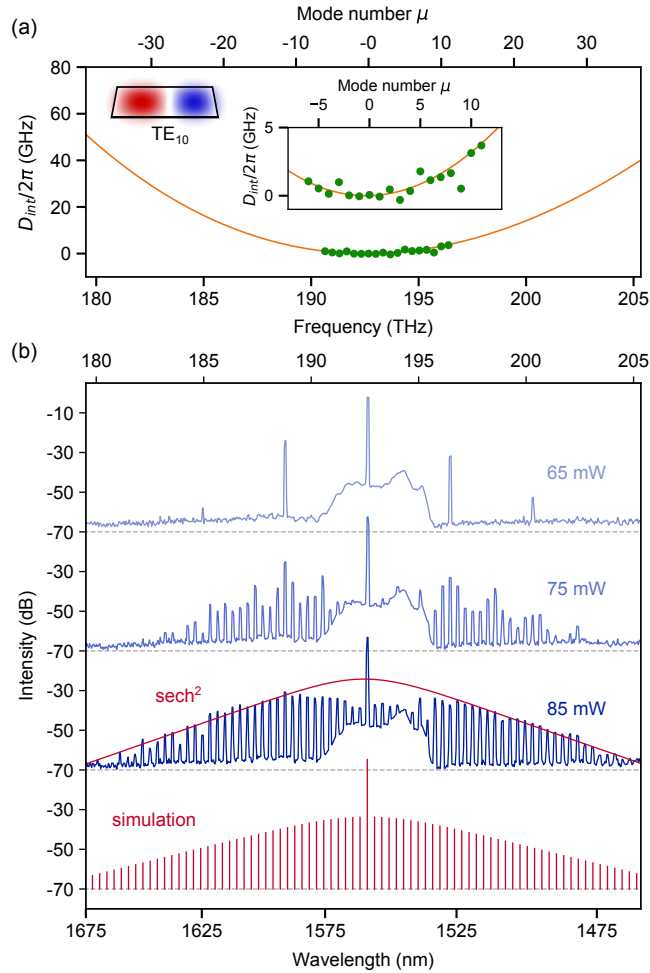


Figure 2.6: Microcomb formation in a 4H-SiC microring. (a) Measured integrated dispersion (green points) of the  $TE_{10}$  mode versus the relative mode number  $\mu$ , where  $\mu = 0$  corresponds to the pump mode. The orange curve is a numerical simulation, from which we extract  $D_2/2\pi = 61$  MHz and  $D_3/2\pi = -0.01$  MHz. Center inset: Close-up of the measured dispersion datapoints. Left inset: Numerical simulation of the  $TE_{10}$  mode cross-section. (b) Measured OPO spectra (blue) at different injected powers, featuring three distinct stages in the microcomb formation. A  $\text{sech}^2$  fit (red envelope) is overlaid onto the chaotic frequency comb for comparison to the characteristic soliton spectral shape. Simulation (red) of the soliton.

Finally, we measure the OPO power threshold in our devices and use it to determine the nonlinear refractive index ( $n_2$ ) of 4H-SiC. The power threshold of the OPO is defined as the input power in the waveguide at which the primary sideband emerges. This threshold is determined by the loss (described by the loaded quality factors  $Q_{L,s}$ ,  $Q_{L,i}$ , and  $Q_{L,p}$  of

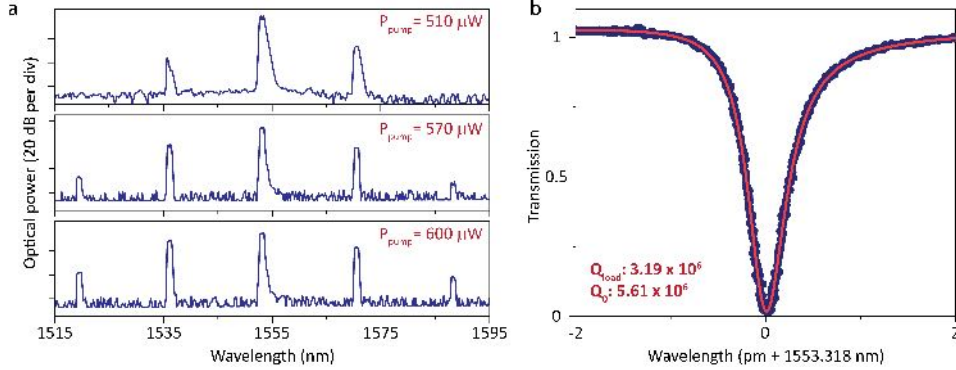


Figure 2.7: **Sub-mW parametric oscillation threshold power** (a) SiC parametric oscillation induced by pumping at the wavelength of 1553.3 nm. Top panel shows OPO just above the threshold power (510  $\mu\text{W}$  total power in the waveguide). Middle and lower panels show measured optical spectra with loaded pump power of approximately 570 and 600  $\mu\text{W}$ , respectively. (b) High-resolution scan of the fundamental TE mode with a loaded (intrinsic) quality factor of 3.19 (5.61) million. The mode is seen to be nearly critically-coupled to the waveguide. The scan laser wavelength is calibrated using a wavemeter, and the red curve is a fit to a Fano lineshape. The asymmetry of the resonance shape is attributed to interference with back-reflection of the vertical couplers.

the signal, idler, and pump modes, respectively) and the confinement

$$P_{th} = \frac{\omega_0 n^2}{8\eta m_2 c} \frac{V}{\sqrt{Q_{L,s} Q_{L,i} Q_{L,p}}} \quad (2.2)$$

where  $n$  is the modal refractive index,  $V$  is the mode volume, and  $\eta = Q_{L,p}/Q_{c,p}$  where  $Q_{c,p}$  accounts for coupling from the pump mode to the waveguide [109]. In this demonstration, we use the  $\text{TE}_{00}$  mode of a 55  $\mu\text{m}$  diameter ring resonator with the same cross-section as before. Although the dispersion is normal for the fundamental TE mode, pumping at an avoided mode crossing allows us to achieve frequency matching [210] and to generate OPO, while benefiting from the higher quality factors of the fundamental mode. By optimizing the pump power such that the OPO threshold is reached exactly on resonance, we measure a threshold of  $8.5 \pm 0.5$  mW. Using the simulated mode volume and measured quality factors, we extract a nonlinear refractive index for 4H-SiC of  $n_2 = 6.9 \pm 1.1 \times 10^{-15}$   $\text{cm}^2/\text{W}$  at 1550 nm, consistent with previous studies [223, 108].

### 2.5.3 Low-power OPO and soliton generation in SiC

Here, we describe the first demonstration of a soliton microcomb in a 4H-silicon carbide (SiC) microresonator.

The efficiency of the Kerr nonlinear interaction improves with higher quality factors of the optical resonator. For example, the threshold relation for optical parametric oscillation in a microresonator can be expressed in the following form:

$$P_{th} = \frac{\pi n \omega_0 A_{\text{eff}}}{4\eta n_2} \frac{1}{D_1 Q^2}$$

where  $Q$  denotes the total  $Q$  factor (intrinsic loss and loading included) with pump mode frequency  $\omega_0$ ,  $A_{\text{eff}}$  is the effective mode area,  $\eta$  is the cavity-waveguide coupling strength, and  $D_1$  is the free-spectral range (FSR) in units of rad/s. Zero detuning of the laser frequency with respect to the pump mode frequency is assumed. The parametric oscillation threshold is inversely proportional to the square of the  $Q$  factor. Fig. 2.7 shows a sub-milliwatt (approximately 510  $\mu\text{W}$ ) parametric oscillation threshold of a SiC optical resonator featuring an intrinsic  $Q$  factor of 5.6 million with a 350 GHz FSR.

Coherently pumped solitons in optical microresonators form as a result of the balance of the Kerr nonlinear shift and the cavity dispersion, as well as the parametric gain and the cavity loss. The soliton-forming mode family (in particular for bright solitons) in a microresonator must feature anomalous dispersion and minimal distortion of the dispersion (*e.g.*, minimal avoided-mode-crossings). The power requirement for soliton operation is inversely proportional to the total  $Q$  factor of the mode family[216].

Material	$Q_0$ (M)	FSR (GHz)	Soliton (OPO) Power (mW)	Ref
Si <sub>3</sub> N <sub>4</sub>	260	5	$\sim 20$	[80]
Si <sub>3</sub> N <sub>4</sub>	8	194	1.3 (1.1)	[181]
Si <sub>3</sub> N <sub>4</sub>	15	99	6.2 (1.7)	[103]
SiO <sub>2</sub> /Si <sub>3</sub> N <sub>4</sub>	120	15	28 (5)	[212]
LiNbO <sub>3</sub>	2.4	199.7	5.2	[71]
AlGaAs	1.5	450	1.77 (0.07)	[31]
SiC	5.6	350	2.3 (0.51)	This work

Table 2.2: Comparison of integrated soliton device performance

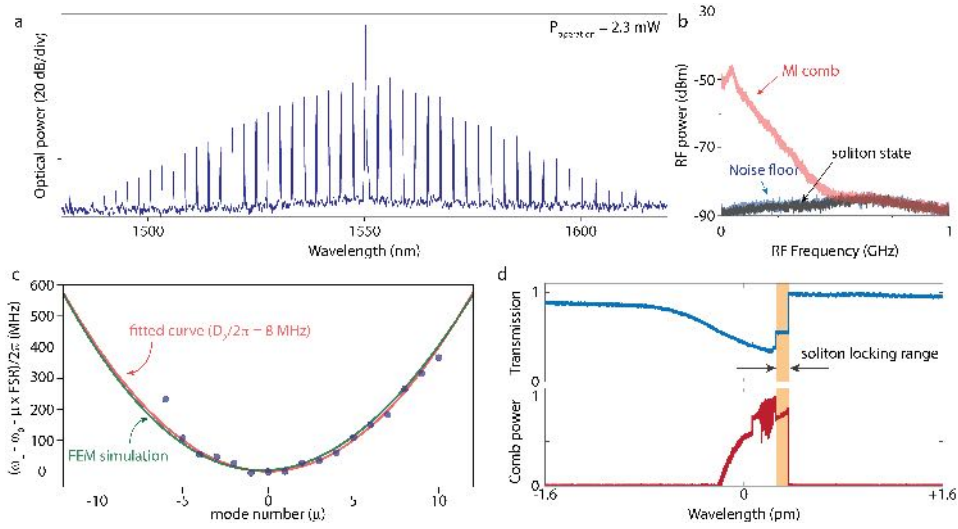


Figure 2.8: **SiC soliton microcomb** (a) The optical spectrum of a single soliton state with 2.3 milliwatts operation power. (b) RF spectrum (resolution bandwidth = 100 kHz) of the entire soliton comb confirms a low-noise state, compared to the non-locked modulation instability (MI) state. (c) Measured frequency dispersion belonging to the soliton forming mode family ( $TE_{00}$ ) is plotted versus the relative mode number. The red curve is a fit using  $D_1/2\pi = 358.663$  GHz and  $D_2/2\pi = 8$  MHz. Simulation of the soliton mode families is plotted (green curve), and the simulation fairly agrees with the measurement results. (d) Upper panel presents pump power transmission versus tuning across a resonance used for the soliton formation. Lower panel shows comb power trace in which the pump laser scans over the resonance from the short wavelength (blue detuned) to the long wavelength (red detuned). The shaded region (orange) depicts the spectral region where the single soliton exists.

We demonstrate the generation of a dissipative soliton microcomb in a SiC microresonator. The experiment is performed at cryogenic temperatures (5 K) in order to reduce the thermo-optic effects and to increase the stability of the system (high stability was needed to perform long-acquisition quantum correlations experiments with the soliton state [66]). Figure 2.8a shows the spectrum measured for a single-soliton state, and the soliton spectral shape follows the square of a hyperbolic secant function. Small spurs in the spectrum correlate with the avoided-mode-crossings in the mode dispersion spectrum (Fig. 2.8c), and the RF spectrum of the single-soliton state confirms that it is a low-noise state (Fig. 2.8b). While tuning the laser through the resonance mode, the pump power transmission as well as the comb power (Fig. 2.8d) show a step transition from modulation instability (MI) and a chaotic comb state to a stable soliton comb state. The high Q SiC resonator enables a low

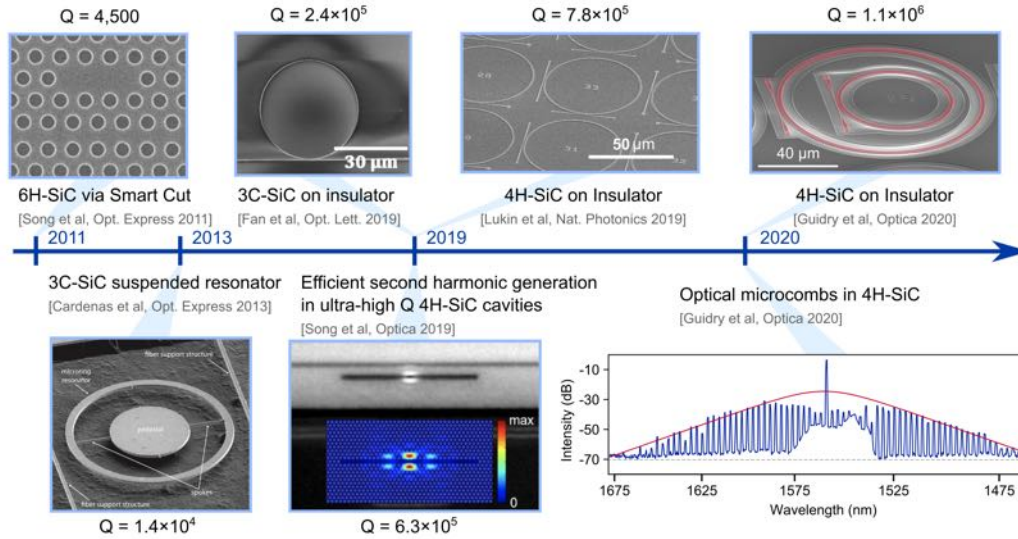


Figure 2.9: **Timeline of the first decade of SiC photonics.** The first demonstration of a SiC photonic device using the Smart Cut approach with 6H-SiC [176]. Soon after, suspended resonators in 3C-SiC-on-Si were demonstrated [29]. Strong intrinsic absorption of low quality Smart Cut and heteroepitaxial 3C films was hypothesized to limit the achievable Q-factors. Using thicker 3C-SiC epilayers or thinning down bulk-crystal 4H-SiC, enabled record Q factors in 3C-SiC [56, 57], ultra-high Q PhCs [174], and low-loss 4H-SiC-on-Insulator waveguides [110]. Devices with Q factors exceeding  $10^6$  were shown, enabling the demonstration of optical parametric oscillation and microcomb formation [67]. Reproduced from [176, 29, 57, 174, 110, 67]

operation power of the soliton microcomb of 2.3 mW: Table 2.2 compares operation powers of various chip-scale soliton devices.

## 2.6 Summary and outlook for SiC photonics

Since the first demonstration of a SiC photonics device by Song et al. over a decade ago [176], many approaches have been investigated in an effort to harness the potential of SiC as a high-performance photonics material. Figure 2.9 highlights the advances SiC photonics has seen in the first decade of its development. The Q-factor metric continues to be improved, with the recent demonstration of Q-factors exceeding 6 million [198]. Recent highlights in SiC photonics include octave-spanning microcombs [26], third- and fourth-harmonic generation in whispering-gallery resonators [198], and the demonstration of an electro-optic modulator [58, 147].

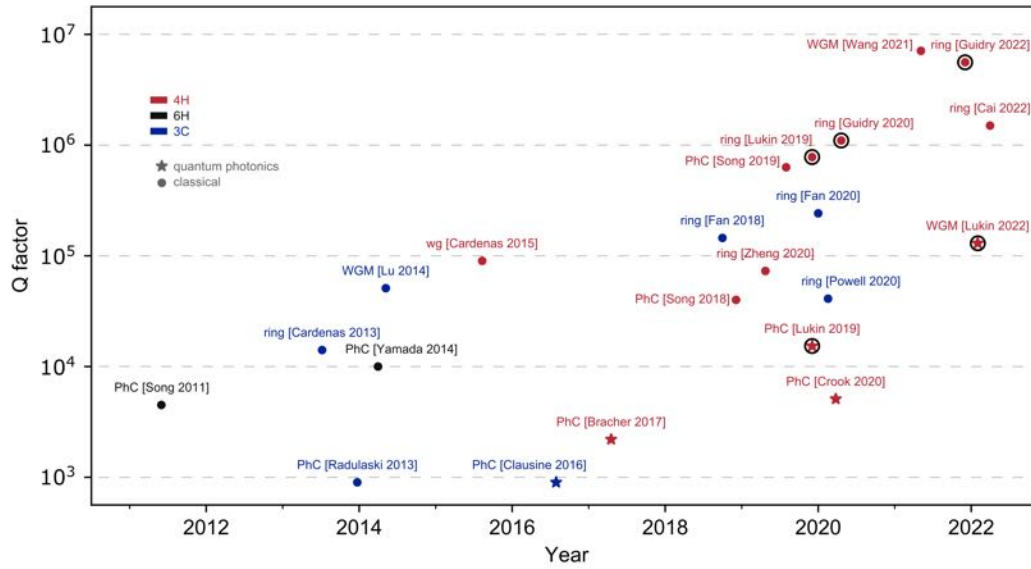


Figure 2.10: **SiC photonics demonstrations: Q-factor metric over the years.** Each reference is categorized by the SiC polytype (4H, 6H, or 3C); type of resonator (WGM - whispering gallery mode resonator, PhC - photonic crystal cavity, wg - waveguide, or ring resonator); and whether the resonator is coupled to color centers (quantum), or not (classical). Circled in black are the demonstrations presented in this dissertation. The following references are presented in the chart: Song 2011 [176]; Cardenas 2013 [29]; Radulaski 2013 [148]; Yamada 2014 [211]; Lu 2014 [107]; Cardenas 2015 [28]; Clausine 2016 [27]; Bracher 2017 [21]; Song 2018 [175]; Fan 2018 [56]; Zheng 2020 [223]; Song 2019 [174]; Lukin 2019 [110]; Crook 2020 [38]; Powell 2020 [147], Fan 2020 [57]; Guidry 2020 [67]; Wang 2021 [198]; Guidry 2022 [66]; Cai 2022 [26]; Lukin 2022 [113].

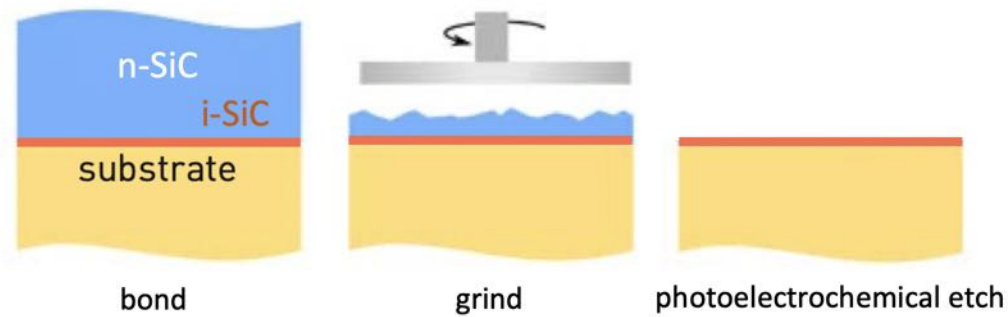


Figure 2.11: **Wafer-scale SiC-on-Insulator using photoelectrochemical etching.**

So far, only the 4H-SiC grinding and polishing method has attained low-loss photonics with Q-factors exceeding approx. 0.5 million, suggesting that pristine quality homoepitaxy may be necessary for attaining the highest performance photonics. This raises the question of the long-term scalability of this platform, since this approach cannot produce highly uniform SiC films for full wafer-scale processing (namely, where variation of less than a few percent across the whole wafer is desired).

Fortunately, a pathway to wafer-scale thin films of pristine SiC does exist. Specifically, we propose a modified grinding and polishing process that takes advantage of the photoelectrochemical etching technique developed for 4H-SiC [118]. The outline of this method is presented in Fig. 2.11. Instead of grinding and polishing an intrinsically-doped wafer to the target thickness, an n-doped wafer with i-SiC homoepitaxial layer is used as a starting point. At the grinding step, a few microns of the sacrificial n-SiC layer is kept, which is then selectively removed via photoelectrochemical etching, leaving the i-SiC-on-insulator layer. Polishing can then be performed to reduce the surface roughness intrinsic to the photoelectrochemical etching process. With this pathway to wafer-scalability, and considering the continued industrial investment into SiC growth and processing technology for electronics applications, it is conceivable that SiC-on-insulator photonics will, eventually, pass the stage of academic research and development and be deployed into CMOS photonics foundries.

## Chapter 3

# SiC quantum photonics

It is in the quantum context that the material quality of SiC thin films falls under the highest scrutiny: the coherence properties of color centers are highly sensitive even to low densities of unwanted defects. Indeed, in the first demonstration of SiC color centers coupled to a nanophotonic resonator — using PhCs fabricated in 3C-SiC-on-Si — the color center optical coherence was shown to be severely degraded by the crystal growth defects arising from the lattice mismatch between Si and SiC [27]. Similarly, color centers with good optical coherence have not been observed in Smart-Cut SiCOI, a consequence of the lattice damage induced by Smart-Cut ion-implantation: The dose required in the Smart-Cut process ( $10^{16}$ – $10^{17}$  ions/cm<sup>2</sup>) exceeds the dose used to generate spatially-resolvable single defects by four orders of magnitude.

This chapter describes the integration of optically-coherent color centers into SiC-on-Insulator photonics. First, single color centers are isolated in non-quantum-grade silicon carbide thin films, and Purcell enhancement of single emitters is demonstrated. Then, apply integrated photonics techniques to high quality homoepitaxially-grown SiC that has been shown to host optically-coherent  $V_{\text{Si}}$  color centers [11, 131]. We observe that the  $V_{\text{Si}}$  remain spectrally stable inside nanostructures, which enables us to show photon interference between two cavity-integrated emitters, constituting a key step towards SiC quantum networks based on remote color centers.

### 3.1 Isolated defects in SiC-on-Insulator

After the fabrication of SiC-on-Insulator from high-purity-semi-insulating (HPSI) SiC wafers (as illustrated earlier in Fig. 3.5), we investigate the properties of the intrinsic color centers in the material. First, we fabricate micropillars via reactive ion etching to improve the photon collection efficiency[149]. Using spatially-resolved photoluminescence spectroscopy we observe single color centers in 4H-SiCOI (Fig. 3.1a), which has not been possible before in thin-film SiC due to compromised crystal quality. The inset of Fig. 3.1a shows a scanning electron micrograph (SEM) of a micropillar, and a typical spectrum of single V1 ( $h$  lattice site) and V2 ( $k$  lattice site) silicon vacancies ( $V_{\text{Si}}$ )[131, 11, 47, 45]. The measurements are performed at a temperature of 5 K in a closed-cycle cryostat (Montana Instruments), with above-resonant excitation at 740 nm. The color center spectra show weak emission into the phonon sideband and minimal background noise, as reported in bulk 4H-SiC[131, 11]. By recording the fraction of micropillars that contain an emitter and estimating the micropillar volume, we arrive at an optically active defect density of  $0.1 V_{\text{Si}} \mu\text{m}^{-3}$ . In initial experiments we observed that 4H-SiC is susceptible to a strong background noise at the SiC-SiO<sub>2</sub> fusion bond, as well as at interfaces between SiC and the plasma-enhanced chemical vapour deposited (PECVD) oxide cladding layer. This noise overwhelmed the emission from color centers and would likely render the platform unusable for quantum applications. However, we found that a 20 nm thermal oxide layer grown on SiC (dry oxidation for 1 hour at 1000 deg C ) prior to bonding or PECVD deposition fully eliminates this undesirable PL, acting as a buffer against optically active formations at the SiC interface. We thus achieve the same low-background noise observed in high-purity homoepitaxial bulk crystal.[149]

### 3.2 Purcell enhancement of single color centers

As motivated in the Introduction, a critical requirement for multi-qubit spin-based optical quantum information processing is the ability to engineer high-fidelity interactions between a single quantum emitter and light. This can be achieved by placing a quantum emitter into a photonic resonator, thereby enhancing its interaction with light. The enhancement of the dipole-photon interaction in a resonator is quantified by the Purcell factor  $F$ :

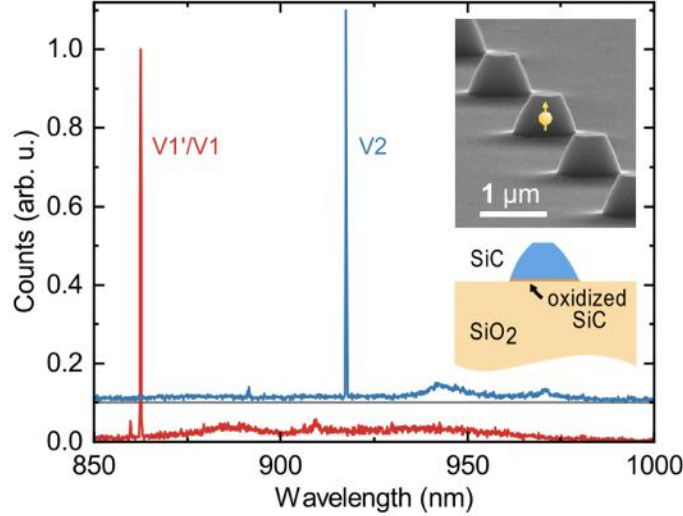


Figure 3.1: **Photoluminescence spectra of color centers in pillars fabricated in 4H-SiCOI**;  $h$ - $V_{\text{Si}}$  (V1'/V1) and  $k$ - $V_{\text{Si}}$  (V2) show narrow linewidths and low-intensity phonon sidebands. Insets: Scanning electron micrograph (SEM) of micropillars and corresponding material stack.

$$F = \frac{3}{4\pi^2} \left( \frac{\lambda}{n} \right)^3 \frac{Q}{V},$$

where  $\lambda$  is the emission wavelength,  $n$  is the refractive index, where  $Q$  is the quality factor and  $V$  is the cavity mode volume. Notably,  $F$  scales as  $Q/V$ . So, although whispering gallery mode resonators (such as microring resonators) typically have the highest  $Q$  among other nanophotonic devices, the microring  $V$  is also large ( $\sim 10^2 (\lambda/n)^3$ , where  $\lambda$  is the wavelength in vacuum and  $n$  is the refractive index of the material). Although coupling of 4H-SiC color center ensembles to nanophotonic resonators has been shown,[21] coupling of single color centers had not been demonstrated prior to our work. To maximize Purcell enhancement, we design photonic crystal (PhC) nanobeam cavities with a well-localised TE mode and simulated mode volume  $V = 0.46 (\lambda/n)^3$ . The fabrication of the cavities proceeds as follows: Starting with 4H-SiCOI where SiC thickness is 150 nm, and the buried SiO<sub>2</sub> thickness of 130 nm, we define the PhC nanobeam pattern via electron beam lithography (JEOL 6300-FS) in HSQ resist (FOX-16, Dow Corning Corp.). The pattern is transferred into SiC via SF<sub>6</sub>/O<sub>2</sub> plasma. Devices are suspended via a two-step undercut process: the

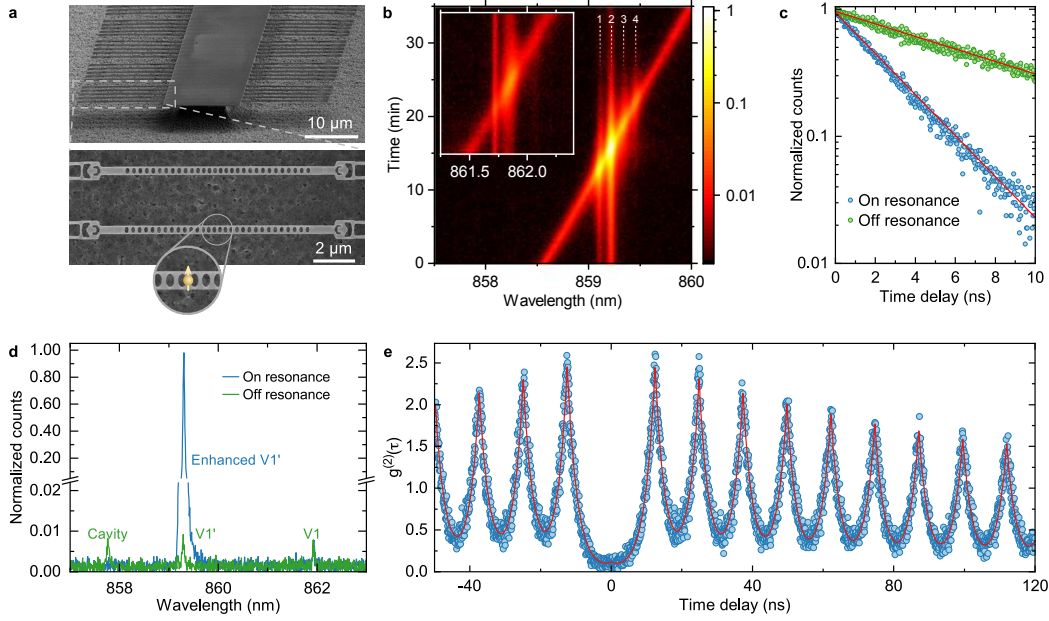


Figure 3.2: **Light-matter interaction of a single color center with a nanophotonic resonator.** **a** SEM of a suspended nanobeam array and close-up image of the devices from above. **b** Stacked spectra while tuning a nanobeam photonic crystal cavity resonance via gas condensation through the  $V1'$ . Individual color centers are indicated via 1-4. Inset: While tuning the cavity resonance through  $V1$ , we observe minimal enhancement of  $V1$ , which confirms that the dipole moment of the transition is orthogonal to the TE mode of the cavity. **c** Lifetime measurements with the cavity on- and off-resonance. Fitted lifetimes are  $\tau_{\text{off}} = 6.66$  ns and  $\tau_{\text{on}} = 2.45$  ns. **d** Spectra extracted from **b** with the cavity off- and on-resonance with  $V1'$ . **e** Second-order correlation measurement with the cavity on-resonance with the  $V1'$  transition of a single emitter, revealing  $g^{(2)}(0) = 0.08$ .

buried oxide layer and the resist are etched in a vapour HF etch, followed by a  $\text{XeF}_2$  gas etch that etches Si, suspending the photonic crystal cavity over  $5 \mu\text{m}$  above the substrate. In our experiments, we measure a maximum cavity Q factor of 19,300 corresponding to a  $Q/V$  ratio of over three times higher than for previous approaches in crystalline SiC [21, 175, 118, 106]. There remains room for further improvement in  $Q/V$  performance, such as via the use of heterostructure photonic crystal cavities demonstrated in SiC [174] that have a higher  $Q/V$  and feature a design that may offer advantages over nanobeam PhC for color center integration.

Since the residual density of  $V_{\text{Si}}$  in the nanobeam cavities is  $\ll 1$  per cavity volume, we

introduce them post-fabrication via flood implantation of  $H^+$  with energy of 10 keV (CuttingEdge Ions Inc.) to generate peak defect density at a depth of 75 nm, corresponding to the cavity mode maximum. The optimal fluence of  $2.3 \cdot 10^{10}/\text{cm}^2$  was estimated by assuming energy-independent ratio between simulated[227] and measured[91] conversion efficiency. No post-implantation annealing was done. Based on the reported polarisation of the optical transitions,[47, 11, 131] the primarily in-plane polarised resonator mode is predicted to couple maximally to the  $V1'$  transition and minimally to the  $V1$  and  $V2$  transitions. For our measurements, we select a PhC cavity with a Q factor of 14,900 that is blue-shifted from the  $V1'$  transition. Via Argon gas condensation, we tune the cavity resonance at a rate of 15 GHz/minute while continuously acquiring PL spectra, with excitation (740 nm wavelength) and detection aligned spatially to the center of the cavity. The zero-phonon lines (ZPLs) of individual  $V_{Si}$  become selectively Purcell-enhanced while on resonance with the cavity (individual emitters are labeled 1-4 in Fig. 3.2b). For further characterization of the coupled emitter-cavity system, we stabilized the cavity on resonance with emitter 2, which has the best spatial overlap with the cavity mode and thus the strongest cavity coupling. We excite the emitter with a 740 nm picosecond pulsed laser and observe that the 6.66 ns off-resonant optical lifetime is reduced to 2.45 ns when the cavity is on resonance (Fig. 3.2c). The luminescence intensity of the emitter, in turn, is enhanced by a factor of  $120 \pm 10$  (Fig. 3.2d) compared to off-resonant emission. The complex level structure of  $V1'$  and  $V1$ , with many unknown decay rates, does not allow the extraction of the Purcell factor ( $F$ ) from the lifetime reduction. A simulation of the cavity fields on- and off-resonance (as shown below) suggests that the intensity enhancement is not due to a change in cavity collection efficiency. Thus, although the lower bound on the Purcell factor from the known decay rates of  $V_{Si}$  is  $F_{\min} = 9$ , the actual Purcell enhancement is likely much higher. We verify that the cavity is indeed enhancing a single emitter by measuring the two-photon autocorrelation,  $g^{(2)}(\tau)$ , shown in Fig. 3.2e, and observing strong anti-bunching at zero time delay. A fit to the data using an effective three-level model (described below) reveals  $g^{(2)}(0) = 0.08$ , confirming single-emitter enhancement.

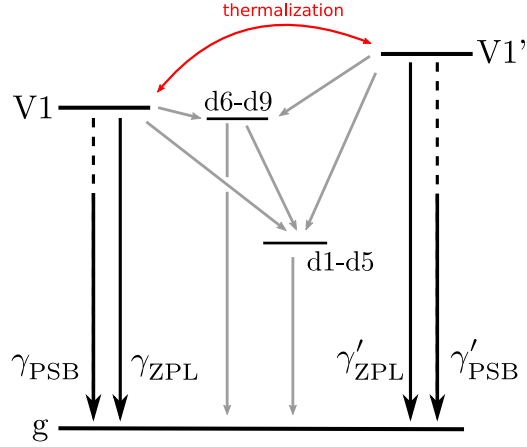


Figure 3.3: Level diagram of the  $V_{\text{Si}}$ , showing the decay channels of the  $V1$  and  $V2$  transitions. Detailed theoretical analysis of the levels is presented in [45]

### 3.2.1 $V_{\text{Si}}$ level structure and Purcell factor analysis

To measure the Purcell enhancement of  $V1'$ , we observe the reduction of the emitter lifetime while on resonance with the cavity. The resulting lifetime reduction (Fig. 3d in main text) is measured to be  $\tau_{\text{off}}/\tau_{\text{on}} = 2.7$ . The Purcell enhancement of the optical transition rate  $\gamma_{\text{ZPL}}$  is given by[59]

$$F = (\tau_{\text{off}}/\tau_{\text{on}} - 1)/\xi,$$

where  $\xi$  is the branching ratio in bulk crystal,

$$\xi = \gamma_{\text{ZPL}}/(\gamma_{\text{ZPL}} + \gamma_{\text{PSB}} + \gamma_{\text{therm}} + \gamma_{\text{ISC}}).$$

$\gamma_{\text{therm}}$  is the thermalization decay rate from  $V1'$  to  $V1$  at the low-temperature limit,  $\gamma_{\text{PSB}}$  is the decay rate into the phonon-sideband, and  $\gamma_{\text{ISC}}$  is the sum of the decay rates from  $V1'$  to the  $d1-d9$  manifolds (Fig. 3.3). The upper bound for the ratio  $\gamma_{\text{ZPL}}/(\gamma_{\text{ZPL}} + \gamma_{\text{PSB}}) < 0.19$  has been previously reported,[132] however, this value is difficult to estimate due to the thermalization of  $V1'$  transition into  $V1$ , and is possibly much lower. Disregarding  $\gamma_{\text{therm}}$  and  $\gamma_{\text{ISC}}$  would give an absolute lower bound on the Purcell factor of  $F > 9$ . Although the magnitudes of  $\gamma_{\text{therm}}$  and  $\gamma_{\text{ISC}}$  are not known, it was shown that  $\gamma_{\text{ZPL}} \ll \gamma_{\text{therm}}$ , [131] owing to the low visibility of the  $V1'$  transition at 4K, such that  $F \gg 9$ . Simulations

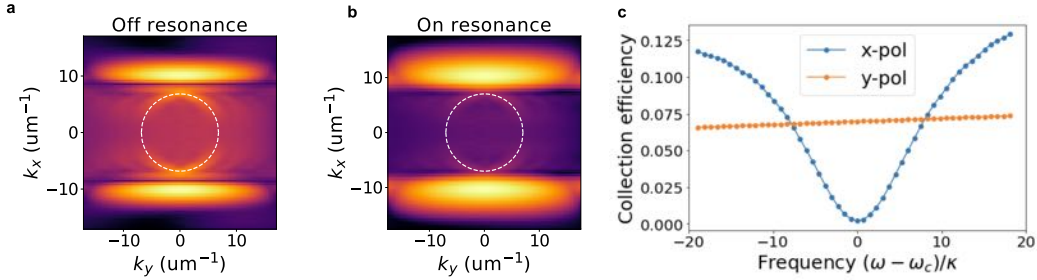


Figure 3.4: A plot of  $|E(k_x, k_y)|^2$  (Normalized such that  $\int |E(k_x, k_y)|^2 dx dy = 1$ ), where  $E(k_x, k_y)$  is the Fourier transform of the electric field just above the nanobeam cavity **a** off-resonance and **b** on-resonance. The light line ( $k_x^2 + k_y^2 = \omega^2/c^2$ ) is represented as a dashed line. These simulations indicate that while on-resonance, most of the field above the cavity lies outside of the light cone and thus does not contribute to the power collected by the objective. While off-resonance, the relative amount of power inside the light cone is higher, resulting in a larger collection efficiency. **c** The collection efficiency for a lens with an NA of 0.9 as a function of dipole-cavity detuning.

of cavity collection efficiency on- and off-resonance suggest that on-resonance collection is suppressed, as shown in Figure 3.4; However, since the theoretical Q factor greatly exceeds the experimental Q factor, losses are dominated by scattering and thus are not expected to result in significant modification of collection efficiency on resonance. This suggests that the intensity enhancement is primarily due to Purcell modification of the branching ratio. Additional experimental and theoretical studies of the transition rates of the  $V_{Si}$  would be needed to verify the Purcell enhancement value against lifetime reduction.

### 3.2.2 Numerical fit for $g^{(2)}(\tau)$

As described in detail elsewhere[45], the level structure of  $V_{Si}$  is complex, and most transition rates of the upper excited state manifold are not yet known. Thus, to perform the  $g^{(2)}(\tau)$  fit, we use a simplified three-level model,[63] which we expect to reproduce well the features of the two-photon correlation function, owing to the lifetime of the lower meta-stable manifold greatly exceeding all other lifetimes. Below, we derive the functional form of  $g^{(2)}(\tau)$  for a pulsed laser drive to perform a fit to our measurement.

The one-photon probability density is proportional to the population of the excited state,  $p_e(t)$ , and  $g^{(2)}(\tau)$  is proportional to the probability density of two emissions separated by

time  $\tau$ :

$$g^{(2)}(\tau) \propto \int_{-\infty}^{\infty} dt p_e(t)p_e(t + \tau).$$

In our limit of low photon detection rate, the probability of first emission at time  $t$  is obtained from the steady-state (unconditioned) excited state population (in the pulsed regime, by “steady state” we mean  $p_e$  is periodic with laser drive). The second emission is conditioned on the first; the population dynamics of  $p_e(t + \tau)$  are governed by the boundary condition,  $p_g(t) = 1$ , and the rate equations are:

$$\frac{d}{dt}p_e = -(\gamma_r + \gamma_{\text{ISC}})p_e + \sum_{n=-\infty}^{\infty} fp_g\delta(t - n\Delta t)$$

$$\frac{d}{dt}p_{\text{MS}} = \gamma_{\text{ISC}}p_e - \gamma_{\text{MS}}p_{\text{MS}},$$

where  $p_g$  ( $p_{\text{MS}}$ ) is the population of the ground (metastable) state;  $\gamma_r, \gamma_{\text{ISC}}, \gamma_{\text{MS}}$  are the decay rates  $e \rightarrow g$ ,  $e \rightarrow \text{MS}$ , and  $\text{MS} \rightarrow g$ , respectively; and  $f$  is the probability of excitation  $p_g \rightarrow p_e$  by a single pulse. Solving the piecewise continuous ODE system of equations yields an expression for  $g^{(2)}(\tau)$  which is then fit numerically to the data.

### 3.3 Optically-coherent color centers in thin-film photonics

The demonstration of Purcell enhancement described in the section above confirms that the SiC-on-Insulator material platform is of sufficient quality to host single emitters, but does not investigate the optical coherence of the color centers, whose spectral stability often degrades after processing or near surfaces [152, 155]. In this section, we demonstrate the integration of optically-coherent non-inversion-symmetric color centers into scalable thin-film SiC nanophotonics. We demonstrate cavity cooperativity of a single  $V_{\text{Si}}$  color center of up to 0.8, allowing for the observation of dipole-induced transparency[195] in SiC. We achieve a photon detection rate of up to 0.4 MHz from a single defect into the zero-phonon-line (ZPL), limited by the population shelving in the metastable state. We use this platform to

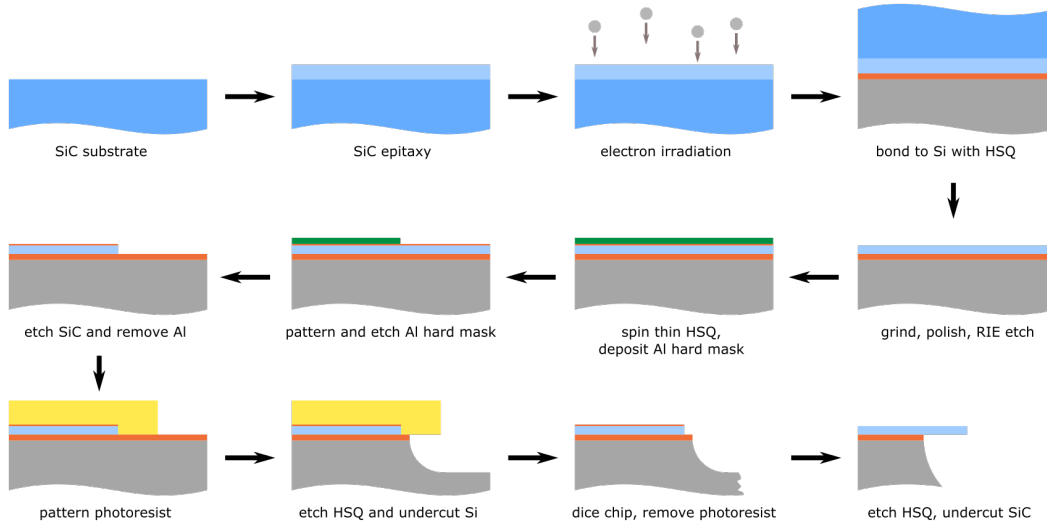


Figure 3.5: **Device fabrication process flow.** Colors correspond to materials as follows. Blue: SiC substrate. Light blue: SiC epitaxy. Grey: Si substrate. Orange: HSQ. Green: hardmask. Yellow: photoresist.

demonstrate superradiant emission of two SiC color centers, and highlight the unique applications of the two-emitter whispering-gallery-mode (WGM) resonator system for quantum information processing architectures. This challenges the notion that inversion symmetry is a prerequisite for nanophotonic integration of optically-coherent spin defects, and bridges the classical-quantum photonics gap by uniting color centers with CMOS compatible, wafer-scalable, state-of-the-art photonics[174, 67, 66].

### 3.3.1 Device fabrication

Due to the dipole orientation of the linearly-polarized transitions in  $V_{Si}$  along the c-axis of the crystal, corresponding to the out-of-plane direction, we use a whispering gallery mode resonator (hosting high Q TM modes) for coupling to the  $V_{Si}$ . The device fabrication process is summarized in Fig. 3.5, and proceeds similarly to the methodology described in Chapter 2, with the key difference being a higher quality of starting material. First, a 20  $\mu\text{m}$  n-doped (nitrogen concentration  $2 \cdot 10^{13} \text{ cm}^{-3}$ ) SiC epilayer is grown by chemical vapour deposition on a n-type (0001) 4H-SiC substrate. Then, the SiC is irradiated with 2 MeV electrons with a fluence of  $1 \cdot 10^{13} \text{ cm}^{-2}$  to generate  $V_{Si}$  defects. The SiC is bonded to a Si substrate via

an HSQ flowable oxide layer (FOX-16, Dow Corning) and annealed at 550 °C for 2 hours to strengthen the bond and activate  $V_{Si}$  defects. The SiC is then thinned via grinding, polishing, and reactive-ion etching (RIE) [110] to 450-620 nm. A 50 nm protective layer of HSQ is spun, followed by e-beam evaporation of the etch hard mask layer (5 nm Ti / 155 nm Al / 5 nm Ti). The device geometry is patterned via e-beam lithography (JEOL 6300-FS) in ZEP520A resist (Zeon Corp), and transferred into the Al hardmask layer via chlorine-based RIE. The SiC layer is etched using  $SF_6$  in a capacitively-coupled plasma etcher (Oxford Plasmalab 100) at an etch rate of 45 nm/min, with gas flow rate of 50 sccm, pressure of 7 mTorr, etch power of 100 W, and substrate temperature maintained at 20 °C. For best quality of the waveguide facet used for in- and out-coupling, it is defined as part of the lithography and RIE etching together with the rest of the geometry, to avoid rough facets that can result from dicing a waveguide. After the SiC etch, the Al hardmask is then removed via a wet etch in Aluminum Etchant Type A. The final steps of the fabrication achieve an undercut device diced in close proximity to the waveguide facet. This is done as follows: First, an approximately 50  $\mu\text{m}$  wide and 10  $\mu\text{m}$  deep Si trench is created 15  $\mu\text{m}$  from the waveguide ends using photoresist mask and  $XeF_2$  isotropic Si etch. Then, the chip is diced along the trench, while the photoresist provides protection to the device layer. Finally, the photoresist is removed, and the device layer is uniformly undercut via wet HF etch and  $XeF_2$  gas etch, to suspend the resonator and waveguide.

### 3.3.2 Experimental setup

The experimental setup is shown schematically in Fig. 3.6(a). The sample is mounted in a closed-cycle cryostat at 5 K with the cryo-optic module (Montana Instruments) where an objective with an NA of 0.9 is mounted inside the vacuum chamber. The sample is mounted on a three-axis piezo positioner stack (Attocube) so that the waveguide facets point up toward the objective (optical images shown in Fig. 3.6(b-d)). The optical paths coupling to the two waveguide ends are spatially separated into separate fiber couplers. We observe a total coupling efficiency from the waveguide to the single-mode fiber of up to 24%, which includes all setup losses. Dichroic mirrors allow for simultaneous collection of ZPL and PSB emission [15]. For continuous-wave above-resonant excitation (such as to measure

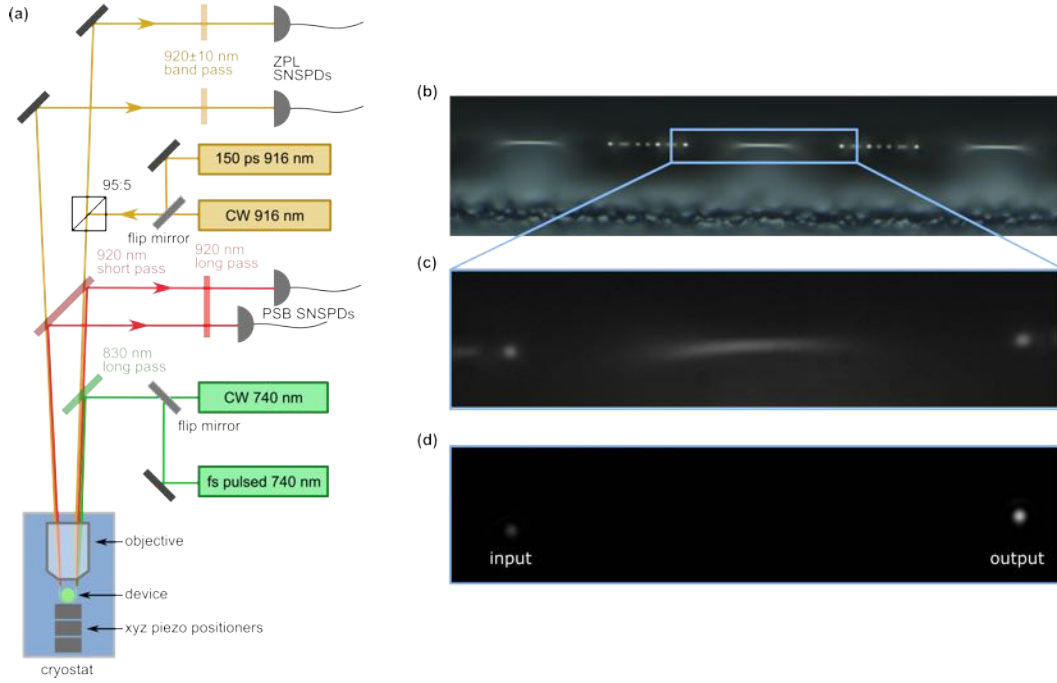


Figure 3.6: **Experimental setup.** (a) Diagram of optical paths, laser sources, and detectors. (b) Optical microscope image of a row of disk resonators (three resonators are visible), taken using a commercial optical microscope. (c) Optical image of a single device under illumination as seen through the cryostat objective. (d) Optical image of the device without illumination and laser light coupling into the left waveguide facet, passing through the waveguide and emitting from the right waveguide facet.

two-photon interference) and for  $V_{Si}$  charge control, a continuous-wave Ti:Sapphire laser is used, with wavelength tuned to couple to a resonator mode around 740 nm for uniform excitation of the resonator mode volume. During the gas-tuning phase, a femtosecond pulsed Ti:Sapphire laser is used to achieve multi-mode excitation of the microresonator that does not vary with resonance shifting due to gas deposition. For resonant excitation, a continuous-wave Ti:Sapphire laser is used for PLE and DIT measurements, whereas a picosecond pulsed Ti:Sapphire laser is used for on-resonance lifetime reduction and single-photon interference measurements. The picosecond laser outputs 5-15 ps FWHM pulses, which are sent to a pulse-shaper to produce 150 ps pulses that are bandwidth matched to the microresonator optical mode that the  $V_{Si}$  are coupled to. Photons are detected using superconducting nanowire single photon detectors (SNSPDs), produced by PhotonSpot Inc., and photon correlations are processed with the TimeTagger Ultra (Swabian Instruments).

A limitation of the current experimental configuration, where the sample is mounted on the side to collect photon emission from the waveguide end, is the lack of optical access to the top of the resonator, precluding individual excitation of the emitters with free-space beams.

### 3.3.3 Purcell enhancement of coherent $V_{Si}$ emitters

In order to observe Purcell enhancement, the microresonator modes are tuned spectrally via argon gas condensation. A pulsed femtosecond laser centered at 740 nm is used to uniformly excite the emitters in the disk: it couples to all resonator modes simultaneously, owing to its broad spectrum. As the microresonator is gas-tuned, an enhancement of emission at the  $V_{Si}$  ZPL wavelength of 916.5 nm (as observed via a spectrometer) indicates Purcell enhancement of one or more  $V_{Si}$ .

A representative gas-tuning spectrum upon above-resonant excitation with an 80 MHz fs laser, without narrowband spectral filtering of emission is shown in Fig. 3.7. The high background photon rate arises because the entire volume of the disk resonator has to be excited in order to excite the two emitters, due to the lack of free-space optical access to the disk. Selective excitation of emitters from above via free-space optical beams would drastically reduce background fluorescence. The background-subtracted ZPL detection rate at saturation is 0.8 MHz. As investigated below, two emitters are present in this device, so this photon detection rate corresponds to a single-emitter ZPL detection rate of 0.4 MHz in the case of equal coupling, and higher in reality due to unequal cavity-coupling rates (as shown below).

With a resonator mode parked at the Purcell enhancement condition, we measure the absorption lines of the coupled emitters via photoluminescence excitation (PLE), where a weak (0.5 pW in the waveguide) continuous-wave resonant laser is scanned across the ZPL while detecting the phonon sideband (PSB) of the emitters. A PLE scan shows that in this device, two emitters are coupled to the cavity (Fig. 3.8b), henceforth labeled emitters A and B. The  $V_{Si}$  is known to feature two spin-preserving optical transitions,  $A_1$  and  $A_2$ , split by 1 GHz [11]. We perform experiments with a weak off-axis external magnetic field that mixes the ground-state spins and eliminates resonant-laser-induced spin-polarization. We focus our study on the  $A_2$  transition of each emitter, which is brighter due to its higher

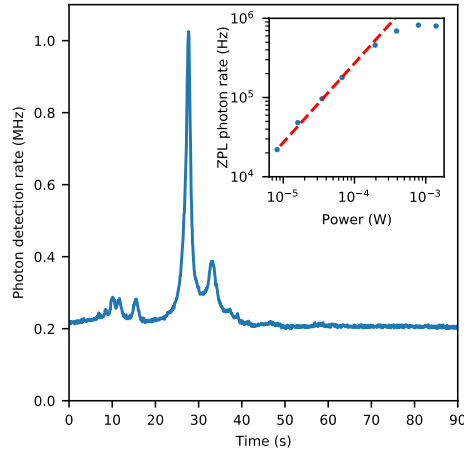


Figure 3.7: **Gas tuning and saturation of photon detection rate.** Photon detection rate in a 20 nm spectral window (910-930 nm) around the  $V_{Si}$  ZPL during continuous red-tuning of the microdisk resonance wavelength via gas condensation. The Purcell enhancement condition is observed as a sharp peak in time. Smaller peaks correspond to weaker coupling to other detuned emitters. Excitation is performed with a 730 nm, 80 MHz repetition rate femtosecond laser (0.79 mW power measured before the objective). Inset shows background-subtracted peak ZPL photon detection rate for varying laser power.

quantum efficiency[11]. We optimize the magnetic field orientation to reduce the relative intensity of the  $A_1$  transition upon resonant driving through coherent population trapping of the  $\text{spin-}\frac{3}{2}$  sublevels. Through the absence of a cavity transmission dip, we conclude that the resonator mode is strongly undercoupled to the waveguide. To observe the cavity lineshape, we measure the cavity photoluminescence noise by scanning across the resonance with higher laser power (1.5  $\mu\text{W}$  in the waveguide) and extract a loaded quality factor of  $1.3 \cdot 10^5$  (Fig. 3.8b).

The emitter-cavity coupling rate is a key metric for cavity quantum electrodynamics systems. We determine coupling strength of each emitter to the cavity by measuring the emitter lifetime reduction on resonance (Purcell enhancement). First, we selectively ionize one emitter into the dark state via strong resonant excitation, and tune the cavity on-resonance with the remaining bright emitter. We then excite the emitter with 150 ps resonant pulses (obtained via pulse-shaping a mode-locked Ti:Sapphire laser) through the cavity mode and detect the transient ZPL emission using temporal filtering. As shown in Fig. 3.8(c), the on-resonance lifetime for emitter A (B) is measured to be 4.2 ns (3.5 ns),

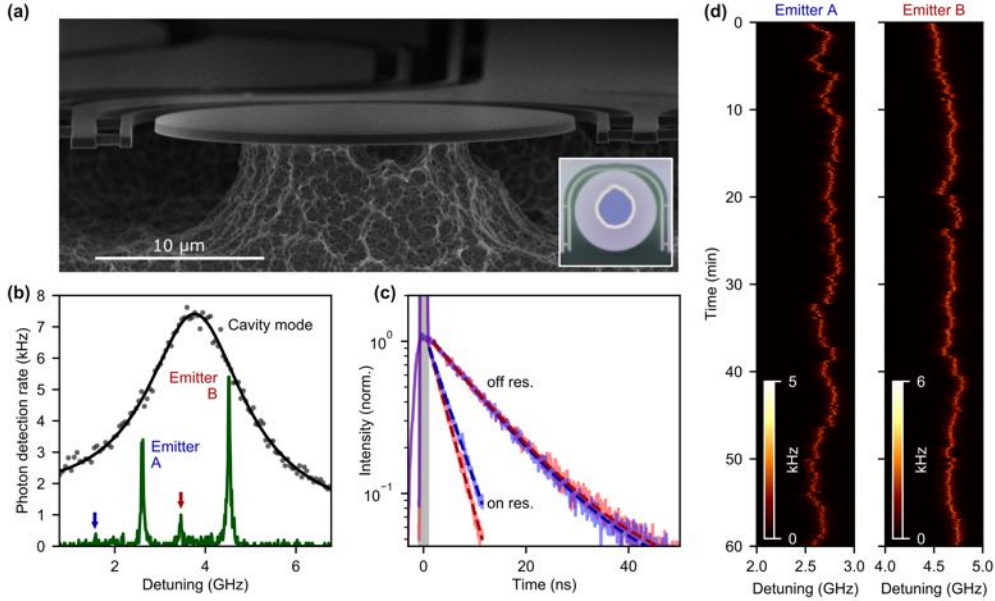


Figure 3.8: **Spectrally-stable  $V_{Si}$  emitters in integrated 4H-SiCOI photonics.** (a) Scanning electron micrograph of the device. A waveguide, which wraps around the disk (seen in the optical microscope image, inset), is coupled to the resonator. A microscope objective is used to couple light to and from the flat facets of the waveguide. (b) A cavity photoluminescence spectrum (emitter PLE spectrum) in black (green), taken with a scanning resonant laser with  $1.5 \mu\text{W}$  ( $0.5 \text{ pW}$ ) of power in the waveguide. We extract a loaded cavity quality factor of  $Q = 1.3 \cdot 10^5$ . The prominent peaks at 2.7 and 4.5 GHz detuning are the  $A_2$  transitions of the two emitters. The corresponding  $A_1$  transitions are labelled with arrows. In this figure and the rest of this chapter, the laser detuning is relative to  $327.113 \text{ THz}$  ( $916.5 \text{ nm}$ ). (c) Lifetime measurements for emitter A (blue) and emitter B (red) on- and off-resonance with the cavity. The gray region represents the excitation pulse. (d) A 1-hour PLE scan of each emitter (while the other is selectively ionized into the dark state), with the cavity positioned on-resonance with the emitter.

which corresponds to a lifetime reduction of 2.7 (3.2) from the bulk lifetime of  $11.3 \text{ ns}$  [101].

The Purcell factor of the emitter-cavity system is defined as the ratio of the rate of emission into the cavity to the unmodified ZPL decay rate. Using the radiative lifetime of the  $A_2$  transition of  $15.9 \text{ ns}$ , [101] and DWF of 8.5% [191, 165] from the literature, we conclude that the unmodified ZPL rate of the  $A_2$  transition is  $1/186.5 \text{ ns}^{-1}$ . From the non-radiative rate from the  $A_2$  transition of  $40 \text{ ns}^{-1}$ , we obtain the on-resonance cavity emission rate for emitter A (B) of  $1/5.1 \text{ ns}^{-1}$  ( $1/6.7 \text{ ns}^{-1}$ ). From this, we obtain Purcell enhancement of 28 and 37 for emitter A and B, respectively. From the simulated mode volume of  $128(\frac{\lambda}{n})^3$

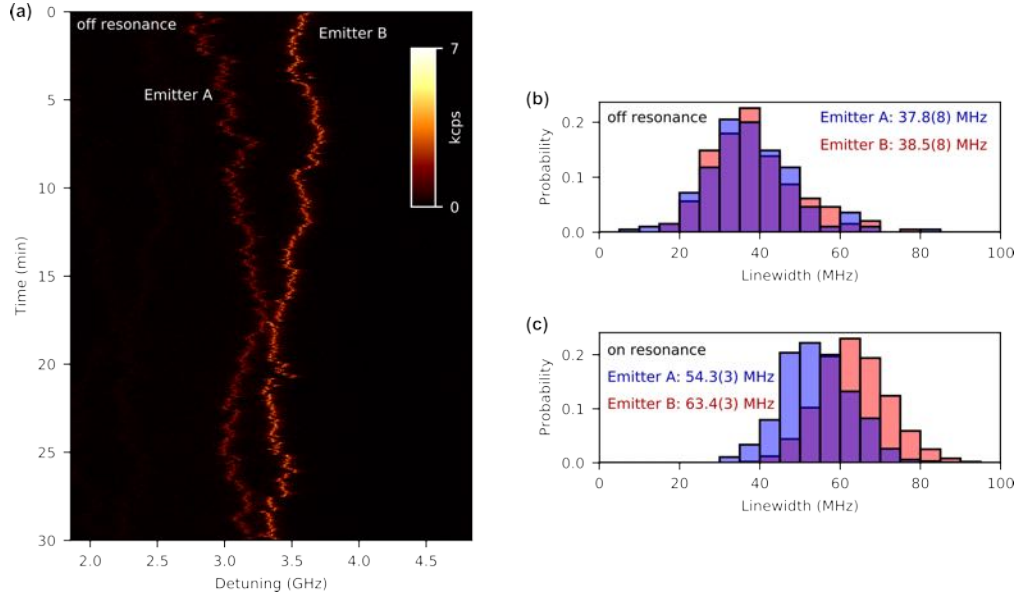


Figure 3.9: **Emitter linewidths on- and off-resonance with the cavity.** (a) A continuous PLE scan of the two emitters with the cavity far-detuned. (b) A histogram of fitted single-scan linewidths. Indicated in the figure is the mean fitted linewidth and its standard error. (c) Histogram of time-averaged scans for PLE data presented in Fig. 1(d) of the main text, showing spectral broadening caused by lifetime reduction of the optical transition. Emitter B transition is broader due to the stronger Purcell enhancement.

for the fundamental  $TM_{00}$  mode, we find the theoretical maximum Purcell enhancement of 77 in this device. The observed Purcell enhancement is comparable to that achieved in the first integrations of the diamond silicon vacancy[170, 221] and tin vacancy[156, 95] into photonic crystal nanobeam cavities, despite the much stronger mode confinement of those devices. We attribute this to the optimal dipole overlap of the  $V_{Si}$  with the cavity  $TM$  mode and the less stringent emitter positioning requirements of the microdisks. Via resonant pulsed excitation with 1 ns long pulses (generated from a continuous-wave laser using electro-optic amplitude modulation) and detection of the PSB emission with the cavity detuned by  $-80$  GHz, we measure the off-resonant lifetime of emitter A (B) to be 10.7 ns (11.1 ns). The minor discrepancy between the off-resonant lifetimes and the bulk lifetime (11.3 ns) is attributed to the coupling of the emitters to other modes of the microdisk.

Although Purcell enhancement has been observed in several color center platforms[38, 21, 170, 221, 156], including thin-film diamond[60] and SiC[110], to date cavity-coupled color centers that retain their optical coherence have only been demonstrated in bulk-carved

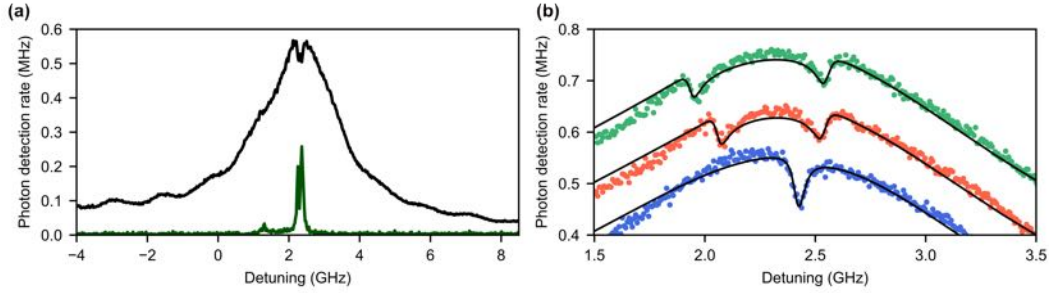


Figure 3.10: **Dipole induced transparency (DIT) in SiC.** (a) A wide laser scan across the cavity resonance, showing the transmission spectrum through the device (black). The  $V_{Si}$  phonon sideband emission is simultaneously detected (green, multiplied by 50x). Excitation of the resonator mode is performed through a scattering imperfection on the disk edge and transmission through the waveguide is detected. (b) Close-up scan at the cavity center for different emitter detunings. Orange and green traces are offset by +0.1 and +0.2 MHz, respectively.

diamond[170, 52]. To quantify the optical coherence and the spectral stability of the  $V_{Si}$  in 4H-SiCOI microdisks, we perform continuous PLE scans on each emitter while on- and off-resonance with the cavity. The on-resonance PLE scans are shown in Fig. 3.8(d). Emitters A and B were measured at different times, and the cavity has been centered on the measured emitter before the start of each one-hour acquisition. Over the course of one hour, no emitter ionization is observed, and spectral wandering is below 500 MHz. The average single-scan optical transition linewidth for emitter A (B) is found to be 54.3(3) MHz (63.4(3) MHz), which corresponds to 17 MHz (18 MHz) of spectral diffusion beyond the transform limit. Repeating the measurement off-resonance, we find the emitter A (B) linewidth to be 37.8(8) MHz (38.5(8) MHz), which corresponds to 24 MHz of spectral diffusion beyond the transform limit (Fig. 3.9). The reduced spectral diffusion on-resonance may be due to a decreased rate of excitation of surface-related defects, because the well-confined TM cavity mode is efficiently excited with low laser power. These results indicate excellent spectral stability of the nanophotonics-integrated  $V_{Si}$ .

### 3.3.4 Approaching cooperativity of unity in SiC

From the measured Purcell enhancement and off-resonant emitter linewidths, we can calculate the emitter-cavity cooperativity,  $C$ , which is the ratio of the rate of the emitter

interaction with the cavity and the total rate of other emission and decoherence processes in the system. The regime  $C \gg 1$  enables cavity-assisted deterministic emitter-photon interactions.

The cooperativity of the emitter-cavity system is given by

$$C = \frac{4g^2}{\kappa\gamma} \equiv \frac{\Gamma}{\gamma} \quad (3.1)$$

where  $g$  is the single-photon Rabi frequency,  $\kappa$  is the cavity decay rate,  $\gamma$  is the total decay rate of the emitter, and  $\Gamma$  is the rate of emission into the cavity. In Fig. 3.9, we measure averaged off-resonant linewidths of  $\gamma_A/2\pi = 37.8$  MHz and  $\gamma_B/2\pi = 38.6$  MHz for the two emitters. In Fig. 3.8, we measure the on-resonant optical transition lifetimes to be  $\tau_A = 4.2$  ns and  $\tau_B = 3.5$  ns. The lifetime of the  $A_2$  optical transition of the  $V_{Si}$  in bulk crystal is known to be  $\tau_0 = 11.3$  ns[101]. We infer  $\Gamma_A/2\pi = 23.8$  MHz and  $\Gamma_B/2\pi = 31.4$  MHz from the relation  $1/\tau_i = \Gamma_i + 1/\tau_0$  and using Eq. 3.1 calculate cooperativities for the two emitters of  $C_A = 0.6$  and  $C_B = 0.8$ . Using the measured  $\kappa/2\pi = 2.8$  GHz, we determine  $g_A/2\pi = 125$  MHz and  $g_B/2\pi = 150$  MHz. This regime enables the observation of dipole-induced transparency (DIT)[195], where the  $V_{Si}$  scatter photons from an input coherent state. Because the device studied here is strongly under-coupled to the bus waveguide, DIT is difficult to observe through waveguide transmission. We instead excite the disk through a scattering point on its edge, and detect emission into the waveguide, thus in effect performing the measurement in a drop-port configuration[195]. Scanning the continuous-wave laser across the disk resonance, DIT dips for both emitters are clearly observed, shown in Fig. 3.10. The slow spectral drift of the emitters allows us to measure DIT for different relative detunings. Looking forward, spin initialization, targeted emitter placement, and cavities with a larger  $Q/V$  metric [110, 174] will enable stronger transmission contrast in DIT for the realization of spin-photon entanglement and spin-readout via the modification of cavity reflectivity [52, 17].

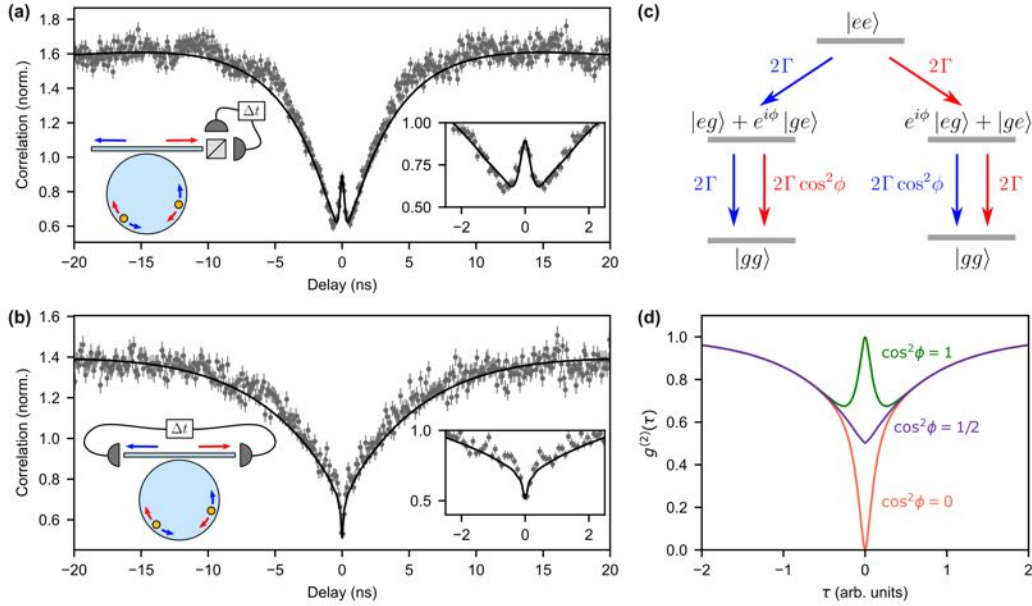


Figure 3.11: **Superradiant emission of two  $V_{Si}$  color centers.** (a) Second-order correlation of the photon emission along one waveguide direction displays bunching at zero time delay, a signature of superradiance. Inset: zoom-in of the superradiance feature. (b) The relative phase  $\phi$  of the emitters impacts the cross-correlation photon statistics between the opposite waveguide directions and can produce anti-bunched emission. The solid line in a,b is the numerical fit based on a five-level model[101] of the  $V_{Si}$ . (c) The level structure representing the pair of two-level-system emitters decaying into degenerate clockwise (red arrows) and counterclockwise (blue arrows) optical modes. The corresponding transition rates are indicated next to the arrows, where  $\Gamma$  is the unmodified single-emitter decay rate into a propagating mode. (d) Theoretically-predicted phase-dependent cross-correlation between clockwise and counterclockwise modes for a pair of ideal two-level emitters.

### 3.4 Photon interference between two SiC color centers

Photon interference between two color centers, a prerequisite for the generation of remote spin-spin entanglement, has been an outstanding challenge in silicon carbide. Here, we demonstrate two-photon interference between two microdisk-integrated emitters, which arises from their collective coupling to the same cavity mode. To observe photon interference in the continuous wave regime, an above-resonant laser is coupled to a resonator mode around 730 nm to excite both emitters. We note that while above-resonant excitation in bulk crystal has been used to obtain nearly transform-limited photon emission from the  $V_{Si}$ [129], we observe that in nanostructures it induces rapid spectral diffusion due to

disturbance of the surface charge environment, broadening the optical linewidths to approximately 0.5 GHz. This spectral instability reduces the rate of superradiant emission (however, optical coherence may be preserved using resonant excitation, as shown in the following section). Fig. 3.11(a) shows the second-order auto-correlation  $g^{(2)}(\tau)$  of the color centers' collective emission in the Hanbury Brown and Twiss configuration, where emission into the waveguide is split between two detectors via a beamsplitter. The sharp peak at zero time delay is a signature of superradiant emission and the probabilistic generation of entanglement between the two color centers. This feature has also been observed with up to three waveguide-integrated quantum dots [83, 65] and a pair of waveguide-integrated silicon vacancy centers in diamond [170, 117]. In contrast, for cross-correlations between the two waveguide propagation directions, an anti-bunching interference dip is observed (Fig. 3.11(b)). This feature is indicative of photon pairs preferentially leaving the resonator in the same direction.

The experimentally-observed photon statistics are explained by the out-of-phase coupling of the two emitters to a pair of degenerate clockwise and counterclockwise optical modes of the resonator. The interaction Hamiltonian for this system can be written as

$$H_I = g_A \sigma_A^\dagger S_A + g_B \sigma_B^\dagger S_B + \text{h.c.}, \quad (3.2)$$

where  $\sigma_A$  and  $\sigma_B$  are the lowering operators for emitters A and B, respectively, and  $g_A$  and  $g_B$  are the emitter-cavity coupling strengths; each emitter couples to its own standing wave supermode  $S_A = (a_{CW} + a_{CCW})/\sqrt{2}$  and  $S_B = (e^{-i\phi}a_{CW} + e^{i\phi}a_{CCW})/\sqrt{2}$ , where  $a_{CW}$  ( $a_{CCW}$ ) is the clockwise (counterclockwise) resonator propagating mode, and phase  $\phi$  corresponds to the emitters' azimuthal separation in the resonator. Consider two special cases: (i) for  $\phi = (0 \bmod \pi)$ ,  $S_A = \pm S_B$  and the two emitters couple to the same standing wave mode, resulting in a single-mode interaction [52]; (ii) for  $\phi = (\pi/2 \bmod \pi)$ ,  $S_A$  and  $S_B$  are orthogonal, and in the standing wave basis the emitters are de-coupled. However, because the measurement is performed in the propagating mode basis  $\{a_{CW}, a_{CCW}\}$  (corresponding to emission to the right and to the left, respectively), the pair of emitters exhibits interference for all values of  $\phi$ . For  $(\phi \bmod \pi) \neq 0$ , the cross-correlation between the two waveguide propagation directions will reveal interference features unique to a multi-mode,

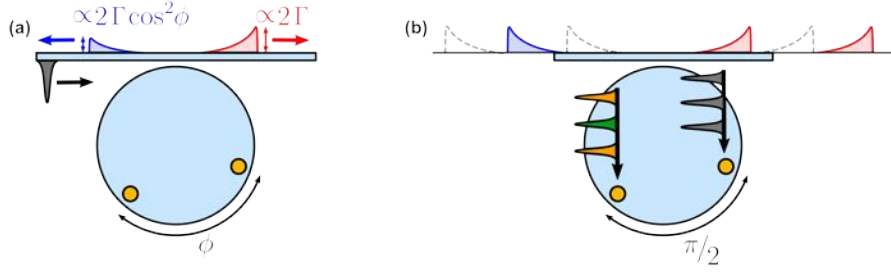


Figure 3.12: **Manipulating the single-photon emission of a pair of emitters.** (a) Weakly exciting the emitters with a resonant pulse (grey) through the CW mode will prepare the system in the superposition  $(e^{i\phi}|eg\rangle + |ge\rangle)/\sqrt{2}$ , which will result in asymmetric emission rates. (b) By independently controlling the excitation phase of the two emitters positioned such that  $\phi = \pi/2$ , the microresonator incorporates the functionality of a single-photon router. The phase of the free-space excitation pulse is represented by the color, where green, grey, and orange correspond to  $\pi/2$ , 0, and  $-\pi/2$ , respectively.

multi-emitter system.

The collective emission behavior can be understood via a cascaded decay diagram shown in Fig. 3.11(c). Starting with the two-emitter excited state  $|ee\rangle$ , emission into the clockwise mode projects the emitters into the superposition state  $(e^{i\phi}|eg\rangle + |ge\rangle)/\sqrt{2}$ . From this state, decay via clockwise emission proceeds with the superradiant rate  $2\Gamma$ , where  $\Gamma$  is the unmodified single-emitter decay rate into a propagating mode. In contrast, the rate of counterclockwise emission is modified by  $\cos^2\phi$ , as follows from the transition amplitude  $\langle gg|(e^{i\phi}\sigma_A + \sigma_B)(e^{i\phi}|eg\rangle + |ge\rangle)/\sqrt{2}$ . When  $\cos^2\phi = 0$ , photons leave the resonator always in the same direction, which corresponds to perfect antibunching in the cross-correlation. For  $\cos^2\phi = \pm 1$ , the cross-correlation is identical to the autocorrelation on a single waveguide direction. These cases are illustrated in Fig. 3.11(d). The correlation measurements (Fig. 3.11(a,b)) are fit to a reduced five-level emitter model[101] with free parameters of excitation power,  $\phi$ , cavity detuning, and background noise. The presence of background noise from the above-resonant excitation reduces the interference contrast.

Excitation of emitters via above-resonant optical fields increases spectral diffusion and is compatible neither with spin-selective excitation nor optical coherent control. To overcome this, we use resonant excitation to coherently manipulate the two-emitter superposition in the single photon subspace, a regime which has enabled pioneering quantum network

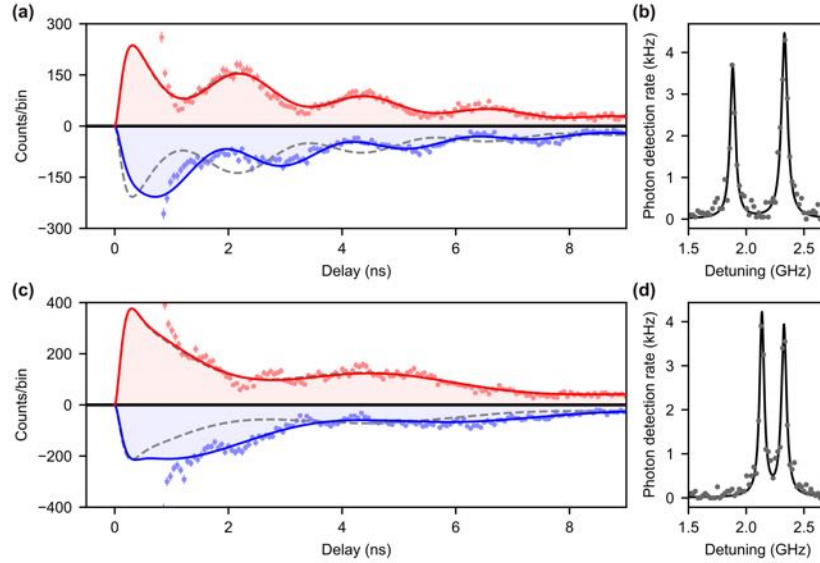


Figure 3.13: **Chiral single-photon scattering from a pair of emitters in a WGM resonator** (a) The emitter pair is excited through the CW mode. Photons scattered into the CW (red) and CCW (blue) mode are time-correlated to the excitation pulse, tracing out the temporal shape of the emitted single-photon wavepacket. The solid red and blue lines represent the simulated expectation values  $\langle a_{CW}^\dagger a_{CW} \rangle$  and  $\langle a_{CCW}^\dagger a_{CCW} \rangle$ , respectively. The asymmetric CW and CCW emission arises from non-trivial emitter phase difference, inferred to be  $(0.34\pi \bmod \pi)$ . The simulated case where  $\phi = 0$  is shown as a grey dotted curve, in which case the emission is symmetric. (b) The PLE spectrum of the two emitters shows frequency separation of 0.44 GHz, which is used as a fixed parameter in the simulation of the wavepacket in (a). (c,d) Same as panels (a,b) but for emitter frequency separation of 0.19 GHz, with inferred phase  $\phi = (0.28\pi \bmod \pi)$ .

experiments with NV centers in diamond [76, 145]. Consider exciting the two emitters through the waveguide via fast resonant pulses in the clockwise direction (Fig. 3.12(a)). In the bad-cavity regime ( $\kappa \gg \gamma$ ) and with resonator finesse  $\mathcal{F} \gg 1$ , if the two emitters are initially in the ground state  $|gg\rangle$ , a pulse instantaneously prepares the system into a superposition state

$$|\psi\rangle = (1 - P_e) |gg\rangle + \sqrt{P_e(1 - P_e)}(e^{i\phi} |eg\rangle + |ge\rangle) + P_e e^{i\phi} |ee\rangle, \quad (3.3)$$

where  $P_e$  is the single-emitter excitation probability. In the weak excitation limit ( $P_e \ll 1$ ), the probability of double-excitation is negligible, and the system is prepared in the superposition  $(e^{i\phi} |eg\rangle + |ge\rangle)/\sqrt{2}$  conditioned on the detection of a scattered photon. This

corresponds to the preparation of the two-emitter system into the intermediate level of the diagram in Fig. 3.11(c). The emission from this state will proceed superradiantly in the clockwise direction independent of  $\phi$ , but the back-scattering rate will be modified by  $\cos^2 \phi$  (Fig. 3.12(a)). For  $\phi = \pi/2$ , complete directionality is achieved. This is analogous to classical chiral scattering observed in WGM resonators coupled to a pair of dielectric[141] and plasmonic[37] nanostructures. The  $\phi = \pi/2$  condition can be used to implement routing of single photons from an emitter pair (Fig. 3.12(b)) and, as shown in the following section, enables efficient spin-spin entanglement protocols. We note that due to the cavity-mediated coupling of emitters, collective scattering of input light is strengthened in the high-cooperativity regime, whereas in a waveguide system high-cooperativity emitters will act as individual strong scatterers.

The combination of preserved optical coherence and spectral stability enables the experimental realization of single-photon interference between two  $V_{Si}$  emitters, shown in Fig. 3.13. Because the emitters' transitions are not degenerate, their relative phase will precess at the rate equal to their frequency difference, which is observed as an oscillation in the single-photon wavepacket. Notably, the phase difference in the oscillations of CW and CCW emission originates from the relative emitter phase  $\phi$ . As described below, the non-unity contrast of the oscillations is due to the distribution of the spin population across the bright spin- $\frac{1}{2}$  and dark spin- $\frac{3}{2}$  manifolds (corresponding to the optical transitions  $A_2$  and  $A_1$ , respectively). The oscillations persist throughout the entire wavepacket, confirming nearly transform-limited photon emission, essential for interference-based entanglement generation[76]. The smaller amplitude oscillation with a 1 ns period is due to incomplete suppression of the  $A_1$  emission line of the  $V_{Si}$  (Fig. 3.8(b)). The free parameters in the numerical model are cavity detuning,  $\phi$ , and the population of the spin- $\frac{1}{2}$  manifold. From the numerical fit, the spin population is inferred to be unpolarized, as expected in an off-axis magnetic field. The relative emitter phase inferred from the data in Fig. 3.13(a) and 3.13(c) is  $\phi = (0.34\pi \bmod \pi)$  and  $\phi = (0.28\pi \bmod \pi)$ , respectively. We note that  $\phi$  was observed to drift in time, attributed to nonuniform deposition of water ice on the resonator as a result of the asymmetric resonator undercut geometry. This explanation is consistent with the observed slow systematic drift of emitter spectral separation by approximately 1 GHz

per day due to strain from the ice.

The present study of the cavity quantum electrodynamics of a color center pair in a microdisk resonator suggests that despite a typically lower quality factor-to-mode volume ratio ( $Q/V$ ) than high-confinement photonic crystal cavities, WGM resonators may offer unique capabilities and warrant further consideration for applications in chip-integrated quantum information processing. As we show below, the two-emitter chiral scattering at the  $\phi = \pi/2$  condition enables efficient entanglement generation via single-photon interference. Through integration with a color center that exhibits two orthogonal circularly polarized transitions such as the divacancy in silicon carbide, the microdisk could be used to realize single-emitter chiral light-matter interaction[163, 105]. Furthermore, the microdisk is a promising platform for near-term many-body quantum optics demonstrations with solid state spins, as many individually-addressable and spectrally-tunable emitters may be integrated into a single resonator[111].

### 3.4.1 Two-emitter single photon interference modeling

The modeling of the single-photon temporal envelope shown in Fig. 3.13 is performed using QuTiP based on a simplified three-level model, where the bright ground state spin- $\frac{1}{2}$  manifold is treated as one state,  $|\uparrow\rangle$ , coupled to one excited state,  $|e\rangle$ . This is an appropriate approximation because all optical transitions within the spin- $\frac{1}{2}$  manifold are near-degenerate and so the fine structure does not impact the photon emission. Additionally, a third state is introduced  $|\downarrow\rangle$ , which represents the dark spin population which is not excited by the optical excitation pulse. This model thus includes the effect of the dark spin population on the interference.

The first step is to calculate the two-emitter state upon the – assumed instantaneous – weak coherent excitation. Before the application of a weak optical excitation pulse, the two-emitter system is in a mixed state

$$\rho_0 = (1 - P_B)^2 |\downarrow\rangle\langle\downarrow| + P_B^2 |\uparrow\rangle\langle\uparrow| + P_B(1 - P_B)(|\uparrow\rangle\langle\downarrow| + |\downarrow\rangle\langle\uparrow|),$$

where  $P_B$  is the population fraction of the bright state  $|\uparrow\rangle$ .

The excitation with a weak optical pulse results in a mixture of four pure states

$$\rho_e = |\psi_1\rangle\langle\psi_1| + |\psi_2\rangle\langle\psi_2| + |\psi_3\rangle\langle\psi_3| + |\psi_4\rangle\langle\psi_4|,$$

where

$$\begin{aligned}\psi_1 &= (1 - P_B) |\downarrow\downarrow\rangle \\ \psi_2 &= P_B \left( e^{i\phi} P_e |ee\rangle + (1 - P_e) |\uparrow\uparrow\rangle + \sqrt{P_e(1 - P_e)} (e^{i\phi} |e\uparrow\rangle + |\uparrow e\rangle) \right) \\ \psi_3 &= \sqrt{P_B(1 - P_B)} \left( e^{i\phi} \sqrt{P_e} |e\downarrow\rangle + \sqrt{1 - P_e} |\uparrow\downarrow\rangle \right) \\ \psi_4 &= \sqrt{P_B(1 - P_B)} \left( \sqrt{P_e} |\downarrow e\rangle + \sqrt{1 - P_e} |\downarrow\uparrow\rangle \right)\end{aligned}$$

In the weak-excitation regime, ( $P_e \rightarrow 0$ ), double excitation  $|ee\rangle$  can be neglected. Furthermore, all zero-excitation terms can be discarded, as they will be annihilated by the photon detection superoperator  $\mathcal{J}[|0\rangle\langle 1|]$  where  $\mathcal{J}[A]B = ABA^\dagger$ . Then, the initial excited state is simplified to:

$$\rho_e = P_B^2 P_e (1 - P_e) (e^{i\phi} |e\uparrow\rangle + |\uparrow e\rangle) (e^{i\phi} \langle e\uparrow| + \langle \uparrow e|) + P_B (1 - P_B) P_e (|e\downarrow\rangle\langle e\downarrow| + |\downarrow e\rangle\langle \downarrow e|)$$

With  $P_e \ll 1$ ,  $P_e \approx P_e(1 - P_e)$ , and, disregarding normalization of the state:

$$\rho_e = P_B^2 (e^{i\phi} |e\uparrow\rangle + |\uparrow e\rangle) (e^{i\phi} \langle e\uparrow| + \langle \uparrow e|) + P_B (1 - P_B) (|e\downarrow\rangle\langle e\downarrow| + |\downarrow e\rangle\langle \downarrow e|)$$

The term  $P_B^2 (e^{i\phi} |e\uparrow\rangle + |\uparrow e\rangle) (e^{i\phi} \langle e\uparrow| + \langle \uparrow e|)$  corresponds to the case of two emitters interfering perfectly. The term  $P_B (1 - P_B) (|e\downarrow\rangle\langle e\downarrow| + |\downarrow e\rangle\langle \downarrow e|)$  corresponds to a solitary excited emitter in the cavity, with the other emitter in the dark state, in which case no interference takes place. The contribution of this term reduces the interference contrast, and one can see that the contrast is minimized for the maximally mixed state ( $P_B = 0.5$ ).

With the initial condition  $\rho(0) = \rho_e$ , the system is evolved in time:

$$\partial_t \rho = \mathcal{L}\rho = -i[H, \rho] + \sum_L \mathcal{D}[L]\rho,$$

where

$$H = (\omega_0 + \Delta - \delta/2)\sigma_1^\dagger\sigma_1 + (\omega_0 + \Delta + \delta/2)\sigma_2^\dagger\sigma_2 + \omega_0(a_{\text{CW}}^\dagger a_{\text{CW}} + a_{\text{CCW}}^\dagger a_{\text{CCW}}) + [g_1 S_1^\dagger\sigma_1 + g_2 S_2^\dagger\sigma_2 + \text{h.c.}],$$

$$L \in \{\sqrt{\gamma_1}\sigma_1, \sqrt{\gamma_2}\sigma_2, \sqrt{\kappa}a_{\text{CW}}, \sqrt{\kappa}a_{\text{CCW}}, \sqrt{\gamma_{d_1}}\sigma_1^\dagger\sigma_1, \sqrt{\gamma_{d_2}}\sigma_2^\dagger\sigma_2\},$$

where  $\gamma_{d_i}$  is the pure dephasing rate of emitter  $i$ ; and

$$\mathcal{D}[L]\rho = L\rho L^\dagger - \frac{1}{2}(L^\dagger L\rho + \rho L^\dagger L).$$

The temporal photon wavepacket shape in the clockwise and counterclockwise direction is then given by the time-dependent expectation value of the cavity-decay number operators  $\text{Tr}[\kappa a_{\text{CW}}^\dagger a_{\text{CW}}\rho(t)]$  and  $\text{Tr}[\kappa a_{\text{CCW}}^\dagger a_{\text{CCW}}\rho(t)]$ , respectively.

### 3.4.2 Entanglement protocol between two emitters with $\phi = \pi/2$

As discussed above and illustrated in Fig. 3.12(a), for a pair of two-level systems coupled to a WGM resonator with a relative phase  $\phi = \pi/2$ , upon weak coherent excitation through the clockwise (counterclockwise) mode, the emitters scatter photons only in the clockwise (counterclockwise) direction; back-scattering is forbidden due to destructive interference. If, however, the emitters possess a fine structure in the ground state and spin-selective optical transitions, back-scattering is possible from a particular two-emitter Bell state, and a detection of a back-scattered photon heralds entanglement generation.

Consider an emitter with an optical transition between states  $|\uparrow\rangle$  and  $|e\rangle$ , as well as an additional spin state  $|\downarrow\rangle$ , which is not affected by the optical driving of the  $|\uparrow\rangle \leftrightarrow |e\rangle$  transition. The first step of the entanglement protocol is spin initialization of both emitters (for instance in state  $|\uparrow\uparrow\rangle$ ), followed by spin control to prepare each emitter in an equal superposition state

$$|\psi_0\rangle = \frac{1}{2}(|\uparrow\rangle + |\downarrow\rangle)_A(|\uparrow\rangle - |\downarrow\rangle)_B.$$

Selective excitation of the emitters' bright spin state with a weak optical pulse produces

the state

$$|\psi_e\rangle = \frac{1}{2} \left( e^{i\pi/2} \sqrt{P_e} |e\rangle + \sqrt{1-P_e} |\uparrow\rangle + |\downarrow\rangle \right)_A \left( \sqrt{P_e} |e\rangle + \sqrt{1-P_e} |\uparrow\rangle - |\downarrow\rangle \right)_B,$$

where  $P_e$  is the excitation strength, corresponding to the probability of preparing an emitter into the excited state. Expanding:

$$\begin{aligned} |\psi_e\rangle = & \frac{1}{2} \left( e^{i\pi/2} P_e |ee\rangle + (1-P_e) |\uparrow\uparrow\rangle - |\downarrow\downarrow\rangle + \right. \\ & \left. \sqrt{P_e(1-P_e)} (e^{i\pi/2} |e\uparrow\rangle + |\uparrow e\rangle) + \sqrt{P_e} (-e^{i\pi/2} |e\downarrow\rangle + |\downarrow e\rangle) + \sqrt{1-P_e} (|\downarrow\uparrow\rangle - |\uparrow\downarrow\rangle) \right) \end{aligned}$$

We denote the state of the waveguide as  $|NM\rangle$ , where  $N$  and  $M$  represent the number of photons emitted backwards and forwards, respectively. We now consider the final state of the emitters and waveguide after the decay:

- The state  $e^{i\pi/2} P_e |ee\rangle$  will emit two photons, either both right or both left, so the final state is  $e^{i\pi/2} P_e (|\uparrow\uparrow 02\rangle + |\uparrow\uparrow 20\rangle) / \sqrt{2}$ .
- The state  $\sqrt{P_e(1-P_e)} (e^{i\pi/2} |e\uparrow\rangle + |\uparrow e\rangle)$  will emit forward only, so the final state is  $\sqrt{2P_e(1-P_e)} |\uparrow\uparrow 01\rangle$ .
- The state  $\sqrt{P_e} (e^{-i\pi/2} |e\downarrow\rangle + |\downarrow e\rangle)$  will emit backward only, so the final state is  $\sqrt{P_e} (|\uparrow\downarrow 10\rangle + |\downarrow\uparrow 10\rangle)$ .

The final total state is then:

$$\begin{aligned} \Psi = & \frac{1}{2} \left( e^{i\pi/2} P_e (|\uparrow\uparrow 02\rangle + |\uparrow\uparrow 20\rangle) / \sqrt{2} + (1-P_e) |\uparrow\uparrow\rangle - |\downarrow\downarrow\rangle + \right. \\ & \left. \sqrt{2P_e(1-P_e)} |\uparrow\uparrow 01\rangle - \sqrt{P_e} (|\uparrow\downarrow 10\rangle + |\downarrow\uparrow 10\rangle) + \sqrt{1-P_e} (|\downarrow\uparrow\rangle - |\uparrow\downarrow\rangle) \right) \end{aligned}$$

A photon detector that does not discriminate photon number can be modeled by a pair of measurement superoperators corresponding to “no click” and “click”:  $\{\mathcal{J}[|0\rangle\langle 0|], \Omega_{\text{click}}\}$ , where  $\Omega_{\text{click}} = \sum_{n=1}^{\infty} \mathcal{J}[|0\rangle\langle n|]$  and  $\mathcal{J}[A]B = ABA^\dagger$ . A click on a detector monitoring

back-scattered photons projects the system into the (unnormalized) state:

$$\begin{aligned} \rho_l &= \frac{1}{4} \left( \frac{P_e^2}{2} |\uparrow\uparrow\rangle\langle\uparrow\uparrow| + P_e(|\uparrow\downarrow\rangle + |\downarrow\uparrow\rangle)(\langle\uparrow\downarrow| + \langle\downarrow\uparrow|) \right) = \\ &= \frac{P_e^2}{8} |\uparrow\uparrow\rangle\langle\uparrow\uparrow| + \frac{P_e}{4} (|\uparrow\downarrow\rangle + |\downarrow\uparrow\rangle)(\langle\uparrow\downarrow| + \langle\downarrow\uparrow|) = \frac{P_e}{4} \left( \frac{P_e}{2} |\uparrow\uparrow\rangle\langle\uparrow\uparrow| + (|\uparrow\downarrow\rangle + |\downarrow\uparrow\rangle)(\langle\uparrow\downarrow| + \langle\downarrow\uparrow|) \right) \end{aligned}$$

The normalized state is then:

$$\rho_l = \frac{2}{P_e + 2} \left( \frac{P_e}{2} |\uparrow\uparrow\rangle\langle\uparrow\uparrow| + (|\uparrow\downarrow\rangle + |\downarrow\uparrow\rangle)(\langle\uparrow\downarrow| + \langle\downarrow\uparrow|) \right) = \alpha |\uparrow\uparrow\rangle\langle\uparrow\uparrow| + (1-\alpha)(|\uparrow\downarrow\rangle + |\downarrow\uparrow\rangle)(\langle\uparrow\downarrow| + \langle\downarrow\uparrow|),$$

where  $\alpha = \frac{P_e}{P_e+2}$  is the infidelity of the state. In the limit of weak excitation,  $\alpha \rightarrow P_e/2$ . Thus, photon detection heralds entanglement whose fidelity will scale with  $1 - P_e/2$ , and probability of detecting a photon will scale with  $P_e$ , a trade-off between entanglement rate and fidelity, as in reference [76].

Note that, if instead the initial state  $|\psi_0\rangle = \frac{1}{2}(|\uparrow\rangle + |\downarrow\rangle)_A(|\uparrow\rangle + |\downarrow\rangle)_B$  had been prepared, one can obtain the entangled singlet Bell state  $(|\uparrow\downarrow\rangle - |\downarrow\uparrow\rangle)$  heralded by the detection of a forward-scattered photon.

### 3.4.3 Spin selective temporally-filtered resonance fluorescence

In the single-photon interference ‘experiments above, pulsed resonant excitation to detect transient ZPL emission was performed with picosecond pulses from a mode-locked laser expanded to 150 ps via pulse shaping. With this approach, however, it is difficult to implement selective excitation of just one of the transitions, due to their small separation of 1 GHz. An alternative approach to generate spectrally narrower pulses is via electrooptic modulation. We use an electro-optic *phase* modulator combined with spectral filtering to electronically define the optical pulse shape via an arbitrary waveform generator. Generating pulses thus, rather than via an electro-optic *amplitude* modulation, achieves high rejection ratio (60 dB) and is insensitive to environmental fluctuations, not requiring any active stabilization of the modulator. Figure 3.14(a) details the experimental configuration. Using 1 ns FWHM pulses, corresponding to a 0.44 GHz FWHM in frequency, we perform temporally-filtered resonance-fluorescence on a single  $V_{S1}$ , observing well resolved  $A_1$  and  $A_2$  transitions, shown

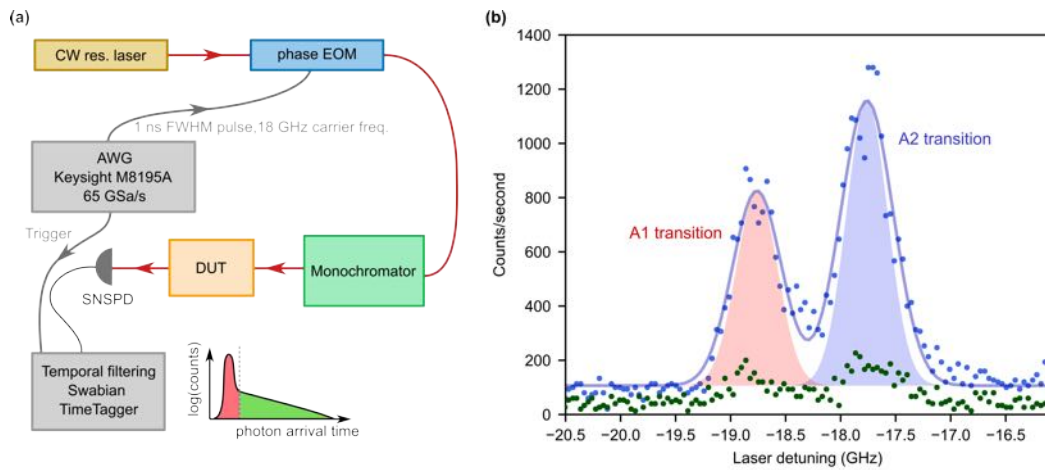


Figure 3.14: **Spin selective temporally-filtered resonance fluorescence.** (a) Diagram of the experimental configuration. Temporally-modulated laser sideband at 18 GHz is generated using a phase electro-optic modulator (EOM) driven by an arbitrary signal generator (AWG). The sideband is spectrally filtered and sent to the device. The detected photons arrival times are correlated with the excitation pulse (Swabian Time Tagger): The earlier photon arrivals corresponding to the excitation pulse are discarded. (b) Resonance fluorescence spectrum of a single  $V_{Si}$  (blue data points) taken with 1 ns FWHM excitation pulses. The shaded areas correspond to the excitation pulse transform limit (0.44 GHz FWHM). The green data points are the simultaneously-acquired phonon side-band emission. Due to the strong Purcell enhancement of the defect, the phonon side-band detection rate is significantly lower than that of the ZPL.

in Figure 3.14b.

## Chapter 4

# Electrical control of the $V_{Si}$

This chapter presents the study of electrical control of the  $V_{Si}$  via the Stark effect, both under DC and AC electrical drive. We also study the effect of AC electrical modulation on the single photon emission properties, and investigate the effect of spectral modulation on a the coherent fast orbital manipulation of a two-level system. While the experiments are performed in bulk crystal, a key motivation of the studies presented in this chapter is the integration with photonic circuits. Specifically, the photonic devices presented in the earlier chapters are immediately compatible with the methods developed in this chapter, to enable versatile and scalable control of single emitters in nanophotonic structures.

This chapter is organized as follows. First, the experimental setup and DC stark shift measurements of single  $V_{Si}$  emitters are presented, followed by the demonstration of AC electrical control of single defects enabling the generation of optical Floquet states. The spectral stability under high amplitude modulation is further shown. We then investigate the two-photon scattering properties of AC-driven emitters, and confirm that in the fast driving regime, the system behaves as a spectrally-complex but unmodulated single-photon source. Finally, we investigate the interplay of electrical driving with optical coherent control. Together these results constitute a backbone for the eventual co-integration of color centers with electrical control and photonic resonators.

## 4.1 Experimental setup

The experiments were performed using a 100  $\mu\text{m}$ -thick  $4\text{H-}^{28}\text{Si}^{12}\text{C}$  epilayer grown by chemical vapour deposition on a n-type (0001) 4H-SiC substrate. Color centers are generated via electron irradiation. In order to investigate whether the spectral stability of the  $V_{Si}$  is influenced by the electron irradiation energy, one sample was irradiated with an average energy of 2 MeV (at QST, Japan) and another at an average energy of 23 MeV (at Stanford SLAC, USA), with a dose of  $1 \cdot 10^{13} \text{ cm}^{-2}$  and  $5 \cdot 10^{12} \text{ cm}^{-2}$ , respectively. Samples were annealed for 30 minutes at  $300^\circ\text{C}$  after irradiation. Samples were diced and their edges were polished (DAG 810 from Disco Corp.). Then, 3  $\mu\text{m}$  were removed from the surface with reactive ion etching (using  $\text{SF}_6$ ), to minimize the presence of defects that arise from mechanical processing. Gold electrodes were patterned on the sample edge via e-beam lithography and liftoff. No difference in the properties of single  $V_{Si}$  was observed between the two samples; however, as expected, the higher-energy irradiation produced a greater fraction of optically-active defects of unknown origin.

The measurements are performed in a closed-cycle cryostat (Montana Instruments) at a temperature of 5 K. The sample is mounted onto a custom-built circuit board with a microwave stripline optimized for high-frequency operation. The signal is delivered onto the sample with aluminum wirebonds. The cut-off frequency of the microwave setup was measured to be 10.5 GHz. Optical spectra of the  $V_{Si}$  are measured via the PLE technique: by scanning a weak resonant laser (power at the objective lens ranging between 50 and 150 nW) across the transition, and detecting only the emission into the phonon side-band via a tunable long-pass filter (Semrock). Two-photon coincidences are recorded with timing electronics with a 10 ps resolution (Swabian Instruments). To control the charge state of the emitter, a 1  $\mu\text{s}$  above-resonant (740 nm) repump pulse is applied at a 1 kHz repetition rate. For pulsed measurements, a picosecond Ti:Sapphire laser (Spectra Physics) with a home-built pulse delay stage and an EOM-based pulse picker are used. For DC Stark tuning characterization, voltage is applied to the gold electrodes via a programmable voltage source (Keithley). Single-frequency microwave drive is delivered via a continuous-wave signal generator with 3.3 GHz bandwidth (Rhode-Schwartz). A diagram of the optical and electronic experimental setup is shown in Figures 4.1 and 4.2.

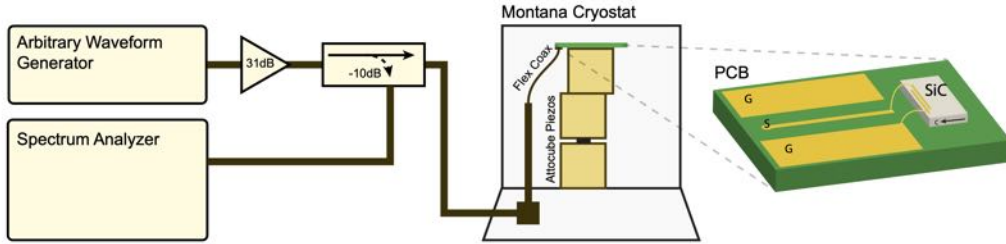


Figure 4.1: **Electrical experimental setup.** The output from an arbitrary waveform generator (Keysight) is amplified (Minicircuits) and delivered to the cryostat via SMA RF cables. The signal is sampled via a -10 dB directional coupler to verify the quality of the amplified signal. Coaxial feedthrough connections allow signal transfer to the inside of the Montana Instruments cryostat. Inside the cryostat, the signal is routed through a flexible coaxial cable to a microwave PCB with a 50 ohm transmission line that terminates open on the 4H-SiC substrate. Three attocube piezoelectric actuators allow for three-axis motion of the sample.

## 4.2 DC Stark shift

We first probe the static Stark shift of the  $V_{Si}$  by applying a voltage across gold electrodes fabricated on the  $a$ -cut surface of 4H-SiC, oriented to apply the field along the axis of symmetry of the defect, and measure the single-defect spectrum. The narrowest homogeneous linewidth emitters we observe in our sample are around 80-90 MHz, which is only three times broader than transform-limited. Narrower emitters (50-70 MHz) have been previously observed in samples with lower density of defects[129, 131, 11]. We attribute the larger linewidths in our sample to a higher electron irradiation dose used to generate defects, which has been shown to induce increased emitter linewidths[131]. As a result of minor spectral diffusion, the narrowest inhomogeneous linewidths we observe are 100 and 102 MHz for the  $k$ - and  $h$ - $V_{Si}$ , respectively.

All measurements are performed at 5 K via resonant absorption spectroscopy, *i.e.*, photoluminescence excitation (PLE). As shown in Fig. 4.3, we observe that the zero-phonon line of the  $V_{Si}$  can be tuned by 200 GHz without degradation of spectral properties: in other solid-state emitters, the degradation manifests as blinking, charge conversion, or carrier tunneling[42, 2] The  $V_{Si}$  does require the periodic application of an above-resonant laser for charge stabilization[11, 131], but we do not observe an increased rate of charge conversion with the application of a bias voltage. The static Stark shift measurement is performed by

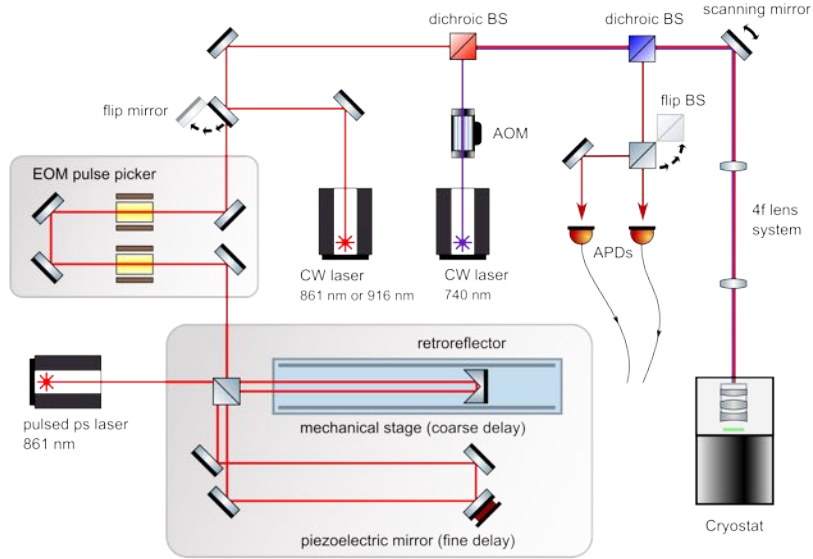


Figure 4.2: **Optical experimental setup.** For PLE measurements, a CW laser (M Squared Lasers) scanned around 861 nm or 916 nm is used to excite the color centers. APDs (Excelitas SPCM-AQRH-14) are used for single photon experiments as well as two-photon correlation (switching between two modes is done with a flip beamsplitter). A scanning confocal setup is used to spatially raster the excitation and detection spots across the sample surface to identify single emitters. For optical pulsed measurements, a picosecond pulsed laser with 80 MHz repetition rate (Spectra Physics, Tsunami) is used. For the Ramsey interference experiment, a combination of a retroreflector on a mechanical stage and a mirror mounted on a piezoelectric crystal produces a pair of pulses with precisely-controlled delay. For the Rabi oscillations experiment requiring only one pulse, one of the paths is blocked. A pair of EOMs (Conoptics, LTA Series EOM) is used for pulse-picking with a 60 dB extinction. Throughout all experiments, above resonant pulsed excitation is used to stabilize the charge of the emitter, produced using a CW laser (MBR) at 740 nm and an AOM. Abbreviations: EOM: electrooptic modulator. AOM: acoustooptic modulator. BS: beamsplitter. CW: continuous wave. APD: avalanche photodiode.

incrementing the applied voltage in steps of 0.5 V and sweeping a tunable laser, programmed to track the frequency of the  $V_{Si}$  as it shifts. From electrostatic simulation of the electrodes and the Lorentz local field approximation[185], we calculate the local electric field strength at the  $V_{Si}$  location (assuming the defect position is accurate within  $1 \mu\text{m}^3$ ), and deduce a strong Stark shift of  $3.65 \pm 0.09 \text{ GHz}/(\text{MV}/\text{m})$ . This corresponds to an electric dipole moment of  $0.72 \pm 0.02 \text{ Debye}$ , in disagreement with the theoretical prediction of 0.2 Debye[190]. We note that a recent experimental study in  $V_{Si}$  ensembles estimated the dipole moment

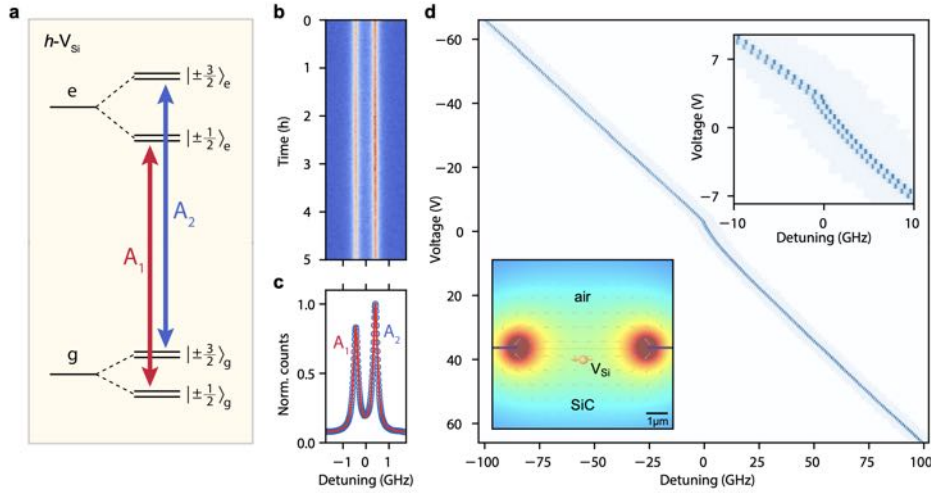


Figure 4.3: **DC Stark tuning characteristics of the  $h\text{-}V_{\text{Si}}$ .** **a** The  $h\text{-}V_{\text{Si}}$  level structure. **b** Continuous PLE measurement over the course of 5 hours. **c** The intensity of the transitions averaged over the 5-hour acquisition, revealing inhomogeneous linewidths of the  $A_1$  and  $A_2$  transitions to be 259 MHz and 273 MHz, respectively. **d**. The  $V_{\text{Si}}$  frequency is Stark tuned by 200 GHz by applying electric field parallel to the defect's symmetry axis. The detuning is relative to 347.821 THz. Left inset: electrostatic simulation of the field produced by micro-fabricated electrodes. Right inset: the 'kink' observed near bias of 0 V, also seen in the  $k\text{-}V_{\text{Si}}$ . A closer investigation of this feature is shown in Fig. 4.5.

to be 0.18 Debye[158]. Nevertheless, the wide-range, high resolution characterization of the Stark shift of single color centers presented in this work gives us confidence in the dipole moment magnitude we report.

In our experiments, we observe the linewidths of  $k\text{-}V_{\text{Si}}$  to be about 2-3 times narrower than those of the  $h\text{-}V_{\text{Si}}$ . As seen in Figs. 4.4 and 4.3, the optical transitions of both defects display excellent spectral stability, with optical transitions remaining stable over the course of many hours. From the DC Stark shift measurements of the  $k\text{-}V_{\text{Si}}$  (Fig. 4.4d), (assuming the defect position is measured to within  $1 \mu\text{m}^3$ ), we deduce a Stark shift of  $3.7 \pm 0.2 \text{ GHz}/(\text{MV}/\text{m})$ . Thus, the dipole moment of the  $k\text{-}V_{\text{Si}}$  is within the measurement uncertainty of the value for the dipole moment of the  $h\text{-}V_{\text{Si}}$ ; this is expected, given the very similar orbital structure of the  $k\text{-}$  and  $h\text{-}V_{\text{Si}}$  defects. We note that the dipole moment and Stark shift response is reported for the local field, which is calculated via the Lorentz local field approximation[185]. In the Lorentz local field approximation, the relation between the local ( $F$ ) and external ( $E$ ) field is  $F = E(\epsilon + 2)/3$ , where  $\epsilon$  is the dielectric constant of SiC

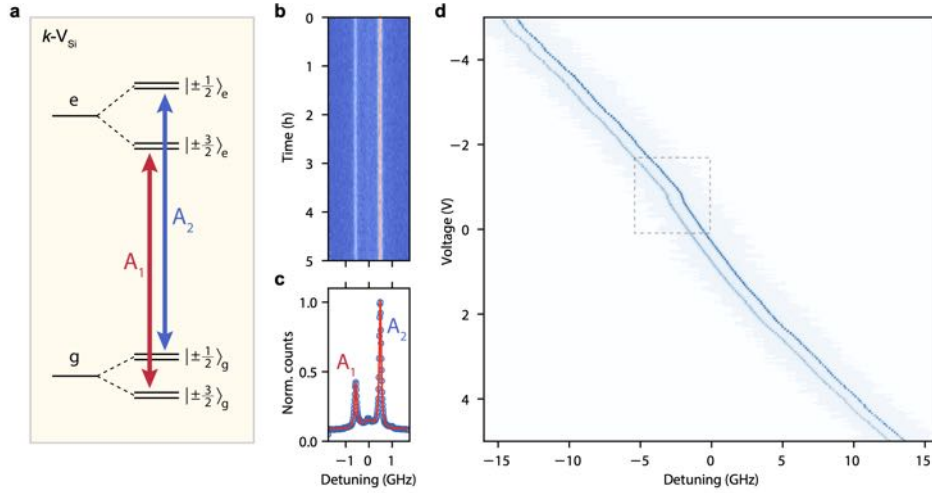


Figure 4.4: **DC Stark tuning characteristics of the  $k$ - $V_{Si}$**  **a** The  $k$ - $V_{Si}$  level structure. **b** Continuous PLE measurement over the course of 5 hours. **c** The intensity of the transitions averaged over the 5-hour acquisition, revealing inhomogeneous linewidths of the  $A_1$  and  $A_2$  transitions to be 117 MHz and 100 MHz, respectively. **d** Tuning characteristics of  $V_{Si}$  for a range of  $\pm 5$  V. The ‘kink’ is observed near 0 V as in the  $h$ - $V_{Si}$ . The range indicated by the dashed box is investigated in Fig. 4.5. The detuning is given relative to 326.908 THz.

( $\epsilon_{SiC} \approx 10$ ). Thus, from experimental considerations, the effective Stark shift of the  $V_{Si}$  is approximately 4 times higher, since the *local* field experienced by the emitter is 4 times stronger than the *external* field that is obtained from electrostatic simulation.

We investigate the ‘‘kink’’ present in the DC Stark shift tuning characteristics near 0 V, to determine whether it is caused by hysteresis. To this end, we scan continuously back and forth around the kink position. We observe that the tuning characteristics are the same for positive and negative voltage ramp, confirming the non-hysteretic nature of the kink (Fig. 4.5). We attribute it to field rectification by trapped charges, similar to what has been observed in the NV center[14].

### 4.3 Observation of Floquet states under AC drive

We then proceed to characterize the  $V_{Si}$  under Stark modulation, in order to observe spectra of Floquet eigenstates which have been previously seen in other solid state quantum emitters such as the NV and SiV centers in diamond [33, 119], the divacancy in SiC[126], and quantum

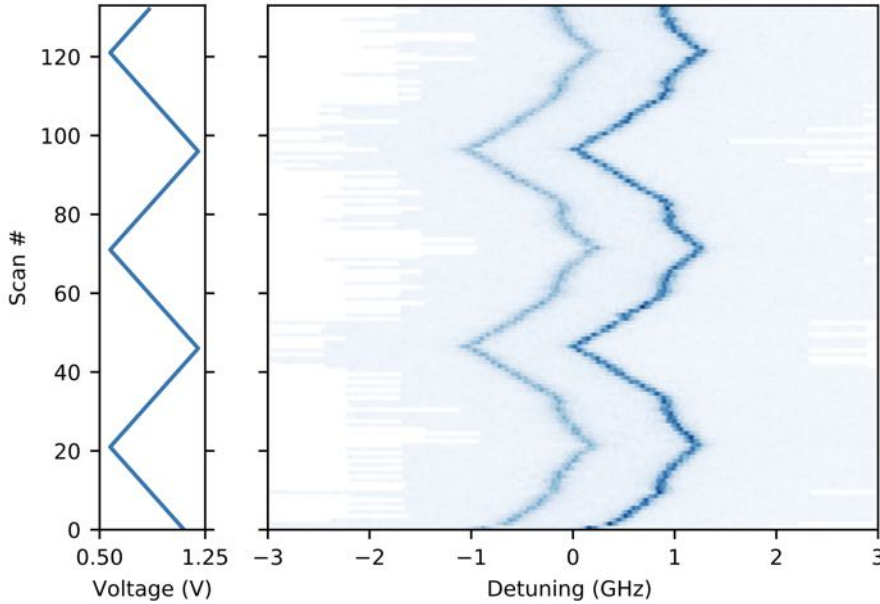


Figure 4.5: **Confirming the non-hysteretic nature of the DC Stark shift near 0 V bias.** As the bias on the electrodes is swept linearly from 0.5 V to 1.25 V and back, it can be seen that the nonlinear behavior is present when scanning in both directions, and thus is not caused by hysteresis. The detuning is given relative to 326.905 THz.

dots[124]. Applying sinusoidal modulation  $\Delta(t)$  for a range of frequencies and amplitudes, we observe that the  $V_{Si}$  spectrum matches the prediction of the scattering matrix theory [114], as shown in Figures 4.7 and 4.6.

Figure 4.8 shows the strongest modulation we could apply at  $\Omega/2\pi = 10$  GHz. The 16 GHz amplitude corresponds to a maximum optical transition slew rate of  $1 \text{ GHz ps}^{-1}$ . At this slew rate, the  $V_{Si}$  transition traverses its 30 MHz transform-limited linewidth  $1.8 \times 10^5$  times within the optical lifetime of 5.5 ns. Even under such rapid modulation, the optical transitions remain as narrow as in the unmodulated  $V_{Si}$ , and only three times broader than the transform-limited linewidth.

### 4.3.1 Spectral stability under AC drive

For most potential applications of fast Stark modulation of quantum emitters, it is essential that modulation does not induce additional spectral diffusion. We investigate the effect of spectral diffusion on the  $h-V_{Si}$  by collecting the PLE spectra of the same emitter with and

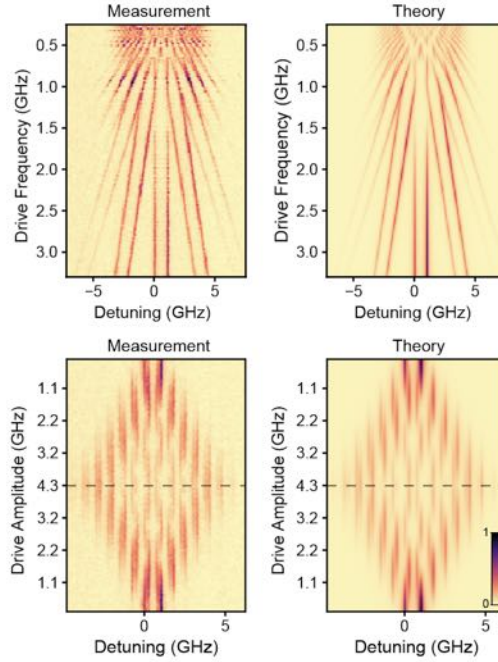


Figure 4.6: **Floquet eigenstates of the  $h\text{-}V_{Si}$  under sinusoidal drive.** Spectral signatures of Floquet states in the  $k\text{-}V_{Si}$  for  $\Delta(t) = A \sin(\Omega t)$  harmonic drive, for swept  $\Omega$  under a fixed amplitude of  $A = 3$  GHz (upper), and swept  $A$  with fixed  $\Omega/2\pi = 750$  MHz (lower). Color corresponds to the normalized photon counts emitted into the phonon sideband. Color corresponds to the normalized photon counts from the PLE.

without modulation for a duration of 5 hours each, as shown in Fig. 4.9. The inhomogeneous linewidth of the modulated emitter is nearly identical to that of the unmodulated emitter (105 MHz compared with 102 MHz). We observe that the single modulated emitter linewidth is broader than that of the unmodulated emitter (due to heating effects as experimentally and theoretically described elsewhere[190]). Our data suggests that other than thermal load effects (which can be addressed with improved electrodes design), there are no adverse effects of microwave modulation on the emitter stability.

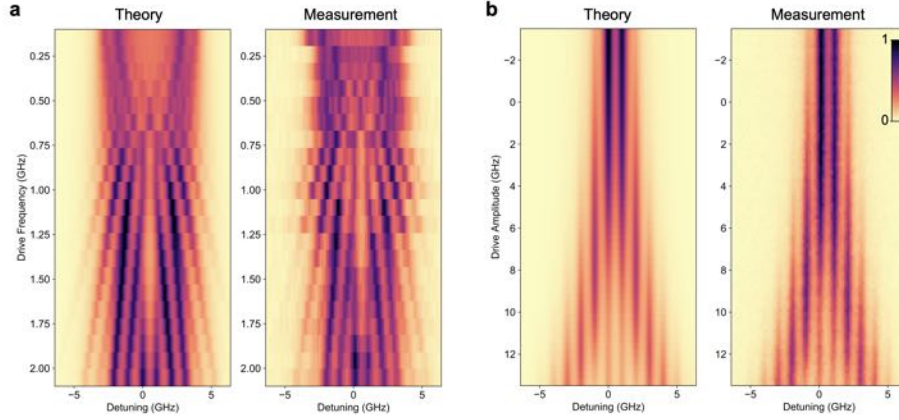


Figure 4.7: **Floquet eigenstates of the  $h$ - $V_{Si}$  under sinusoidal drive.** **a** Spectral signatures of Floquet states in the  $h$ - $V_{Si}$  for  $\Delta(t) = A \sin(\Omega t)$  harmonic drive, for swept  $\Omega$  under a fixed amplitude of  $A = 3$  GHz. **b** Spectral signatures of Floquet states with logarithmically swept microwave drive power with fixed  $\Omega/2\pi = 1$  GHz. Color corresponds to the normalized photon counts from the PLE.

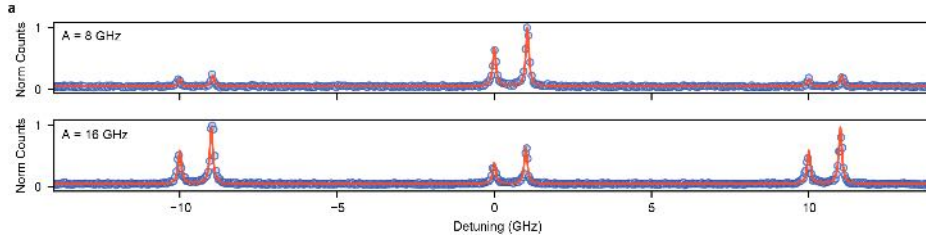


Figure 4.8: **Large amplitude drive of  $k$ - $V_{Si}$**  a PLE spectra of a single  $k$ - $V_{Si}$  driven at a frequency of 10 GHz and amplitudes of 8 and 16 GHz.

#### 4.4 Two-photon scattering from a modulated two-level system

We then study the two-photon scattering properties of the  $V_{Si}$ . As expected for a single-photon emitter, we observe antibunching for all modulation frequencies (Fig. 3c). Additionally, we observe two independent effects: 1) the oscillations in  $g^{(2)}(\tau)$  due to the emitter modulation, present for all  $\tau$ ; and 2) a modulation-independent signature of interference between the four ground states in the ground manifold, decaying exponentially with  $\tau$  due to the spin mixing via the intersystem crossing. A detailed analysis of this interference effect,

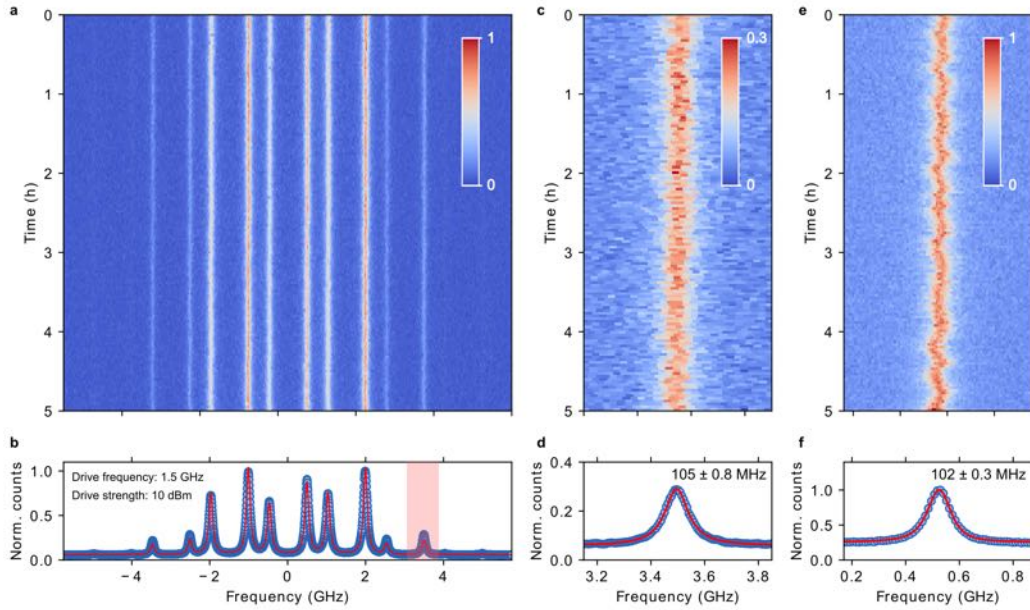


Figure 4.9: **Spectral diffusion under fast modulation.** **a** Continuous PLE measurement over 5 hours of  $h$ - $V_{SI}$  under microwave drive of frequency 1.5 GHz and power 10 dBm. **b** Time averaged spectrum. A minor deviation from the theoretical model is seen due to power broadening, present only for the stronger sidebands due to the comparatively stronger coupling to the laser field. **c** A close-up of panel (a) around the Floquet sideband for the A2 transition, identified with a red stripe in panel (b). **d** Lorentzian fit to the time-averaged spectrum of the transition reveals a linewidth of  $105 \pm 0.8$  MHz. **e** Continuous PLE measurement over 5 hours of the A2 transition of the same emitter but without modulation. **f** Lorentzian fit to the time-averaged spectrum of the transition shows a similar inhomogenous linewidth of  $102 \pm 0.3$  MHz. Frequency is given relative to 347.920 THz

specific to the  $V_{SI}$ , is presented below. Universal to all two-level systems, however, is the modulation-induced oscillations in  $g^{(2)}(\tau)$  that persist for all time delays. Figure 4.10 shows the measured  $g^{(2)}(\tau)$  for a single emitter for modulation frequencies of 15 MHz, 150 MHz, and 1.5 GHz, which probe the slow, intermediate, and fast regimes, respectively. In the slow regime, the shape of  $g^{(2)}(\tau)$  is strongly modified by the Stark modulation. As the modulation frequency is increased, the  $g^{(2)}(\tau)$  becomes practically indistinguishable from that of the unmodulated emitter, in agreement with the scattering-matrix theory [114].

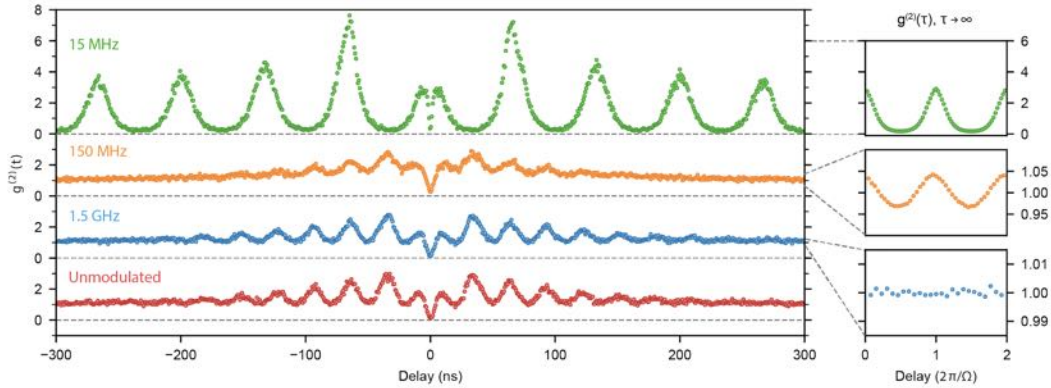


Figure 4.10: **Two-photon scattering off a single Stark-modulated  $V_{Si}$ .** Measurement of the second-order photon correlation —  $g^{(2)}(\tau)$  — under weak coherent excitation in the slow (15 MHz), intermediate (150 MHz) and fast (1.5 GHz) modulation regimes. The modulation-independent oscillations at short time delays originate from the interference of the multiple states in the ground manifold, as discussed in the Supplementary Information. In the limit of long time delay,  $g^{(2)}(\tau)$  of a modulated emitter becomes periodic. To resolve the fine oscillatory features, we average the  $g^{(2)}(\tau)$  data over many microwave periods (up to  $\tau = 200\mu\text{s}$ ), shown in the right panel.

## 4.5 Signature of ground state interference in $g^{(2)}(\tau)$

Figure 4.11 shows the effect on the optical level structure of the defect of the two magnetic field configurations studied in this work. For all experiments other than the  $g^{(2)}(\tau)$  measurements, the axial  $B$  field configuration is used (shown in Fig. 4.11a). For  $g^{(2)}(\tau)$ , however, this configuration cannot be used, as the intersystem crossing channel would depopulate the resonantly pumped optical transition and cause the emitter to go into a dark state. While an rf-magnetic field can be used to induce spin mixing in the ground state, such an approach would introduce a time-dependent term in the Hamiltonian in addition to the studied Stark shift modulation; This would potentially compromise the integrity of the experiment, which aims to isolate the effect of Stark modulation on the two-photon scattering properties. As such, a low, off-axis B-field is applied to allow all states in the ground manifold to couple to the  $\pm 3/2$  excited state subspace.

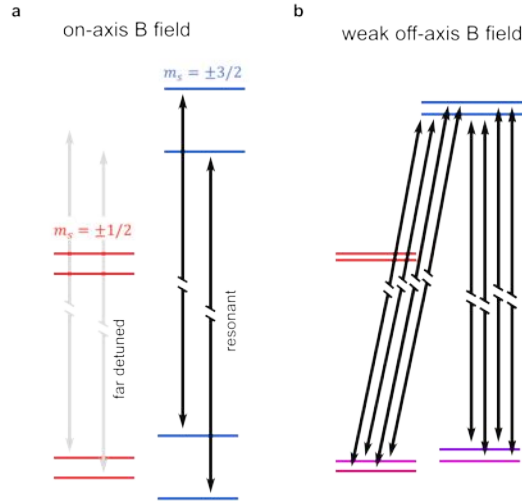


Figure 4.11: **Radiative level structure of the  $V_{Si}$  in different magnetic field configurations.** **a** In a magnetic field aligned with the symmetry axis (*i.e.*  $B_x = 0$ ), the optical transitions are spin-conserving. When resonantly addressing the  $\pm 3/2$  transitions, the  $\pm 1/2$  transitions are far detuned and are not excited. **b** When a low off-axis magnetic field is applied, the ground state spins are hybridized. The excited  $\pm 3/2$  states, however, remain unhybridized due to the much larger excited state ZFS. The non-uniform hybridization is indicated in purple for illustrative purposes. The resulting optical level structure comprises total of 8 optical transitions varying only slightly (order of 10 MHz) in frequency. Crucially, unlike in the axial field case shown in (a), ground states are interacting via spin-non-conserving optical transitions.

#### 4.5.1 Observation of interference of multiple ground states via $g^{(2)}$ .

Using our full extended 12-dimensional Hamiltonian, and the quantum regression theorem [189] we numerically evaluate  $g^{(2)}(\tau)$  and fit it to the experimental data using three unknown  $V_{Si}$  rates (radiative branching ratio, metastable state lifetime, and doublet mixing rate) and well three external parameters (the laser drive strength and the axial and transverse magnetic field strengths). The numerical fit overlaid with experimental data is shown in the top dataset in Fig. 4.12. The branching ratio, metastable lifetime, and doublet mixing are fit to be 0.75, 690 ns, and 5.8 ns, respectively.

We then proceed to change the laser drive power and magnetic field strength, and observe a change in the ground state interference pattern. At higher laser power, we observe a drop in the coherence at longer timescales: This is predicted by the model, as it causes a faster rate of population transfer to the metastable state, where incoherent phonon interactions

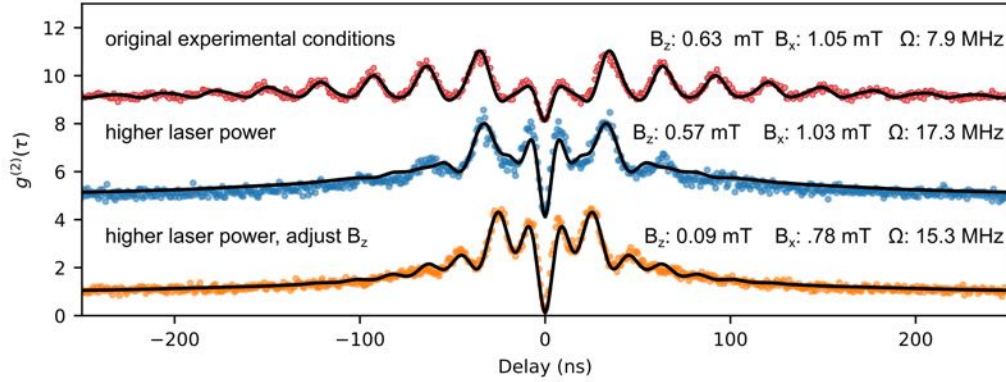


Figure 4.12: **Signatures of ground states interference in  $g^{(2)}$ .** Top dataset is used to extract the three unknown rates of the  $V_{Si}$  described in the text. Then, a higher laser power is applied, and a fit to the model is obtained using the external parameters  $B_z$ ,  $B_x$ ,  $\Omega$ , whose resulting values are shown in the second dataset. Then, with laser power held at the higher level, axial magnetic field was adjusted, and the measurement was repeated (bottom dataset)

destroy the spin coherence. Then, keeping the same laser power we adjust the external magnet to decrease  $B_z$ . As expected, we observe a change in the period of oscillations, which arises from the fine splitting between the ground states. Our numerical model (fit with the three aforementioned “external” parameters) agrees well with the experimental data. For a targeted study of ground state interference in  $g^{(2)}(\tau)$ , integration of rf-B-field delivery to the sample would enable independent verification of the ground state splitting via optically-detected magnetic resonance, and thus permit a fitting with fewer free parameters.

## 4.6 All-optical orbital control of the $V_{Si}$ under AC modulation

We proceed to investigate the interaction of a modulated  $V_{Si}$  with short optical pulses. Using a resonant pulsed laser, we demonstrate fast control of the unmodulated  $V_{Si}$  orbital state (Fig. 4.13a). The high density of  $V_{Si}$  in the sample induces a background fluorescence that limits the signal contrast. As the pulse bandwidth (3 ps) far exceeds the  $V_{Si}$  modulation amplitude, modulation-induced orbital dynamics cannot be resolved with a single pulse. In

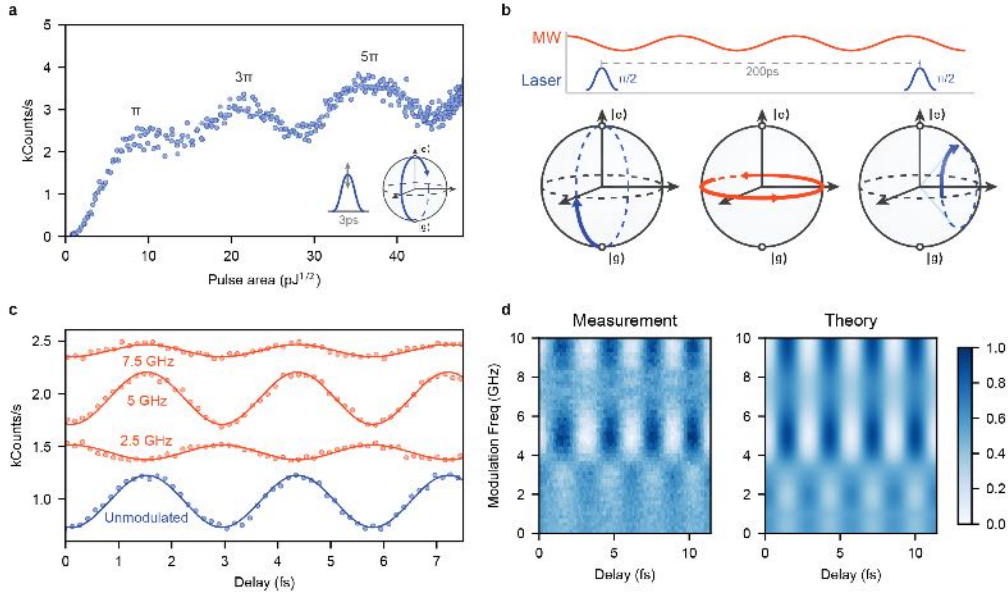


Figure 4.13: **Stark-modulated  $V_{Si}$  interacting with short optical pulses.** **a.** Optical Rabi oscillations of a single unmodulated  $V_{Si}$  excited by a 3 ps laser pulse. **b.** To observe the effects of fast Stark modulation on the orbital state, we measure Ramsey interference by driving the  $V_{Si}$  with two identical  $\pi/2$  resonant pulses separated by a course delay of 200 ps. The Ramsey interference contrast will strongly depend on the modulation period relative to the interpulse delay. **c.** Observed Ramsey interference for various modulation frequencies, as well as for the unmodulated emitter. The data series are offset vertically for clarity. When the interpulse delay is an integer multiple of the modulation period, the observed interference is identical to that of the unmodulated  $V_{Si}$ . **d.** Ramsey interference for modulation frequency swept from DC to 10 GHz. As predicted theoretically, full interference contrast is recovered at 5 and 10 GHz.

order to observe signatures of Stark modulation in the orbital trajectories of the  $V_{Si}$ , we perform a Ramsey interference experiment, where the  $V_{Si}$  is manipulated by a pair of 3 ps optical  $\pi/2$  pulses separated by 200 ps (Fig. 4.13b). We observe a strong dependence of the Ramsey interference amplitude on the modulation frequency (Fig.4.13c). This effect is a consequence of the time-dependent Larmor precession experienced by the modulated  $V_{Si}$  on the equator of the Bloch sphere. When the pulse delay is not a multiple of the modulation period, the accumulated interpulse precession depends on the phase of the microwave signal relative to the arrival of the first pulse. As we show below, the time-averaged Ramsey interference pattern is described by  $1/2 + 1/2 \cos(\omega t_{delay}) J_0 \left( 2 \frac{A}{\Omega} \sin \left( \frac{\Omega t_{delay}}{2} \right) \right)$ , where  $t_{delay}$  is the time delay between the two  $\pi/2$  pulses. We measure the Ramsey interference across

different modulation frequencies and observe the recovery of the full Ramsey contrast at 5 and 10 GHz, in excellent agreement with the theoretical prediction (Fig. 4.13d).

For an unmodulated TLS excited with two  $\pi/2$  pulses delayed by a time  $t_{delay}$  where  $t_{delay} \ll 1/\gamma$ , the Ramsey interference pattern is given by

$$I_R(t_{delay}) = \frac{1}{2} + \frac{1}{2} \cdot \cos(\omega_0 \cdot t_{delay}). \quad (4.1)$$

A sinusoidally modulated TLS experiences an additional phase due to its modulation,

$$A \int_0^{t_{delay}} \cos(\Omega t + \phi) dt = \frac{A}{\Omega} [\sin(\Omega t_{delay} + \phi) - \sin(\phi)], \quad (4.2)$$

where  $\phi$  is the microwave phase relative to the Ramsey pulses.

For modulation frequencies that are not multiples of  $1/t_{delay}$ , the time-averaged Ramsey contrast due to this phase is

$$I_R(t_{delay}, A, \Omega) = \frac{1}{2} + \frac{1}{2} \cdot \frac{1}{2\pi} \int_0^{2\pi} \cos\left(\omega_0 \cdot t_{delay} + \frac{A}{\Omega} [\sin(\Omega t_{delay} + \phi) - \sin(\phi)]\right) d\phi, \quad (4.3)$$

which can be simplified to

$$I_R(t_{delay}, A, \Omega) = \frac{1}{2} + \frac{1}{2} \cdot \cos(\omega_0 \cdot t_{delay}) \cdot J_0\left(\frac{2A}{\Omega} \sin\left(\frac{\Omega \cdot t_{delay}}{2}\right)\right). \quad (4.4)$$

### 4.6.1 Experimental details

Figure 4.2 shows the experimental setup used to investigate Ramsey interference. Not pictured in the diagram is an additional tunable band pass filter (Semrock) placed before the single photon detector, which is used to increase the rejection ratio of the resonant laser; as well as a permanent magnet mounted to produce approximately 20mT field along the symmetry axis of the defect, in order to polarize the ground state manifold. Thermal and acoustic isolation of the experimental setup use to produce the pulse sequence enables high stability of the fine interpulse delay, with drift rates of approximately 1 fs per hour. The data presented is corrected for this residual drift. The 6 MHz repetition rate pulse sequence is produced with a delay generator (Stanford Research Systems, DG645), triggered by the

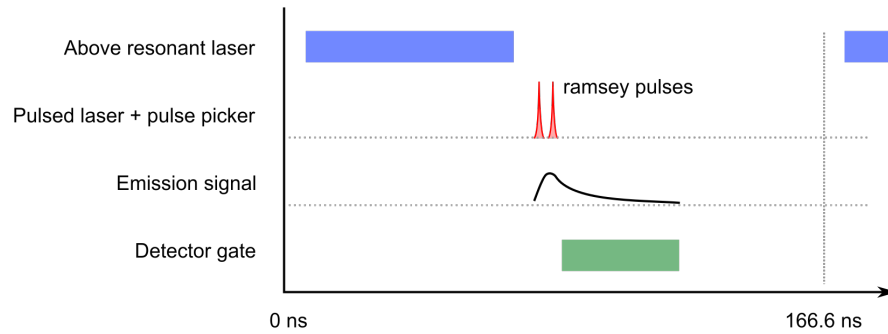


Figure 4.14: **Ramsey pulse sequence.** First, an above resonant pulse initializes the emitter into an equal mixture ground state. A pair of 3 ps pulses (x-axis not to scale) manipulate the emitter orbital state. The single photon detector is gated to only detect the transient signal from the  $V_{Si}$  (optical lifetime 6 ns).

intrinsic laser repetition rate (80 MHz). The pulse sequence is shown in Fig. 4.14.

## Chapter 5

# Conclusions and outlook

In this dissertation, we have addressed the lack of high quality Silicon Carbide on Insulator (SiCOI) material, which has been a roadblock for utilizing SiC both in classical photonics and for scalable quantum architectures. We developed high quality factor photonic circuits for efficient nonlinear photonics, and integrated single color centers into high  $Q/V$  photonic crystal cavities. Then, we fabricate devices in high quality homoepitaxially-grown SiC, observe that the  $V_{\text{Si}}$  remain spectrally stable inside nanostructures, which enables us to show photon interference between two cavity-integrated emitters, constituting a key step towards SiC quantum networks based on remote color centers. Finally, we explore the electrical control of the  $V_{\text{Si}}$  via the Stark effect, both under DC and AC electrical drive, which will be a key technique for overcoming the inhomogeneity of solid state qubits in photonic circuits. In this concluding chapter, we discuss the outlook for quantum photonic networks based on solid state qubits and to provide context for the results presented in the dissertation.

### 5.1 Optimizing the single quantum node

#### Emitter-cavity coupling

The density of states of a defect's electromagnetic environment must be modified in order to enhance and direct its photon emission, suggesting a nanophotonic cavity coupled

to an optically-active spin qubit as the basic building block of a defect-based integrated quantum photonic device. Despite remarkable progress in the development of the cavity-defect node, there remains a large performance gap between integrated quantum photonics devices and their classical photonics counterparts. To date, the state-of-the-art photonic crystal cavities in silicon [7] and whispering gallery resonators in silica [96] have Q factors of  $10^7$  and  $10^9$  ( $10^8$  for a fully-integrated device [212]), respectively. In contrast, photonic devices integrated with spin defects have so far demonstrated Q factors in the  $10^3 - 10^4$  range. It is not surprising that spin-defect photonics are orders of magnitude behind, since the quantum material platforms (i.e., diamond, YSO, YVO, YAG, and SiC) are relatively new to the photonics scene. From this perspective, SiC-on-insulator is uniquely suited for bridging the classical-quantum photonics gap. SiCOI is already in the top three platforms for demonstrating high  $Q/V$  photonic resonators, after silicon on insulator [7] and lithium niobate on insulator [99]. The high refractive index of SiC ( $n \approx 2.6$ ) allows for the fabrication of resonators based on 2D-photonic crystal cavities, the class of nanophotonic devices with the highest  $Q/V$  ratio to-date [7]. The impact of bridging the classical-quantum photonics gap will be an orders-of-magnitude improvement in readout fidelity and entanglement generation rates over current state-of-the-art spin-qubit photonics demonstrations. Furthermore, it will unlock new regimes of spin-qubit operation, including generation of transform-limited (and thus indistinguishable) photons from rare earth ions [84] and strong coupling of a color center to a cavity [17]. In SiC, these advances could likely be implemented with defects such as the  $\text{Cr}^{4+}$  ion, the divacancy, and the silicon vacancy.

What  $Q/V$  is sufficient, then? Naturally, the answer will depend on the defect used and the application. For the  $V_{\text{Si}}$  color center studied in this work, a modest Purcell enhancement of 100 (about 3 times improvement over the whispering gallery mode resonator demonstration in this thesis (Chapter 3)) would be sufficient to achieve 90% fidelity single shot readout with total detection efficiency of 10%, and cooperativity  $C$  in the range 5-10 for nearly transform-limited emitters, enabling nearly deterministic state readout and emitter-photon interactions. More broadly, beyond the  $V_{\text{Si}}$ , a defect with a lower branching ratio into the enhanced transition (for example, due to a small DWF or low quantum efficiency) will require greater  $Q/V$  to achieve the same Purcell enhancement. From the

photonics perspective, the emitter-cavity node is sufficiently optimized once the fraction of emitter excitations that do not result in a photon emitted into the cavity becomes negligible compared to other system losses, *and* the spin state readout fidelity exceeds the fidelity of other single-register qubit operations. For readout, the presence of a cycling transition would relax the  $Q/V$  requirements [150, 17]. In selecting a promising quantum emitter, the brightness of a defect plays a role: High brightness can be an indicator of high quantum efficiency and the presence of cycling transitions. Low brightness, however, does not necessarily mean the contrary, since the presence of a long-lived metastable state can result in low count rates even if the non-radiative decay rate into the metastable states is slow. Thus, in contrast with single photon-source applications, the defect brightness is not the key metric in spin-based quantum technologies.

### Mitigating emitter degradation in nanostructures

Another challenge for defect-based quantum photonics is mitigating the degradation of optical properties of defects in nanostructures. Often, defects with narrow, stable transitions in bulk material degrade severely when a material interface is nearby. The common understanding is that the linewidth degradation is caused by spectral diffusion (i.e., rapid temporal fluctuations in the defect's optical transitions due to fluctuating charges on the nearby surfaces). So far, the greatest success in nanophotonic integration has been had with centrosymmetric defects in diamond such as the silicon vacancy [117, 17, 196], the germanium vacancy [196], and the tin vacancy [157]. And yet, even these defects which should be maximally insensitive to environmental fluctuations display spectral diffusion that by several times exceeds the transform-limited linewidth, likely as a result of strain introduced during growth and fabrication, which lifts the symmetry of these defects and renders them sensitive to electric field to first order [117, 196, 157]. The problem of spectral stability must be solved before the spin-defect quantum photonics technology becomes scalable.

Unlike many intrinsic properties of defects over which the experimentalist has no control, spectral diffusion in nanostructures is an extrinsic property and is amenable to systematic material science engineering. Surface passivation, either chemical or plasma-assisted, is one technique that has been successfully used to increase the photon or phonon lifetime

in nanoresonators [116, 94], but to our knowledge has not yet been explored for defect stabilization. A comprehensive study that seeks to understand rather than simply eliminate spectral diffusion is needed to resolve this problem globally. For example, a comparison of the spectral diffusion of different defect types in the same environment can help elucidate the degradation mechanisms.

The approach toward understanding spectral diffusion and resolving it will likely be specific to each quantum material platform. In the case of SiC, surfaces may potentially be passivated with a graphene layer, which can be readily grown on hexagonal SiC [127]. Although the strong optical absorption of graphene renders this an impractical solution when combined with photonics, it would constitute a valuable proof-of-concept demonstration of passivation-enabled compensation of spectral diffusion. An entirely different method to achieve near-surface emitter stabilization in SiC may take advantage of charge depletion using advanced doping epitaxy available in SiC [3]; implemented successfully in bulk material, the charge depletion technique has yet to be investigated in nanostructures. We note here that charge depletion can be directly integrated with existing nanophotonic architectures, as has been done in other platforms [48]. Although the high temperature required for dopant activation in SiC [151] would necessitate definition of diode structure prior to the fabrication of the SiCOI material stack [110], it is a technologically straightforward process. Another active approach to mitigating the effects of spectral diffusion may be via optimized optical excitation of the emitter, either via time-dependent drive [62] analogous to radiofrequency modulation demonstrations to extend defect spin coherence [18], or via optimized steady-state illumination [187]. Fortunately, the challenge of stabilization of defects in nanostructures is as formidable as the possible strategies for overcoming it are numerous.

### **Comparison of SiC and diamond quantum photonics**

The key color center quantum photonics demonstrations (such as single-shot readout of spin [153, 183], cavity integration of emitters with narrow optical transitions [24, 17, 117], cavity-mediated spin-spin interactions [52], and nuclear spin quantum register [22]) have so far been in the diamond platform, specifically with the NV and the Silicon Vacancy color centers. Both of these color centers possess at least one optical transition that does not

suffer from non-radiative spin-flip processes. The cyclicity of such a transition was utilized for single-shot readout of spin, even without photonic cavity integration [153, 183]. A similar cycling transition has not yet been definitively demonstrated in a SiC color center, although a potential candidate in the  $kh$  divacancy has been identified [126]. However, a cycling transition is not required for single-shot readout if cyclicity can be enhanced with a photonic cavity via the Purcell effect [150]. So far, only centrosymmetric color centers in diamond have been integrated into nanophotonic structures while retaining narrow linewidths [117, 196, 157]. Although inversion symmetry is not in principle a prerequisite for defect insensitivity to electric fields [190], a non-centrosymmetric defect that has a strongly suppressed first order DC Stark shift is yet to be identified. Since crystals without inversion symmetry such as SiC do not host inversion-symmetric defects, it is important to develop techniques to work with non-centrosymmetric defects in nanostructures.

With regard to photonic devices, state-of-the-art microring resonators in SiC and diamond are currently comparable [67, 69], whereas the photonic crystal nanocavities in SiC are superior due to the wider range of device designs accessible in the thin film platform [23, 174]. There are some key differences between diamond and SiC with regard to the intrinsic material properties: The larger bandgap of diamond results in a wider transparency window into the ultraviolet range. Although the SiC bandgap is narrower, it strikes a balance between optical transparency (which spans the visible frequencies) and ease of doping, enabling semiconductor structures such as  $p$ - $i$ - $n$  junctions. The SiC  $\chi^{(3)}$  nonlinearity is an order of magnitude stronger than that of diamond, lowering the power requirement for generating optical parametric oscillation and optical frequency combs [67, 69]. SiC also possesses a strong  $\chi^{(2)}$  nonlinearity of 12 pm/V [162], which is absent in diamond due to the inversion symmetry of its lattice.

## 5.2 Scaling-up quantum photonic processors

When designing a nanophotonic defect-based quantum node, it is crucial to look ahead toward multi-node scalability. This introduces two additional single-node system requirements. First, since the nodes must be spectrally identical during operation, the single node must be spectrally tunable to overcome inherent variations in resonator frequencies and the

inhomogeneous broadening of defects. Second, the node must have an efficient waveguide interface, in order to transfer the emitted photons into the inter-node link with very high efficiency. The exact efficiency requirements will depend strongly on the application. Quantum communication and simulation will likely place a less stringent requirement than fault tolerant quantum computation, where proposals require no more than 10% cumulative loss at all stages of the circuit [139, 138].

The spectral tuning of cavities and color centers has seen excellent progress in a variety of platforms. For cavity tuning, the primary technique has been cryogenic gas condensation [52]: a heated gas tube delivers argon or xenon gas to the sample which then condenses on the cold sample surface, red-shifting the cavity frequency. Since condensed gas can be selectively and gradually removed via heating by a milliwatt laser, one can tune individual cavities onto resonance by applying the appropriate laser pulse. Numerous other techniques have also been employed, including atomic layer deposition [213], laser-assisted oxidation [86], and index-shifting materials [61]. In all, cavity tuning is amenable to further optimization and numerous routes to multi-node scalability exist. We note that although in principle the electrooptic effect allows fast modulation of cavity resonance, the Stark effect in emitters is typically much stronger and thus if rapid modulation is desired, it will likely be advantageous to modulate the emitter with respect to the cavity rather than vice versa. Defect tuning has been demonstrated using both Stark shift [3, 110] and strain [122], with several demonstrations of the tuning range far exceeding the inhomogeneous broadening. Fast, high amplitude spectral modulation of quantum emitters has been shown [126, 114]. One caveat, however, is that current tuning demonstrations are limited to compensating one degree of freedom, whereas spectral inhomogeneity in defects is higher-dimensional in nature (vector for electric field and tensor for strain). Thus, for most defects (an exception are defects with degeneracy broken by spin-spin interactions only, like the  $V_{Si}$  [178]), a single tuning degree of freedom is only sufficient to make one optical transition degenerate [122]. Thus, if a protocol makes use of multiple optical transitions of a single defect, each additional transition must be controlled with an independent tunable laser, which is not scalable [117]. Cavity-assisted Raman emission can allow to overcome this limitation [184]. Overall, while engineering challenges are still ahead, there is already a framework for building a

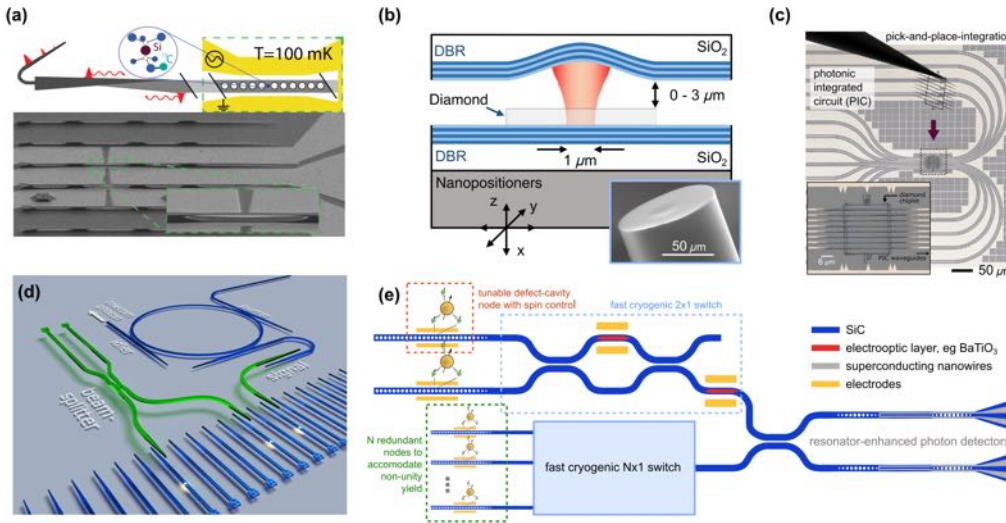


Figure 5.1: **Approaches to scaling-up spin-based quantum photonic technologies** (a) Diamond nanophotonic cavity with a single silicon vacancy defect and an adiabatically-coupled fiber interface. [137] (b) Free-space coupled Fabry-Pérot microcavity enhancing the emission of an NV center in diamond [152]. Inset: the concave mirror can also be fabricated directly on the tip of a fiber [78]. (c) Pick-and-place heterogeneous on-chip integration of diamond microchips containing silicon and germanium vacancy centers on top of aluminum nitride photonic waveguides [196] (image courtesy of Noel Wan). (d) A heterogeneous approach without pick-and-place can be realized by using a secondary layer of photonic interconnects to post-select working quantum nodes [110]. (e) A conceptual diagram demonstrating how the example photonic network shown in Fig. 1.2b could be realized in a fully monolithic platform. In order to account for non-unity fabrication yield,  $N$  redundant nodes are fabricated in the place of one node, and a  $N \times 1$  switch (composed of cascaded  $2 \times 1$  switches) selects one working node. Reproduced from: (a) [137], (b) [152, 78] (d) [110].

fully-tunable quantum node and a clear path toward scalability.

In addition to spectral tuning, an efficient cavity-waveguide interface is the second essential requirement for multi-node devices. To achieve this, the cavity must be designed to be significantly over-coupled to the waveguide (i.e., cavity loss into the waveguide must dominate over other loss channels), implying that ultimately the actual Q factor will be much lower than the highest Q attainable in the platform. Consequently, this places an even greater requirement on the intrinsic cavity  $Q/V$  to maintain the same Purcell enhancement. Furthermore, once the photon has entered the waveguide, great attention must be paid to any losses that the photon may experience as it propagates between nodes.

At this point, it is important to note a distinction between the principles of scalability for classical computers and quantum photonic processors. Classical technologies based on semiconductor transistors progressed through “scaling down”, where the individual node size has been reduced further and further to accommodate greater computing power, until the limiting factor has become the wires rather than the transistors themselves. In contrast, a defect-based quantum photonic computer does not fundamentally enjoy gains from small overall size (as long as the photon emission-enhancing component maximizes large Purcell factor through high  $Q/V$ ). Compared to the resistive losses that limit classical computers, short-distance optical communications (fibers or waveguides) are effectively lossless. The speed of a defect-based quantum computer will not be limited by the internode-link communication rates (photon transit time), but by the (much slower) physics of the quantum node, namely, the spin manipulation and readout of the defect-cavity system. This difference in paradigms is especially relevant in context of the distinct challenge of device yield present in defect-based quantum photonics, since the technological complexity of the single node precludes fabricating quantum nodes with a yield exceeding 99%. This suggests that scaling-up will require a degree of device post-selection and reconfigurability, as is already done on other platforms such as trapped atoms [13]. In light of the above considerations, integration via off-chip fiber interconnects should not a priori be excluded in the near future (before the increasing number of quantum nodes makes it impractical).

In this context, we comment on the current leading approaches toward multi-node scalability:

1. **Integrated nanophotonic devices with a fiber interface.** This approach relies on a nanophotonic cavity for enhancing the light-matter interaction, but routes the photons from the cavity directly into a fiber for off-chip processing (Fig. 5.1a). [24, 117, 17] This approach naturally enables 100% device yield within a quantum network via post-selection: individual devices are characterized and working devices are integrated together via (low loss) fiber interconnects. Because the nanophotonic waveguide and optical fibers are effectively lossless at the relevant length scales, photon loss is incurred exclusively at the fiber-waveguide interface, with demonstrated efficiencies as high as 96% [24]. While this approach is suitable for near-term integration of multiple nodes,

large scale integration is challenging as the fiber coupling interface is bulky, and all photon operations are performed via fiber components.

2. **Fabry-Pérot microcavities.** Recently, photonic resonators based on concave dielectric mirrors have enabled breakthrough demonstrations of cavity-integrated light-matter interactions [134]. In this approach, a concave mirror is fabricated [77] either in bulk silica [152] or, notably, directly on the tip of a fiber [78], and forms a distributed Bragg reflector microcavity with the buried Bragg mirror beneath the active quantum medium, incorporating the defect in-between (Fig. 5.1b). As with fiber-coupled on-chip nanophotonic cavities, unity yield is achieved by post-selection; The fiber-tip scans the surface to isolate a suitable defect, and the cavity resonance is tuned by controlling the fiber height piezoelectrically. Notably, this technique can in principle be applied to any defect that can be integrated into a smooth, thin membrane. [70, 123, 152] The fiber Fabry-Pérot microcavity is in a sense a distillation of the fiber-coupled nanophotonic cavity approach, as the cavity output mode is Gaussian and can efficiently be coupled into single mode fibers. The efficiency is limited by losses in the optical components required for coupling the photons into the single-mode fiber, reflection losses at surfaces, and a slight modal mismatch between the cavity and fiber modes. Recently, a total coupling efficiency of 68% into the fiber mode has been demonstrated [186]. Similarly to the approach above, this approach is more appropriate for near-term scalability due to the direct fiber interface.
3. **Pick-and-place heterogeneous on-chip integration.** This approach aims to address the concern of yield in a fully integrated fashion, by transferring quantum nodes onto an integrated photonic circuit after characterization. Pick-and-place is a particularly promising technique in material platforms not suitable for standard photonics processing: For instance, it has recently enabled large-scale on-chip integration of diamond color centers with aluminum nitride interconnects (Fig. 5.1c) [196]. Although promising for fully chip-scale integration, pick-and-place currently suffers from high experimental losses in the adiabatic transfer of photons from the transferred quantum material to the integrated photonic circuit (transmission of 34% [196]) suggesting that

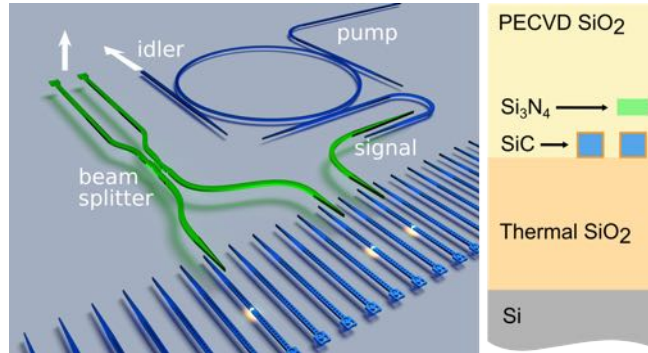


Figure 5.2: **A conceptual diagram showing two applications that can be readily implemented with the 4H-SiCOI architecture.** **a** On the left, the realisation of spin-spin entanglement scheme between two emitter-cavity systems. On the right, emission from a single  $V_{\text{Si}}$  is delivered to a high-Q triply-resonant ring resonator to achieve frequency conversion to the telecommunication frequencies. Although for maximum circuit efficiency it is best to forgo silicon nitride interconnects, this approach may enable short term multi-qubit integration until near-unity single-qubit yield is attained **b** Material stack illustration for the proposed platform.

the transfer efficiency to the inter-node link may be a serious impediment for scalability. Although highly efficient interlayer adiabatic transfer is possible (approaching 99% [169]), it relies on long, well-aligned (200  $\mu\text{m}$ ) tapers that are difficult to achieve using a pick-and-place technique (but are possible with heterogeneous integration of multiple thin-film layers (Fig. 5.1d)). Thus, we see an efficient waveguide interface as the key challenge in developing pick-and-place as a method for multi-node QIP.

### 5.3 Prospects for monolithic frequency conversion and photonic reconfigurability

The compatibility of thin-film SiC with industry-standard nanophotonics processing techniques offers the advantage of foundry-based device fabrication, together with complex optical interconnects and multilayer electrical wiring. This makes the 4H-SiC platform promising both in the long run —when robust fabrication protocols will be crucial for large quantum networks —and in the near future, when low device yields shared by all solid-state quantum photonic platforms may be compensated by device post-selection via photonic circuit reconfigurability. The 4H-SiCOI platform enables, for instance, the integration of quantum nodes

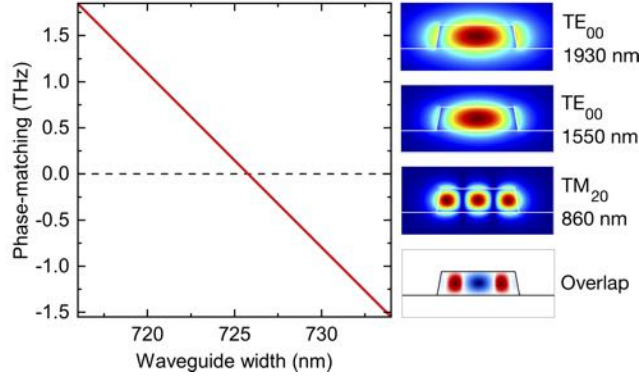


Figure 5.3: **Modal phase-matching for difference-frequency generation.** *Left:* For a waveguide height of 350 nm, sidewall angle of  $\theta = 7^\circ$ , and radius of  $27.5 \mu\text{m}$  with  $\text{SiO}_2$  cladding, the phase-matching condition  $(n_T\omega_T + n_p\omega_p - n_e\omega_e)/2\pi = 0$  THz is achieved for a waveguide width of 725 nm. *Right:* The absolute value of the primary electric field component in the ring cross-section for each mode. The spatial overlap diagram features the real component of  $\sum_{ijk} \chi_{ijk}^{(2)} E_{1i}^* (E_{2j}^* E_{3k} + E_{2k}^* E_{3j})$  prior to integrating over the volume.

post-characterisation via the fabrication of silicon nitride optical interconnects. Critically, the number of qubits in a network is then limited only by the total number of mutually-compatible nodes on-chip. An example of this technique for a two-qubit device is illustrated in Fig. 5.2, where two nanobeams coupled to spectrally-aligned V1' transitions of single  $V_{\text{Si}}$  colour centres are selected, and silicon nitride interconnects are fabricated to realise on-chip spin-spin coupling via Hong-Ou-Mandel photon interference.[47] The versatility of the fabrication platform also enables sensing based on optically-detected spin-mechanical resonance in SiC membranes, with promise towards quantum sensing applications,[146, 205] as well as studies of fundamental material properties.

Quantum frequency conversion of single photons emitted by a color center (such as the  $V_{\text{Si}}$ ) to telecommunication wavelengths is possible by means of nonlinear second-order difference frequency generation,[41] where the emitter ( $\omega_e$ ) and pump ( $\omega_p < \omega_e$ ) photons generate a telecommunication photon ( $\omega_T = \omega_e - \omega_p$ ). A single photon may be converted with high fidelity from  $\omega_e$  to  $\omega_T$ , *i.e.*, the conversion efficiency is quantum-limited, for a critical pump power

$$P_p = \frac{\omega_p}{16|\beta|^2 Q_e Q_p Q_T \Gamma_p}$$

where  $\Gamma_p$  is the ratio of the decay rate into the waveguide over the total decay rate of the

pump mode.[154] Using  $\lambda_p = 1.93$   $\mu\text{m}$ ,  $\lambda_T = 1.55$   $\mu\text{m}$ ,  $\lambda_e = 860$   $\text{nm}$  with  $\Gamma_p = 0.5$ , and  $Q_T = Q_p = 2 \cdot Q_e = 5 \cdot 10^5$ , we calculate a critical pump power of  $P_p = 0.3$   $\text{mW}$ . The coupling factor  $|\beta| = 2.4 \text{ J}^{-1/2}$  is calculated using simulated pump and telecom TE00 mode profiles and a TM20 mode profile (see Fig. 5.3) at the emitter wavelength, where the waveguide dimensions in a 27.5  $\mu\text{m}$ -radius,  $\text{SiO}_2$ -clad microring are designed for phase-matching (*i.e.*, to satisfy the condition  $n_e \omega_e = n_T \omega_T + n_p \omega_p$ , where  $n_k$  is the effective index of the mode with frequency  $\omega_k$ ). This difference frequency process utilizes the same nonlinear term as the SHG process, where the polarization of the  $\omega_e$  mode is chosen to match the orientation of the emitter dipole moment.

## 5.4 Perspective on fully-integrated quantum photonics

Most advanced spin-defect experiments to-date rely on the strategy of coupling emitted photons into an optical fiber as soon as possible (approaches 1 and 2 above). However, for applications other than fiber network communications, a photon in a fiber is not an advantage over a photon in an integrated waveguide: Practical realization of the key components for quantum networks identified in Fig. 1.2 actually plays to the strengths of integrated photonics rather than fiber optics. Integrated photonics have already achieved system complexity beyond what can be practically realized in macroscopic fiber-based devices, integrating hundreds of elements with mean fidelities of linear components exceeding 99.9% [68]. On-chip integration of single-photon detectors has seen remarkable progress in recent years [142, 133, 51], and integration with photonic resonators will likely enable narrowband integrated single photon detection with efficiencies exceeding 99% in the near future. In our view, the chip-integrated approach is the most promising for large-scale quantum systems. This architecture is illustrated in Fig. 5.1(e), using the example photonic network introduced in Fig. 1.2(b).

In this fully-monolithic realization of chip-integrated spin-based quantum technologies, the photon never leaves the chip, never couples into a fiber or passes through lossy bulk active elements, and is not subject to system fluctuations inherent in a large-scale macroscopic system. In fact, the photon never leaves the waveguide into which the quantum node emitted it, because switching, interference, and detection can all be realized in a waveguide

geometry [133, 68]. Compact and efficient on-chip photon detectors can be placed anywhere in the integrated circuit to convert a (fragile) quantum signal into a (robust) classical signal which can be routed off-chip via standard CMOS electronics such as vias and buried electrical layers, aiding in the realization of circuit connectivity. The relative simplicity of the integrated approach is a source of optimism for satisfying the extremely low loss requirements of useful quantum photonic computation.

SiC-on-insulator is a promising candidate to realize a fully-integrated defect-based quantum photonic processor, using high Q/V photonic crystal cavities, fast cryogenic optical modulators, and integrated detectors. In order to overcome the challenge of non-unity yield, each quantum node may consist of  $N$  redundant cavity-coupled spin-defect elements coupled to a bus waveguide. Using this configuration, one can achieve post-selection without any additional cavity-waveguide losses, by tuning all but one working node away from the quantum network operation frequency. If necessary, a similar approach can be employed for post-selection of detectors (which are to be integrated with low-Q resonators or long waveguides to maximize photon absorption probability). Each node is electrically interfaced to tune the defect optical transition and to coherently manipulate the spin. Fast cryogenic modulators and switches based on a directional coupler or resonator drop-filter configuration can be integrated directly into the SiC platform, taking advantage of its electrooptic effect. Cryogenic integration based on this approach has only recently been demonstrated [50]. To increase the bandwidth and decrease the footprint, an additional electro-optically active layer, such as barium titanate ( $\text{BaTiO}_3$ ) [50], can be sputtered and patterned in an adiabatic taper atop the SiC waveguide to minimize scattering loss. Finally, regardless of the optical frequency of operation of the quantum processor, efficient frequency conversion to the telecommunications band using the strong intrinsic second-order nonlinearity of SiC (12 pm/V) [162] would prepare the optically-encoded quantum information for long-distance communication.

In the development of scalable quantum photonic circuits, an emerging technique to device engineering — photonics inverse design [143, 128, 182] — will likely play an important role. The near-unity fidelities achieved with classical photonics design, as mentioned above, are limited to simple photonics building blocks such as a directional coupler. However, for

more complex tasks, inverse design offers a novel approach for performing targeted optimization against multiple metrics, including robustness to fabrication imperfections (thus improving the yield) and fabrication constraints [144]. For example, an classical adiabatic taper between photonic layers [169] is extremely sensitive to misalignment, precluding efficient interlayer coupling in pick-and-place; this limitation is an opportunity to apply inverse design. The powerful functionality of inverse design has been used to demonstrate efficient mode conversion [193] and free-space coupling [161], even under stringent fabrication constraints [46]. The simultaneous inverse design of photonic structures and embedded color centers may enable a fully solid-state implementation of a quantum simulator recently proposed for trapped atoms [64].

## 5.5 Conclusion

In summary, spin-based photonic technologies for quantum computing will likely operate in the on-chip or distributed network architecture (Fig. 1.2) and will require the integration of spin-qubit registers with high quality photonic structures and efficient photon detectors to reduce the total photon loss below the demanding thresholds for quantum computing [138]. While there may be numerous approaches for achieving this goal, we believe that a fully chip-integrated quantum photonic platform holds the most promise, as this approach is most scalable and avoids additional coupling loss from waveguide interconnects. SiC has emerged as a promising platform for realizing this technology with demonstrations of wafer-scale integration of high quality emitters into semiconductor junctions [3], isotopic engineering for nuclear spin registers [10, 20], indistinguishable single photon emission [129, 113], as well as the demonstration quantum-grade SiC-on-Insulator platform for fabrication of photonic devices [110, 113] that was the subject of this dissertation.

# Bibliography

- [1] MH Abobeih, Y Wang, J Randall, SJH Loenen, CE Bradley, M Markham, DJ Twitchen, BM Terhal, and TH Taminiau. Fault-tolerant operation of a logical qubit in a diamond quantum processor. *Nature*, pages 1–1, 2022.
- [2] Shahriar Aghaeimeibodi, Chang-Min Lee, Mustafa Atabey Buyukkaya, Christopher JK Richardson, and Edo Waks. Large stark tuning of InAs/InP quantum dots. *Appl. Phys. Lett.*, 114(7):071105, 2019.
- [3] Christopher P Anderson, Alexandre Bourassa, Kevin C Miao, Gary Wolfowicz, Peter J Mintun, Alexander L Crook, Hiroshi Abe, Jawad Ul Hassan, Nguyen T Son, Takeshi Ohshima, et al. Electrical and optical control of single spins integrated in scalable semiconductor devices. *Science*, 366(6470):1225–1230, 2019.
- [4] Christopher P. Anderson, Elena O. Glen, Cyrus Zeledon, Alexandre Bourassa, Yu Jin, Yizhi Zhu, Christian Vorwerk, Alexander L. Crook, Hiroshi Abe, Jawad Ul-Hassan, Takeshi Ohshima, Nguyen T. Son, Giulia Galli, and David D. Awschalom. Five-second coherence of a single spin with single-shot readout in silicon carbide. *Science Advances*, 8(5):eabm5912, 2022.
- [5] Marta Arcari, Immo Söllner, Alisa Javadi, S Lindskov Hansen, Sahand Mahmoodian, Jin Liu, Henri Thyrestrup, Eun Hye Lee, Jin Dong Song, Søren Stobbe, et al. Near-unity coupling efficiency of a quantum emitter to a photonic crystal waveguide. *Physical review letters*, 113(9):093603, 2014.
- [6] Frank Arute, Kunal Arya, Ryan Babbush, Dave Bacon, Joseph C Bardin, Rami Barends, Rupak Biswas, Sergio Boixo, Fernando GSL Brandao, David A Buell,

- et al. Quantum supremacy using a programmable superconducting processor. *Nature*, 574(7779):505–510, 2019.
- [7] Takashi Asano, Yoshiaki Ochi, Yasushi Takahashi, Katsuhiko Kishimoto, and Susumu Noda. Photonic crystal nanocavity with a q factor exceeding eleven million. *Optics express*, 25(3):1769–1777, 2017.
- [8] Mete Atatüre, Dirk Englund, Nick Vamivakas, Sang-Yun Lee, and Joerg Wrachtrup. Material platforms for spin-based photonic quantum technologies. *Nature Reviews Materials*, 3(5):38–51, 2018.
- [9] David D Awschalom, Ronald Hanson, Jörg Wrachtrup, and Brian B Zhou. Quantum technologies with optically interfaced solid-state spins. *Nature Photonics*, 12(9):516–527, 2018.
- [10] Charles Babin, Rainer Stöhr, Naoya Morioka, Tobias Linkewitz, Timo Steidl, Raphael Wörnle, Di Liu, Erik Hesselmeier, Vadim Vorobyov, Andrej Denisenko, et al. Fabrication and nanophotonic waveguide integration of silicon carbide colour centres with preserved spin-optical coherence. *Nature Materials*, page 67–73, 2022.
- [11] Hunter B Banks, Öney O Soykal, Rachael L Myers-Ward, D Kurt Gaskill, TL Reinicke, and Samuel G Carter. Resonant optical spin initialization and readout of single silicon vacancies in 4 h-si c. *Physical Review Applied*, 11(2):024013, 2019.
- [12] Pavel G Baranov, Anna P Bundakova, Alexandra A Soltamova, Sergei B Orlinskii, Igor V Borovykh, Rob Zondervan, Rogier Verberk, and Jan Schmidt. Silicon vacancy in sic as a promising quantum system for single-defect and single-photon spectroscopy. *Physical Review B*, 83(12):125203, 2011.
- [13] Daniel Barredo, Sylvain De Léséleuc, Vincent Lienhard, Thierry Lahaye, and Antoine Browaeys. An atom-by-atom assembler of defect-free arbitrary two-dimensional atomic arrays. *Science*, 354(6315):1021–1023, 2016.
- [14] LC Bassett, FJ Heremans, CG Yale, BB Buckley, and DD Awschalom. Electrical tuning of single nitrogen-vacancy center optical transitions enhanced by photoinduced fields. *Phys. Rev. Lett.*, 107(26):266403, 2011.

- [15] Hannes Bernien, Lilian Childress, Lucio Robledo, Matthew Markham, Daniel Twitchen, and Ronald Hanson. Two-photon quantum interference from separate nitrogen vacancy centers in diamond. *Physical Review Letters*, 108(4):043604, 2012.
- [16] Hannes Bernien, Sylvain Schwartz, Alexander Keesling, Harry Levine, Ahmed Omran, Hannes Pichler, Soonwon Choi, Alexander S Zibrov, Manuel Endres, Markus Greiner, et al. Probing many-body dynamics on a 51-atom quantum simulator. *Nature*, 551(7682):579–584, 2017.
- [17] Mihir K Bhaskar, Ralf Riedinger, Bartholomeus Machielse, David S Levonian, Christian T Nguyen, Erik N Knall, Hongkun Park, Dirk Englund, Marko Lončar, Denis D Sukachev, et al. Experimental demonstration of memory-enhanced quantum communication. *Nature*, 580(7801):60–64, 2020.
- [18] Dolev Bluvstein, Zhiran Zhang, Claire A McLellan, Nicolas R Williams, and Ania C Bleszynski Jayich. Extending the quantum coherence of a near-surface qubit by coherently driving the paramagnetic surface environment. *Physical Review Letters*, 123(14):146804, 2019.
- [19] Johannes Borregaard, Hannes Pichler, Tim Schröder, Mikhail D Lukin, Peter Lodahl, and Anders S Sørensen. One-way quantum repeater based on near-deterministic photon-emitter interfaces. *Physical Review X*, 10(2):021071, 2020.
- [20] Alexandre Bourassa, Christopher P Anderson, Kevin C Miao, Mykyta Onizhuk, He Ma, Alexander L Crook, Hiroshi Abe, Jawad Ul-Hassan, Takeshi Ohshima, Nguyen T Son, et al. Entanglement and control of single nuclear spins in isotopically engineered silicon carbide. *Nature Materials*, pages 1–7, 2020.
- [21] David O Bracher, Xingyu Zhang, and Evelyn L Hu. Selective purcell enhancement of two closely linked zero-phonon transitions of a silicon carbide color center. *Proceedings of the National Academy of Sciences*, 114(16):4060–4065, 2017.
- [22] CE Bradley, J Randall, MH Aboeih, RC Berrevoets, MJ Degen, MA Bakker, M Markham, DJ Twitchen, and TH Taminiau. A ten-qubit solid-state spin register with quantum memory up to one minute. *Physical Review X*, 9(3):031045, 2019.

- [23] Michael J Burek, Yiwen Chu, Madelaine SZ Liddy, Parth Patel, Jake Rochman, Srujan Meesala, Wooyoung Hong, Qimin Quan, Mikhail D Lukin, and Marko Lončar. High quality-factor optical nanocavities in bulk single-crystal diamond. *Nature communications*, 5(1):1–7, 2014.
- [24] Michael J Burek, Charles Meuwly, Ruffin E Evans, Mihir K Bhaskar, Alp Sipahigil, Srujan Meesala, Bartholomeus Machielse, Denis D Sukachev, Christian T Nguyen, Jose L Pacheco, et al. Fiber-coupled diamond quantum nanophotonic interface. *Physical Review Applied*, 8(2):024026, 2017.
- [25] Donovan Buterakos, Edwin Barnes, and Sophia E Economou. Deterministic generation of all-photonic quantum repeaters from solid-state emitters. *Physical Review X*, 7(4):041023, 2017.
- [26] Lutong Cai, Jingwei Li, Ruixuan Wang, and Qing Li. Octave-spanning microcomb generation in 4h-silicon-carbide-on-insulator photonics platform. *Photonics Research*, 10(4):870–876, 2022.
- [27] Greg Calusine, Alberto Politi, and David D Awschalom. Cavity-enhanced measurements of defect spins in silicon carbide. *Physical Review Applied*, 6(1):014019, 2016.
- [28] Jaime Cardenas, Mengjie Yu, Yoshitomo Okawachi, Carl B Poitras, Ryan KW Lau, Avik Dutt, Alexander L Gaeta, and Michal Lipson. Optical nonlinearities in high-confinement silicon carbide waveguides. *Optics letters*, 40(17):4138–4141, 2015.
- [29] Jaime Cardenas, Mian Zhang, Christopher T Phare, Shreyas Y Shah, Carl B Poitras, Biswajeet Guha, and Michal Lipson. High q sic microresonators. *Optics express*, 21(14):16882–16887, 2013.
- [30] Stefania Castelletto and Alberto Boretti. Silicon carbide color centers for quantum applications. *Journal of Physics: Photonics*, 2(2):022001, 2020.
- [31] Lin Chang, Weiqiang Xie, Haowen Shu, Qi-Fan Yang, Boqiang Shen, Andreas Boes, Jon D Peters, Warren Jin, Chao Xiang, Songtao Liu, et al. Ultra-efficient frequency comb generation in algaas-on-insulator microresonators. *Nature communications*, 11(1):1–8, 2020.

- [32] Yanne K Chembo and Curtis R Menyuk. Spatiotemporal lugiato-lefever formalism for kerr-comb generation in whispering-gallery-mode resonators. *Physical Review A*, 87(5):053852, 2013.
- [33] Huiyao Y Chen, ER MacQuarrie, and Gregory David Fuchs. Orbital state manipulation of a diamond nitrogen-vacancy center using a mechanical resonator. *Phys. Rev. Lett.*, 120(16):167401, 2018.
- [34] Yu-Chen Chen, Patrick S Salter, Matthias Niethammer, Matthias Widmann, Florian Kaiser, Roland Nagy, Naoya Morioka, Charles Babin, Jürgen Erlekampf, Patrick Berwian, et al. Laser writing of scalable single color centers in silicon carbide. *Nano letters*, 19(4):2377–2383, 2019.
- [35] David J Christle, Abram L Falk, Paolo Andrich, Paul V Klimov, Jawad Ul Hassan, Nguyen T Son, Erik Janzén, Takeshi Ohshima, and David D Awschalom. Isolated electron spins in silicon carbide with millisecond coherence times. *Nature materials*, 14(2):160–163, 2015.
- [36] David J Christle, Paul V Klimov, F Charles, Krisztián Szász, Viktor Ivády, Valdas Jokubavicius, Jawad Ul Hassan, Mikael Syväjärvi, William F Koehl, Takeshi Ohshima, et al. Isolated spin qubits in sic with a high-fidelity infrared spin-to-photon interface. *Physical Review X*, 7(2):021046, 2017.
- [37] Kévin G Cognée, Hugo M Doleman, Philippe Lalanne, and AF Koenderink. Cooperative interactions between nano-antennas in a high-Q cavity for unidirectional light sources. *Light: Science & Applications*, 8(1):115, 2019.
- [38] Alexander L Crook, Christopher P Anderson, Kevin C Miao, Alexandre Bourassa, Hope Lee, Sam L Bayliss, David O Bracher, Xingyu Zhang, Hiroshi Abe, Takeshi Ohshima, et al. Purcell enhancement of a single silicon carbide color center with coherent spin control. *Nano Letters*, 2020.
- [39] A Csóré, HJ Von Bardeleben, JL Cantin, and A Gali. Characterization and formation of nv centers in 3 c, 4 h, and 6 h sic: An ab initio study. *Physical Review B*, 96(8):085204, 2017.

- [40] Joel Davidsson, Viktor Ivády, Rickard Armiento, Takeshi Ohshima, NT Son, Adam Gali, and Igor A Abrikosov. Identification of divacancy and silicon vacancy qubits in 6h-sic. *Applied Physics Letters*, 114(11):112107, 2019.
- [41] Kristiaan De Greve, Leo Yu, Peter L. McMahon, Jason S. Pelc, Chandra M. Natarajan, Na Young Kim, Eisuke Abe, Sebastian Maier, Christian Schneider, Martin Kamp, Sven Höfling, Robert H. Hadfield, Alfred Forchel, M. M. Fejer, and Yoshihisa Yamamoto. Quantum-dot spin—photon entanglement via frequency downconversion to telecom wavelength. *Nature*, 491:421–425, 2012.
- [42] Charles F de las Casas, David J Christle, Jawad Ul Hassan, Takeshi Ohshima, Nguyen T Son, and David D Awschalom. Stark tuning and electrical charge state control of single divacancies in silicon carbide. *Appl. Phys. Lett.*, 111(26):262403, 2017.
- [43] L Di Cioccio, F Letertre, Y Le Tiec, AM Papon, C Jausaud, and M Bruel. Silicon carbide on insulator formation by the smart-cut process. *Materials Science and Engineering: B*, 46(1-3):349–356, 1997.
- [44] Berk Diler, Samuel J Whiteley, Christopher P Anderson, Gary Wolfowicz, Marie E Wesson, Edward S Bielejec, F Joseph Heremans, and David D Awschalom. Coherent control and high-fidelity readout of chromium ions in commercial silicon carbide. *npj Quantum Information*, 6(1):1–6, 2020.
- [45] Wenzheng Dong, MW Doherty, and Sophia E Economou. Spin polarization through intersystem crossing in the silicon vacancy of silicon carbide. *Physical Review B*, 99(18):184102, 2019.
- [46] Constantin Dory, Dries Vercauteren, Ki Youl Yang, Neil V Saprà, Alison E Rugar, Shuo Sun, Daniil M Lukin, Alexander Y Piggott, Jingyuan L Zhang, Marina Radulaski, et al. Inverse-designed diamond photonics. *Nature communications*, 10(1):1–7, 2019.
- [47] Sophia E Economou and Pratibha Dev. Spin-photon entanglement interfaces in silicon carbide defect centers. *Nanotechnology*, 27(50):504001, 2016.



- [56] Tianren Fan, Hesam Moradinejad, Xi Wu, Ali A Eftekhar, and Ali Adibi. High-q integrated photonic microresonators on 3c-sic-on-insulator (sicoi) platform. *Optics express*, 26(20):25814–25826, 2018.
- [57] Tianren Fan, Xi Wu, Ali A Eftekhar, Matteo Bosi, Hesam Moradinejad, Eric V Woods, and Ali Adibi. High-quality integrated microdisk resonators in the visible-to-near-infrared wavelength range on a 3c-silicon carbide-on-insulator platform. *Optics Letters*, 45(1):153–156, 2020.
- [58] Tianren Fan, Xi Wu, Sai RM Vangapandu, Amir H Hosseinnia, Ali A Eftekhar, and Ali Adibi. Racetrack microresonator based electro-optic phase shifters on a 3c silicon-carbide-on-insulator platform. *Optics Letters*, 46(9):2135–2138, 2021.
- [59] Andrei Faraon, Paul E. Barclay, Charles Santori, Kai-Mei C. Fu, and Raymond G. Beausoleil. Resonant enhancement of the zero-phonon emission from a colour centre in a diamond cavity. *Nature Photonics*, 5:301–305, 2011.
- [60] Andrei Faraon, Paul E Barclay, Charles Santori, Kai-Mei C Fu, and Raymond G Beausoleil. Resonant enhancement of the zero-phonon emission from a colour centre in a diamond cavity. *Nature Photonics*, 5(5):301–305, 2011.
- [61] Andrei Faraon, Dirk Englund, Douglas Bulla, Barry Luther-Davies, Benjamin J Eggleton, Nick Stoltz, Pierre Petroff, and Jelena Vučković. Local tuning of photonic crystal cavities using chalcogenide glasses. *Applied Physics Letters*, 92(4):043123, 2008.
- [62] HF Fotso, AE Feiguin, DD Awschalom, and VV Dobrovitski. Suppressing spectral diffusion of emitted photons with optical pulses. *Physical Review Letters*, 116(3):033603, 2016.
- [63] F Fuchs, B Stender, M Trupke, D Simin, J Pflaum, V Dyakonov, and GV Astakhov. Engineering near-infrared single-photon emitters with optically active spins in ultra-pure silicon carbide. *Nature communications*, 6(1):1–7, 2015.
- [64] Alejandro González-Tudela, C-L Hung, Darrick E Chang, J Ignacio Cirac, and HJ Kimble. Subwavelength vacuum lattices and atom-atom interactions in two-dimensional photonic crystals. *Nature Photonics*, 9(5):320–325, 2015.

- [65] Joel Q Grim, Allan S Bracker, Maxim Zalalutdinov, Samuel G Carter, Alexander C Kozen, Mijin Kim, Chul Soo Kim, Jerome T Mlack, Michael Yakes, Bumsu Lee, et al. Scalable in operando strain tuning in nanophotonic waveguides enabling three-quantum-dot superradiance. *Nature materials*, 18(9):963–969, 2019.
- [66] Melissa A Guidry, Daniil M Lukin, Ki Youl Yang, Rahul Trivedi, and Jelena Vučković. Quantum optics of soliton microcombs. *Nature Photonics*, 16(1):52–58, 2022.
- [67] Melissa A Guidry, Ki Youl Yang, Daniil M Lukin, Ashot Markosyan, Joshua Yang, Martin M Fejer, and Jelena Vučković. Optical parametric oscillation in silicon carbide nanophotonics. *Optica*, 7:1139, 2020.
- [68] Nicholas C Harris, Gregory R Steinbrecher, Mihika Prabhu, Yoav Lahini, Jacob Mower, Darius Bunandar, Changchen Chen, Franco NC Wong, Tom Baehr-Jones, Michael Hochberg, et al. Quantum transport simulations in a programmable nanophotonic processor. *Nature Photonics*, 11(7):447, 2017.
- [69] BJM Hausmann, I Bulu, V Venkataraman, P Deotare, and Marko Lončar. Diamond nonlinear photonics. *Nature Photonics*, 8(5):369–374, 2014.
- [70] Stefan Häußler, Julia Benedikter, Kerem Bray, Blake Regan, Andreas Dietrich, Jason Twamley, Igor Aharonovich, David Hunger, and Alexander Kubanek. Diamond photonics platform based on silicon vacancy centers in a single-crystal diamond membrane and a fiber cavity. *Physical Review B*, 99(16):165310, 2019.
- [71] Yang He, Jingwei Ling, Mingxiao Li, and Qiang Lin. Perfect soliton crystals on demand. *Laser & Photonics Reviews*, 14(8):1900339, 2020.
- [72] Martijn JR Heck, Jared F Bauters, Michael L Davenport, Daryl T Spencer, and John E Bowers. Ultra-low loss waveguide platform and its integration with silicon photonics. *Laser & Photonics Reviews*, 8(5):667–686, 2014.
- [73] Bas Hensen, Hannes Bernien, Anaïs E Dréau, Andreas Reiserer, Norbert Kalb, Machiel S Blok, Just Ruitenbergh, Raymond FL Vermeulen, Raymond N Schouten, Carlos Abellán, et al. Loophole-free bell inequality violation using electron spins separated by 1.3 kilometres. *Nature*, 526(7575):682–686, 2015.

- [74] Christian Hepp. *Electronic Structure of the Silicon Vacancy Color Center in Diamond*. PhD thesis, Universität des Saarlandes, 2014.
- [75] T. Herr, J. Riemensberg, C. Y. Wang, E. Gavartin, R. Holzwarth, M. L. Gorodetsky, and T. J. Kippenberg. Universal formation dynamics and noise of Kerr-frequency combs in microresonators. *Nature Photonics*, 6:480–487, 2012.
- [76] Peter C Humphreys, Norbert Kalb, Jaco PJ Morits, Raymond N Schouten, Raymond FL Vermeulen, Daniel J Twitchen, Matthew Markham, and Ronald Hanson. Deterministic delivery of remote entanglement on a quantum network. *Nature*, 558(7709):268–273, 2018.
- [77] David Hunger, Christian Deutsch, Russell J Barbour, Richard J Warburton, and Jakob Reichel. Laser micro-fabrication of concave, low-roughness features in silica. *Aip Advances*, 2(1):012119, 2012.
- [78] David Hunger, Tilo Steinmetz, Yves Colombe, Christian Deutsch, Theodor W Hänsch, and Jakob Reichel. A fiber fabry-perot cavity with high finesse. *New Journal of Physics*, 12(6):065038, 2010.
- [79] Viktor Ivády, Paul V Klimov, Kevin C Miao, Abram L Falk, David J Christle, Krisztián Szász, Igor A Abrikosov, David D Awschalom, and Adam Gali. High-fidelity bidirectional nuclear qubit initialization in sic. *Physical review letters*, 117(22):220503, 2016.
- [80] Warren Jin, Qi-Fan Yang, Lin Chang, Boqiang Shen, Heming Wang, Mark A Leal, Lue Wu, Maodong Gao, Avi Feshali, Mario Paniccia, et al. Hertz-linewidth semiconductor lasers using cmos-ready ultra-high-q microresonators. *Nature Photonics*, pages 1–8, 2021.
- [81] Norbert Kalb, Andreas A Reiserer, Peter C Humphreys, Jacob JW Bakermans, Sten J Kamerling, Naomi H Nickerson, Simon C Benjamin, Daniel J Twitchen, Matthew Markham, and Ronald Hanson. Entanglement distillation between solid-state quantum network nodes. *Science*, 356(6341):928–932, 2017.

- [82] C Kasper, D Klenkert, Z Shang, D Simin, A Gottscholl, A Sperlich, H Kraus, C Schneider, S Zhou, M Trupke, et al. Influence of irradiation on defect spin coherence in silicon carbide. *Physical Review Applied*, 13(4):044054, 2020.
- [83] Je-Hyung Kim, Shahriar Aghaeimeibodi, Christopher JK Richardson, Richard P Leavitt, and Edo Waks. Super-radiant emission from quantum dots in a nanophotonic waveguide. *Nano Letters*, 18(8):4734–4740, 2018.
- [84] Jonathan M Kindem, Andrei Ruskuc, John G Bartholomew, Jake Rochman, Yan Qi Huan, and Andrei Faraon. Control and single-shot readout of an ion embedded in a nanophotonic cavity. *Nature*, 580(7802):201–204, 2020.
- [85] TJ Kippenberg, SM Spillane, and KJ Vahala. Kerr-nonlinearity optical parametric oscillation in an ultrahigh-q toroid microcavity. *Physical Review Letters*, 93(8):083904, 2004.
- [86] S Kiravittaya, HS Lee, L Balet, LH Li, M Francardi, A Gerardino, A Fiore, A Rastelli, and OG Schmidt. Tuning optical modes in slab photonic crystal by atomic layer deposition and laser-assisted oxidation. *Journal of Applied Physics*, 109(5):053115, 2011.
- [87] Paul V Klimov, Abram L Falk, David J Christle, Viatcheslav V Dobrovitski, and David D Awschalom. Quantum entanglement at ambient conditions in a macroscopic solid-state spin ensemble. *Science advances*, 1(10):e1501015, 2015.
- [88] PV Klimov, AL Falk, BB Buckley, and DD Awschalom. Electrically driven spin resonance in silicon carbide color centers. *Physical Review Letters*, 112(8):087601, 2014.
- [89] William F Koehl, Bob B Buckley, F Joseph Heremans, Greg Calusine, and David D Awschalom. Room temperature coherent control of defect spin qubits in silicon carbide. *Nature*, 479(7371):84–87, 2011.
- [90] William F Koehl, Berk Diler, Samuel J Whiteley, Alexandre Bourassa, N Tien Son, Erik Janzén, and David D Awschalom. Resonant optical spectroscopy and coherent control of cr 4+ spin ensembles in sic and gan. *Physical Review B*, 95(3):035207, 2017.

- [91] H. Kraus, D. Simin, C. Kasper, Y. Suda, S. Kawabata, W. Kada, T. Honda, Y. Hijikata, T. Ohshima, V. Dyakonov, and G. V. Astakhov. Three-dimensional proton beam writing of optically active coherent vacancy spins in silicon carbide. *Nano Lett.*, 17(5):2865–2870, 2017.
- [92] H Kraus, D Simin, C Kasper, Y Suda, S Kawabata, W Kada, T Honda, Y Hijikata, T Ohshima, V Dyakonov, et al. Three-dimensional proton beam writing of optically active coherent vacancy spins in silicon carbide. *Nano letters*, 17(5):2865–2870, 2017.
- [93] H Kraus, VA Soltamov, D Riedel, S V ath, F Fuchs, A Sperlich, PG Baranov, V Dyakonov, and GV Astakhov. Room-temperature quantum microwave emitters based on spin defects in silicon carbide. *Nature Physics*, 10(2):157–162, 2014.
- [94] Kazuhiro Kuruma, Yasutomo Ota, Masahiro Kakuda, Satoshi Iwamoto, and Yasuhiko Arakawa. Surface-passivated high-q gaas photonic crystal nanocavity with quantum dots. *APL Photonics*, 5(4):046106, 2020.
- [95] Kazuhiro Kuruma, Benjamin Pingault, Cleaven Chia, Dylan Renaud, Patrick Hoffmann, Satoshi Iwamoto, Carsten Ronning, and Marko Lon ar. Coupling of a single tin-vacancy center to a photonic crystal cavity in diamond. *Applied Physics Letters*, 118(23):230601, 2021.
- [96] Hansuek Lee, Tong Chen, Jiang Li, Ki Youl Yang, Seokmin Jeon, Oskar Painter, and Kerry J Vahala. Chemically etched ultrahigh-q wedge-resonator on a silicon chip. *Nature Photonics*, 6(6):369–373, 2012.
- [97] David Levonian, Ralf Riedinger, Bartholomeus Machielse, Erik Knall, Mihir Bhaskar, Can Knaut, Rivka Bekenstein, Hongkun Park, Marko Loncar, and Mikhail Lukin. Optical entanglement of distinguishable quantum emitters. *arXiv preprint arXiv:2108.10928*, 2021.
- [98] Jiang Li, Hansuek Lee, Ki Youl Yang, and Kerry J. Vahala. Sideband spectroscopy and dispersion measurement in microcavities. *Opt. Express*, 20:26337–26344, 2012.
- [99] Mingxiao Li, Hanxiao Liang, Rui Luo, Yang He, Jingwei Ling, and Qiang Lin. Photon-level tuning of photonic nanocavities. *Optica*, 6(7):860–863, 2019.

- [100] Z Li and Richard C Bradt. Thermal expansion of the hexagonal (4 h) polytype of sic. *Journal of Applied Physics*, 60(2):612–614, 1986.
- [101] Di Liu et al. (manuscript in preparation). (*in preparation*), 2021.
- [102] Junqiu Liu, Guanhao Huang, Rui Ning Wang, Jijun He, Arslan S Raja, Tianyi Liu, Nils J Engelsen, and Tobias J Kippenberg. High-yield wafer-scale fabrication of ultralow-loss, dispersion-engineered silicon nitride photonic circuits. *arXiv preprint arXiv:2005.13949*, 2020.
- [103] Junqiu Liu, Arslan S Raja, Maxim Karpov, Bahareh Ghadiani, Martin HP Pfeiffer, Botao Du, Nils J Engelsen, Hairun Guo, Michael Zervas, and Tobias J Kippenberg. Ultralow-power chip-based soliton microcombs for photonic integration. *Optica*, 5(10):1347–1353, 2018.
- [104] Junqiu Liu, Hao Tian, Erwan Lucas, Arslan S Raja, Grigory Lihachev, Rui Ning Wang, Jijun He, Tianyi Liu, Miles H Anderson, Wenle Weng, et al. Monolithic piezoelectric control of soliton microcombs. *Nature*, 583(7816):385–390, 2020.
- [105] Peter Lodahl, Sahand Mahmoodian, Søren Stobbe, Arno Rauschenbeutel, Philipp Schneeweiss, Jürgen Volz, Hannes Pichler, and Peter Zoller. Chiral quantum optics. *Nature*, 541(7638):473–480, 2017.
- [106] Alexander Lohrmann, Timothy James Karle, Vikas Kanayalal Sewani, Arne Laucht, Matteo Bosi, Marco Negri, Stefania Castelletto, Steven Praver, Jeffrey Colin McCallum, and Brett Cameron Johnson. Integration of single-photon emitters into 3C-SiC microdisk resonators. *ACS Photonics*, 4(3):462–468, 2017.
- [107] Xiyuan Lu, Jonathan Y Lee, Philip X-L Feng, and Qiang Lin. High q silicon carbide microdisk resonator. *Applied Physics Letters*, 104(18):181103, 2014.
- [108] Xiyuan Lu, Jonathan Y Lee, Steven Rogers, and Qiang Lin. Optical kerr nonlinearity in a high-q silicon carbide microresonator. *Optics Express*, 22(25):30826–30832, 2014.

- [109] Xiyuan Lu, Gregory Moille, Anshuman Singh, Qing Li, Daron A. Westly, Ashutosh Rao, Su-Peng Yu, Travis C. Briles, Scott B. Papp, and Kartik Srinivasan. Milliwatt-threshold visible–telecom optical parametric oscillation using silicon nanophotonics. *Optica*, 6(12):1535–1541, Dec 2019.
- [110] Daniil M Lukin, Constantin Dory, Melissa A Guidry, Ki Youl Yang, Sattwik Deb Mishra, Rahul Trivedi, Marina Radulaski, Shuo Sun, Dries Vercruyssen, Geun Ho Ahn, et al. 4h-silicon-carbide-on-insulator for integrated quantum and nonlinear photonics. *Nature Photonics*, 14(5):330–334, 2020.
- [111] Daniil M Lukin, Melissa A Guidry, and Jelena Vučković. Integrated quantum photonics with silicon carbide: challenges and prospects. *PRX Quantum*, 1(2):020102, 2020.
- [112] Daniil M Lukin, Melissa A Guidry, and Jelena Vučković. Silicon carbide: From abrasives to quantum photonics. *Optics and Photonics News*, 32(3):34–41, 2021.
- [113] Daniil M Lukin, Melissa A Guidry, Joshua Yang, Misagh Ghezellou, Sattwik Deb Mishra, Hiroshi Abe, Takeshi Ohshima, Jawad Ul-Hassan, and Jelena Vučković. Optical superradiance of a pair of color centers in an integrated silicon-carbide-on-insulator microresonator. *arXiv preprint arXiv:2202.04845*, 2022.
- [114] Daniil M Lukin, Alexander D White, Melissa A Guidry, Rahul Trivedi, Naoya Morioka, Charles Babin, Jawad Ul Hassan, Nguyen Tien Son, Takeshi Ohshima, Praful K Vasireddy, et al. Spectrally reconfigurable quantum emitters enabled by optimized fast modulation. *npj Quantum Info*, 6:80, 2020.
- [115] Rui Luo, Yang He, Hanxiao Liang, Mingxiao Li, Jingwei Ling, and Qiang Lin. Optical parametric generation in a lithium niobate microring with modal phase matching. *Phys. Rev. Appl.*, 11:034026, 2019.
- [116] Gregory S MacCabe, Hengjiang Ren, Jie Luo, Justin D Cohen, Hengyun Zhou, Alp Sipahigil, Mohammad Mirhosseini, and Oskar Painter. Phononic bandgap nano-acoustic cavity with ultralong phonon lifetime. *arXiv preprint arXiv:1901.04129*, 2019.

- [117] Bartholomeus Machielse, Stefan Bogdanovic, Srujan Meesala, Scarlett Gauthier, Michael J Burek, Graham Joe, Michelle Chalupnik, Young-Ik Sohn, Jeffrey Holzgrafe, Ruffin E Evans, et al. Quantum interference of electromechanically stabilized emitters in nanophotonic devices. *Physical Review X*, 9(3):031022, 2019.
- [118] Andrew P Magyar, David Bracher, Jonathan C Lee, Igor Aharonovich, and Evelyn L Hu. High quality sic microdisk resonators fabricated from monolithic epilayer wafers. *Applied Physics Letters*, 104(5):051109, 2014.
- [119] Smarak Maity, Linbo Shao, Stefan Bogdanović, Srujan Meesala, Young-Ik Sohn, Neil Sinclair, Benjamin Pingault, Michelle Chalupnik, Cleaven Chia, Lu Zheng, et al. Coherent acoustic control of a single silicon vacancy spin in diamond. *Nat. Commun.*, 11(1):1–6, 2020.
- [120] AS Markosyan, R Route, MM Fejer, D Patel, and C Menoni. Study of spontaneous and induced absorption in amorphous ta<sub>2</sub>o<sub>5</sub> and sio<sub>2</sub> dielectric thin films. *Journal of Applied Physics*, 113(13):133104, 2013.
- [121] RD Meade, Joshua N Winn, and JD Joannopoulos. Photonic crystals: Molding the flow of light, 1995.
- [122] Srujan Meesala, Young-Ik Sohn, Benjamin Pingault, Linbo Shao, Haig A Atikian, Jeffrey Holzgrafe, Mustafa Gündoğan, Camille Stavrakas, Alp Sipahigil, Cleaven Chia, et al. Strain engineering of the silicon-vacancy center in diamond. *Physical Review B*, 97(20):205444, 2018.
- [123] Benjamin Merkel, Alexander Ulanowski, and Andreas Reiserer. Coherent emission of erbium dopants in a high-q resonator. *arXiv preprint arXiv:2006.14229*, 2020.
- [124] Michael Metcalfe, Stephen M Carr, Andreas Muller, Glenn S Solomon, and John Lawall. Resolved sideband emission of InAs/GaAs quantum dots strained by surface acoustic waves. *Phys. Rev. Lett.*, 105(3):037401, 2010.
- [125] Kevin C Miao, Joseph P Blanton, Christopher P Anderson, Alexandre Bourassa, Alexander L Crook, Gary Wolfowicz, Hiroshi Abe, Takeshi Ohshima, and David D

- Awschalom. Universal coherence protection in a solid-state spin qubit. *Science*, 369:1493–1497, 2020.
- [126] Kevin C Miao, Alexandre Bourassa, Christopher P Anderson, Samuel J Whiteley, Alexander L Crook, Sam L Bayliss, Gary Wolfowicz, Gergő Thiering, Péter Udvarhelyi, Viktor Ivády, et al. Electrically driven optical interferometry with spins in silicon carbide. *Science Advances*, 5(11):eaay0527, 2019.
- [127] Neeraj Mishra, John Boeckl, Nunzio Motta, and Francesca Iacopi. Graphene growth on silicon carbide: A review. *physica status solidi (a)*, 213(9):2277–2289, 2016.
- [128] Sean Molesky, Zin Lin, Alexander Y Piggott, Weiliang Jin, Jelena Vucković, and Alejandro W Rodriguez. Inverse design in nanophotonics. *Nature Photonics*, 12(11):659–670, 2018.
- [129] Naoya Morioka, Charles Babin, Roland Nagy, Izel Gediz, Erik Hesselmeier, Di Liu, Matthew Joliffe, Matthias Niethammer, Durga Dasari, Vadim Vorobyov, et al. Spin-controlled generation of indistinguishable and distinguishable photons from silicon vacancy centres in silicon carbide. *Nature communications*, 11(1):1–8, 2020.
- [130] Sreraman Muralidharan, Linshu Li, Jungsang Kim, Norbert Lütkenhaus, Mikhail D Lukin, and Liang Jiang. Optimal architectures for long distance quantum communication. *Scientific reports*, 6:20463, 2016.
- [131] Roland Nagy, Matthias Niethammer, Matthias Widmann, Yu-Chen Chen, Péter Udvarhelyi, Cristian Bonato, Jawad Ul Hassan, Robin Karhu, Ivan G Ivanov, Nguyen Tien Son, et al. High-fidelity spin and optical control of single silicon-vacancy centres in silicon carbide. *Nature communications*, 10(1):1–8, 2019.
- [132] Roland Nagy, Matthias Widmann, Matthias Niethammer, Durga BR Dasari, Ilja Gerhardt, Öney O Soykal, Marina Radulaski, Takeshi Ohshima, Jelena Vučković, Nguyen Tien Son, et al. Quantum properties of dichroic silicon vacancies in silicon carbide. *Physical Review Applied*, 9(3):034022, 2018.
- [133] Faraz Najafi, Jacob Mower, Nicholas C Harris, Francesco Bellei, Andrew Dane, Catherine Lee, Xiaolong Hu, Prashanta Kharel, Francesco Marsili, Solomon Assefa,

- et al. On-chip detection of non-classical light by scalable integration of single-photon detectors. *Nature communications*, 6(1):1–8, 2015.
- [134] Daniel Najer, Immo Söllner, Pavel Sekatski, Vincent Dolique, Matthias C Löbl, Daniel Riedel, Rüdiger Schott, Sebastian Starosielec, Sascha R Valentin, Andreas D Wieck, et al. A gated quantum dot strongly coupled to an optical microcavity. *Nature*, pages 1–1, 2019.
- [135] Kae Nemoto, Michael Trupke, Simon J Devitt, Ashley M Stephens, Burkhard Scharfenberger, Kathrin Buczak, Tobias Nöbauer, Mark S Everitt, Jörg Schmiedmayer, and William J Munro. Photonic architecture for scalable quantum information processing in diamond. *Physical Review X*, 4(3):031022, 2014.
- [136] P Neumann, R Kolesov, B Naydenov, J Beck, F Rempp, M Steiner, V Jacques, G Balasubramanian, ML Markham, DJ Twitchen, et al. Quantum register based on coupled electron spins in a room-temperature solid. *Nature Physics*, 6(4):249–253, 2010.
- [137] CT Nguyen, DD Sukachev, MK Bhaskar, B Machielse, DS Levonian, EN Knall, P Stroganov, R Riedinger, H Park, M Lončar, et al. Quantum network nodes based on diamond qubits with an efficient nanophotonic interface. *Physical review letters*, 123(18):183602, 2019.
- [138] Naomi H Nickerson, Joseph F Fitzsimons, and Simon C Benjamin. Freely scalable quantum technologies using cells of 5-to-50 qubits with very lossy and noisy photonic links. *Physical Review X*, 4(4):041041, 2014.
- [139] Naomi H Nickerson, Ying Li, and Simon C Benjamin. Topological quantum computing with a very noisy network and local error rates approaching one percent. *Nature communications*, 4(1):1–5, 2013.
- [140] Matthias Niethammer, Matthias Widmann, Torsten Rendler, Naoya Morioka, Yu-Chen Chen, Rainer Stöhr, Jawad Ul Hassan, Shinobu Onoda, Takeshi Ohshima, Sang-Yun Lee, et al. Coherent electrical readout of defect spins in silicon carbide by photoionization at ambient conditions. *Nature Communications*, 10(1):1–8, 2019.

- [141] Bo Peng, Şahin Kaya Özdemir, Matthias Liertzer, Weijian Chen, Johannes Kramer, Huzeyfe Yilmaz, Jan Wiersig, Stefan Rotter, and Lan Yang. Chiral modes and directional lasing at exceptional points. *Proceedings of the National Academy of Sciences*, 113(25):6845–6850, 2016.
- [142] Wolfram HP Pernice, C Schuck, O Minaeva, M Li, GN Goltsman, AV Sergienko, and HX Tang. High-speed and high-efficiency travelling wave single-photon detectors embedded in nanophotonic circuits. *Nature communications*, 3(1):1–10, 2012.
- [143] Alexander Y Piggott, Jesse Lu, Konstantinos G Lagoudakis, Jan Petykiewicz, Thomas M Babinec, and Jelena Vučković. Inverse design and demonstration of a compact and broadband on-chip wavelength demultiplexer. *Nature Photonics*, 9(6):374–377, 2015.
- [144] Alexander Y Piggott, Jan Petykiewicz, Logan Su, and Jelena Vučković. Fabrication-constrained nanophotonic inverse design. *Scientific reports*, 7(1):1–7, 2017.
- [145] Matteo Pompili, Sophie LN Hermans, Simon Baier, Hans KC Beukers, Peter C Humphreys, Raymond N Schouten, Raymond FL Vermeulen, Marijn J Tiggelman, Laura dos Santos Martins, Bas Dirkse, et al. Realization of a multinode quantum network of remote solid-state qubits. *Science*, 372(6539):259–264, 2021.
- [146] A. V. Poshakinskiy and G. V. Astakhov. Optically detected spin-mechanical resonance in silicon carbide membranes. *Phys. Rev. B*, 100:094104, 2019.
- [147] Keith Powell, Liwei Li, Amirhassan Shams-Ansari, Jianfu Wang, Debin Meng, Neil Sinclair, Jiangdong Deng, Marko Lončar, and Xiaoke Yi. Integrated silicon carbide electro-optic modulator. *Nature Communications*, 13(1):1–7, 2022.
- [148] Marina Radulaski, Thomas M Babinec, Sonia Buckley, Armand Rundquist, J Provine, Kassem Alassaad, Gabriel Ferro, and Jelena Vučković. Photonic crystal cavities in cubic (3c) polytype silicon carbide films. *Optics express*, 21(26):32623–32629, 2013.
- [149] Marina Radulaski, Matthias Widmann, Matthias Niethammer, Jingyuan Linda Zhang, Sang-Yun Lee, Torsten Rendler, Konstantinos G. Lagoudakis, Nguyen Tien

- Son, Erik Janzén, Takeshi Ohshima, Jörg Wrachtrup, and Jelena Vučković. Scalable quantum photonics with single color centers in silicon carbide. *Nano Lett.*, 17(3):1782–1786, 2017.
- [150] Mouktik Raha, Songtao Chen, Christopher M Phenicie, Salim Ourari, Alan M Dibos, and Jeff D Thompson. Optical quantum nondemolition measurement of a single rare earth ion qubit. *Nature communications*, 11(1):1–6, 2020.
- [151] Mulpuri V Rao, J Tucker, OW Holland, N Papanicolaou, PH Chi, JW Kretchmer, and M Ghezzo. Donor ion-implantation doping into sic. *Journal of electronic materials*, 28(3):334–340, 1999.
- [152] Daniel Riedel, Immo Söllner, Brendan J Shields, Sebastian Starosielec, Patrick Appel, Elke Neu, Patrick Maletinsky, and Richard J Warburton. Deterministic enhancement of coherent photon generation from a nitrogen-vacancy center in ultrapure diamond. *Physical Review X*, 7(3):031040, 2017.
- [153] Lucio Robledo, Lilian Childress, Hannes Bernien, Bas Hensen, Paul FA Alkemade, and Ronald Hanson. High-fidelity projective read-out of a solid-state spin quantum register. *Nature*, 477(7366):574–578, 2011.
- [154] Alejandro Rodriguez, Marin Soljačić, J. D. Joannopoulos, and Steven G. Johnson.  $\chi(2)$  and  $\chi(3)$  harmonic generation at a critical power in inhomogeneous doubly resonant cavities. *Opt. Express*, 15(12):7303–7318, 2007.
- [155] Maximilian Ruf, Mark IJspeert, Suzanne Van Dam, Nick De Jong, Hans Van Den Berg, Guus Evers, and Ronald Hanson. Optically coherent nitrogen-vacancy centers in micrometer-thin etched diamond membranes. *Nano letters*, 19(6):3987–3992, 2019.
- [156] Alison E Rugar, Shahriar Aghaeimeibodi, Daniel Riedel, Constantin Dory, Haiyu Lu, Patrick J McQuade, Zhi-Xun Shen, Nicholas A Melosh, and Jelena Vučković. A quantum photonic interface for tin-vacancy centers in diamond. *Physical Review X*, 11:031021, 2021.

- [157] Alison E Rugar, Constantin Dory, Shahriar Aghaeimeibodi, Haiyu Lu, Shuo Sun, Sattwik Deb Mishra, Zhi-Xun Shen, Nicholas A Melosh, and Jelena Vučković. Narrow-linewidth tin-vacancy centers in a diamond waveguide. *ACS Photonics*, 7:2356–2361, 2020.
- [158] M Rühl, L Bergmann, M Krieger, and HB Weber. Stark tuning of the silicon vacancy in silicon carbide. *Nano Lett.*, 20(1):658, 2020.
- [159] Maximilian Rühl, Lena Bergmann, Michael Krieger, and Heiko B Weber. Stark tuning of the silicon vacancy in silicon carbide. *Nano Letters*, 2019.
- [160] Antonio Russo, Edwin Barnes, and Sophia E Economou. Photonic graph state generation from quantum dots and color centers for quantum communications. *Physical Review B*, 98(8):085303, 2018.
- [161] Neil V Sapra, Dries Vercauteren, Logan Su, Ki Youl Yang, Jinhie Skarda, Alexander Y Piggott, and Jelena Vučković. Inverse design and demonstration of broadband grating couplers. *IEEE Journal of Selected Topics in Quantum Electronics*, 25(3):1–7, 2019.
- [162] Hiroaki Sato, Makoto Abe, Ichiro Shoji, Jun Suda, and Takashi Kondo. Accurate measurements of second-order nonlinear optical coefficients of 6h and 4h silicon carbide. *JOSA B*, 26(10):1892–1896, 2009.
- [163] Michael Scheucher, Adèle Hilico, Elisa Will, Jürgen Volz, and Arno Rauschenbeutel. Quantum optical circulator controlled by a single chirally coupled atom. *Science*, 354(6319):1577–1580, 2016.
- [164] Ido Schwartz, Dan Cogan, Emma R Schmidgall, Yaroslav Don, Liron Gantz, Oded Kenneth, Netanel H Lindner, and David Gershoni. Deterministic generation of a cluster state of entangled photons. *Science*, 354(6311):434–437, 2016.
- [165] Z Shang, A Hashemi, Y Berencén, H-P Komsa, P Erhart, S Zhou, M Helm, AV Krasheninnikov, and GV Astakhov. Local vibrational modes of si vacancy spin qubits in sic. *Physical Review B*, 101(14):144109, 2020.

- [166] D Simin, F Fuchs, H Kraus, A Sperlich, PG Baranov, GV Astakhov, and V Dyakonov. High-precision angle-resolved magnetometry with uniaxial quantum centers in silicon carbide. *Physical Review Applied*, 4(1):014009, 2015.
- [167] D Simin, H Kraus, A Sperlich, T Ohshima, GV Astakhov, and V Dyakonov. Locking of electron spin coherence above 20 ms in natural silicon carbide. *Physical Review B*, 95(16):161201, 2017.
- [168] D Simin, VA Soltamov, AV Poshakinskiy, AN Anisimov, RA Babunts, DO Tolmachev, EN Mokhov, M Trupke, SA Tarasenko, A Sperlich, et al. All-optical dc nanotesla magnetometry using silicon vacancy fine structure in isotopically purified silicon carbide. *Physical Review X*, 6(3):031014, 2016.
- [169] PKJ Singaravelu, GCR Devarapu, Sebastian A Schulz, Quentin Wilmart, Stéphane Malhouitre, Ségolène Olivier, et al. Low-loss, compact, spot-size-converter based vertical couplers for photonic integrated circuits. *Journal of Physics D: Applied Physics*, 52(21):214001, 2019.
- [170] Alp Sipahigil, Ruffin E Evans, Denis D Sukachev, Michael J Burek, Johannes Borregaard, Mihir K Bhaskar, Christian T Nguyen, Jose L Pacheco, Haig A Atikian, Charles Meuwly, et al. An integrated diamond nanophotonics platform for quantum-optical networks. *Science*, 354(6314):847–850, 2016.
- [171] VA Soltamov, C Kasper, AV Poshakinskiy, AN Anisimov, EN Mokhov, A Sperlich, SA Tarasenko, PG Baranov, GV Astakhov, and V Dyakonov. Excitation and coherent control of spin qubit modes in silicon carbide at room temperature. *Nature communications*, 10(1):1–8, 2019.
- [172] VA Soltamov, BV Yavkin, DO Tolmachev, RA Babunts, AG Badalyan, V Yu Davydov, EN Mokhov, II Proskuryakov, SB Orlinskii, and PG Baranov. Optically addressable silicon vacancy-related spin centers in rhombic silicon carbide with high breakdown characteristics and endor evidence of their structure. *Physical review letters*, 115(24):247602, 2015.

- [173] Nguyen T Son, Christopher P Anderson, Alexandre Bourassa, Kevin C Miao, Charles Babin, Matthias Widmann, Matthias Niethammer, Jawad Ul Hassan, Naoya Morioka, Ivan G Ivanov, et al. Developing silicon carbide for quantum spintronics. *Applied Physics Letters*, 116(19):190501, 2020.
- [174] Bong-Shik Song, Takashi Asano, Seungwoo Jeon, Heungjoon Kim, Changxuan Chen, Dongyeon Daniel Kang, and Susumu Noda. Ultrahigh-q photonic crystal nanocavities based on 4h silicon carbide. *Optica*, 6(8):991–995, 2019.
- [175] Bong-Shik Song, Seungwoo Jeon, Heungjoon Kim, Dongyeon Daniel Kang, Takashi Asano, and Susumu Noda. High-q-factor nanobeam photonic crystal cavities in bulk silicon carbide. *Applied Physics Letters*, 113(23):231106, 2018.
- [176] Bong-Shik Song, Shota Yamada, Takashi Asano, and Susumu Noda. Demonstration of two-dimensional photonic crystals based on silicon carbide. *Optics express*, 19(12):11084–11089, 2011.
- [177] E Sörman, NT Son, WM Chen, O Kordina, Christer Hallin, and Erik Janzén. Silicon vacancy related defect in 4h and 6h sic. *Physical Review B*, 61(4):2613, 2000.
- [178] ÖO Soykal, Pratibha Dev, and Sophia E Economou. Silicon vacancy center in 4 h-sic: Electronic structure and spin-photon interfaces. *Physical Review B*, 93(8):081207, 2016.
- [179] ÖO Soykal and Thomas L Reinecke. Quantum metrology with a single spin-3 2 defect in silicon carbide. *Phys. Rev. B*, 95(8):081405, 2017.
- [180] Lukas Spindlberger, András Csóré, Gergő Thiering, S Putz, Robin Karhu, J Ul Hassan, NT Son, T Fromherz, A Gali, and M Trupke. Optical properties of vanadium in 4h silicon carbide for quantum technology. *Physical Review Applied*, 12(1):014015, 2019.
- [181] Brian Stern, Xingchen Ji, Yoshitomo Okawachi, Alexander L Gaeta, and Michal Lipson. Battery-operated integrated frequency comb generator. *Nature*, 562(7727):401–405, 2018.

- [182] Logan Su, Dries Vercrusse, Jinhie Skarda, Neil V Sapra, Jan A Petykiewicz, and Jelena Vučković. Nanophotonic inverse design with spins: Software architecture and practical considerations. *Applied Physics Reviews*, 7(1):011407, 2020.
- [183] Denis D Sukachev, Alp Sipahigil, Christian T Nguyen, Mihir K Bhaskar, Ruffin E Evans, Fedor Jelezko, and Mikhail D Lukin. Silicon-vacancy spin qubit in diamond: a quantum memory exceeding 10 ms with single-shot state readout. *Physical review letters*, 119(22):223602, 2017.
- [184] Shuo Sun, Jingyuan Linda Zhang, Kevin A Fischer, Michael J Burek, Constantin Dory, Konstantinos G Lagoudakis, Yan-Kai Tzeng, Marina Radulaski, Yousif Kelaita, Amir Safavi-Naeini, et al. Cavity-enhanced raman emission from a single color center in a solid. *Physical review letters*, 121(8):083601, 2018.
- [185] Ph Tamarat, T Gaebel, JR Rabeau, M Khan, AD Greentree, H Wilson, LCL Hollenberg, S Prawer, P Hemmer, F Jelezko, et al. Stark shift control of single optical centers in diamond. *Phys. Rev. Lett.*, 97(8):083002, 2006.
- [186] Natasha Tomm, Alisa Javadi, Nadia O Antoniadis, Daniel Najer, Matthias C Löbl, Alexander R Korsch, Rüdiger Schott, Sascha R Valentin, Andreas D Wieck, Arne Ludwig, et al. A bright and fast source of coherent single photons. *arXiv preprint arXiv:2007.12654*, 2020.
- [187] Toan Trong Tran, Carlo Bradac, Alexander S Solntsev, Milos Toth, and Igor Aharonovich. Suppression of spectral diffusion by anti-stokes excitation of quantum emitters in hexagonal boron nitride. *Applied Physics Letters*, 115(7):071102, 2019.
- [188] Rahul Trivedi, Daniil Lukin, and Jelena Vuckovic. Quantum optics and nonclassical light generation. In *Nanoscale Quantum Optics*, pages 29–76. IOS Press, 2020.
- [189] Rahul Trivedi, Marina Radulaski, Kevin A Fischer, Shanhui Fan, and Jelena Vučković. Photon blockade in weakly driven cavity quantum electrodynamics systems with many emitters. *Phys. Rev. Lett.*, 122(24):243602, 2019.

- [190] Péter Udvarhelyi, Roland Nagy, Florian Kaiser, Sang-Yun Lee, Jörg Wrachtrup, and Adam Gali. Spectrally stable defect qubits with no inversion symmetry for robust spin-to-photon interface. *Physical Review Applied*, 11(4):044022, 2019.
- [191] Péter Udvarhelyi, Gergő Thiering, Naoya Morioka, Charles Babin, Florian Kaiser, Daniil Lukin, Takeshi Ohshima, Jawad Ul-Hassan, Nguyen Tien Son, Jelena Vučković, et al. Vibronic states and their effect on the temperature and strain dependence of silicon-vacancy qubits in 4 h-si c. *Physical Review Applied*, 13(5):054017, 2020.
- [192] Rui Vasconcelos, Sarah Reisenbauer, Cameron Salter, Georg Wachter, Daniel Wirtitsch, Jörg Schmiedmayer, Philip Walther, and Michael Trupke. Scalable spin-photon entanglement by time-to-polarization conversion. *npj Quantum Information*, 6(1):1–5, 2020.
- [193] Dries Vercauteren, Neil V Sapra, Logan Su, and Jelena Vuckovic. Dispersion engineering with photonic inverse design. *IEEE Journal of Selected Topics in Quantum Electronics*, 26(2):1–6, 2019.
- [194] HJ Von Bardeleben, JL Cantin, A Csóré, A Gali, E Rauls, and U Gerstmann. Nv centers in 3 c, 4 h, and 6 h silicon carbide: A variable platform for solid-state qubits and nanosensors. *Physical Review B*, 94(12):121202, 2016.
- [195] Edo Waks and Jelena Vuckovic. Dipole induced transparency in drop-filter cavity-waveguide systems. *Physical review letters*, 96(15):153601, 2006.
- [196] Noel H Wan, Tsung-Ju Lu, Kevin C Chen, Michael P Walsh, Matthew E Trusheim, Lorenzo De Santis, Eric A Bersin, Isaac B Harris, Sara L Mouradian, Ian R Christen, et al. Large-scale integration of artificial atoms in hybrid photonic circuits. *Nature*, 583(7815):226–231, 2020.
- [197] Cheng Wang, Mian Zhang, Xi Chen, Maxime Bertrand, Amirhassan Shams-Ansari, Sethumadhavan Chandrasekhar, Peter Winzer, and Marko Lončar. Integrated lithium niobate electro-optic modulators operating at cmos-compatible voltages. *Nature*, 562(7725):101–104, 2018.

- [198] Chengli Wang, Zhiwei Fang, Ailun Yi, Bingcheng Yang, Zhe Wang, Liping Zhou, Chen Shen, Yifan Zhu, Yuan Zhou, Rui Bao, et al. High-q microresonators on 4h-silicon-carbide-on-insulator platform for nonlinear photonics. *Light: Science & Applications*, 10(1):1–11, 2021.
- [199] Jianwei Wang, Fabio Sciarrino, Anthony Laing, and Mark G Thompson. Integrated photonic quantum technologies. *Nature Photonics*, pages 1–12, 2019.
- [200] Jun-Feng Wang, Fei-Fei Yan, Qiang Li, Zheng-Hao Liu, He Liu, Guo-Ping Guo, Li-Ping Guo, Xiong Zhou, Jin-Ming Cui, Jian Wang, et al. Coherent control of nitrogen-vacancy center spins in silicon carbide at room temperature. *Physical Review Letters*, 124(22):223601, 2020.
- [201] Junfeng Wang, Yu Zhou, Xiaoming Zhang, Fucui Liu, Yan Li, Ke Li, Zheng Liu, Guanzhong Wang, and Weibo Gao. Efficient generation of an array of single silicon-vacancy defects in silicon carbide. *Physical Review Applied*, 7(6):064021, 2017.
- [202] Shunchong Wang, Minjie Zhan, Gang Wang, Hongwen Xuan, Wei Zhang, Chunjun Liu, Chunhua Xu, Yu Liu, Zhiyi Wei, and Xiaolong Chen. 4h-sic: a new nonlinear material for midinfrared lasers. *Laser & Photonics Reviews*, 7(5):831–838, 2013.
- [203] Naoki Watanabe, Tsunenobu Kimoto, and Jun Suda. Thermo-optic coefficients of 4h-sic, gan, and aln for ultraviolet to infrared regions up to 500° c. *Japanese Journal of Applied Physics*, 51(11R):112101, 2012.
- [204] Rusheng Wei, Sheng Song, Kun Yang, Yingxin Cui, Yan Peng, Xiufang Chen, Xiaobo Hu, and Xiangang Xu. Thermal conductivity of 4h-sic single crystals. *Journal of Applied Physics*, 113(5):053503, 2013.
- [205] Samuel J Whiteley, Gary Wolfowicz, Christopher P Anderson, Alexandre Bourassa, He Ma, Meng Ye, Gerwin Koolstra, Kevin J Satzinger, Martin V Holt, F Joseph Heremans, et al. Spin-phonon interactions in silicon carbide addressed by gaussian acoustics. *Nature Physics*, 15(5):490–495, 2019.

- [206] M. Widmann, S.Y. Lee, T. Rendler, N. T. Son, H. Fedder, S. Paik, L.P. Yang, N. Zhao, S. Yang, I. Booker, A. Denisenko, M. Jamali, S.A. Momenzadeh, I. Gerhardt, T. Ohshima, A. Gali, E. Janzen, and J. Wrachtrup. Coherent control of single spins in silicon carbide at room temperature. *Nature Materials*, 14:164–168, 2015.
- [207] Matthias Widmann, Sang-Yun Lee, Torsten Rendler, Nguyen Tien Son, Helmut Fedder, Seoyoung Paik, Li-Ping Yang, Nan Zhao, Sen Yang, Ian Booker, et al. Coherent control of single spins in silicon carbide at room temperature. *Nature materials*, 14(2):164–168, 2015.
- [208] Matthias Widmann, Matthias Niethammer, Dmitry Yu Fedyanin, Igor A Khramtsov, Torsten Rendler, Ian D Booker, Jawad Ul Hassan, Naoya Morioka, Yu-Chen Chen, Ivan G Ivanov, et al. Electrical charge state manipulation of single silicon vacancies in a silicon carbide quantum optoelectronic device. *Nano letters*, 19(10):7173–7180, 2019.
- [209] Gary Wolfowicz, Christopher P Anderson, Berk Diler, Oleg G Poluektov, F Joseph Heremans, and David D Awschalom. Vanadium spin qubits as telecom quantum emitters in silicon carbide. *arXiv preprint arXiv:1908.09817*, 2019.
- [210] Xiaoxiao Xue, Yi Xuan, Yang Liu, Pei-Hsun Wang, Steven Chen, Jian Wang, Dan E Leaird, Minghao Qi, and Andrew M Weiner. Mode-locked dark pulse kerr combs in normal-dispersion microresonators. *Nature Photonics*, 9(9):594, 2015.
- [211] Shota Yamada, Bong-Shik Song, Seungwoo Jeon, Jeremy Upham, Yoshinori Tanaka, Takashi Asano, and Susumu Noda. Second-harmonic generation in a silicon-carbide-based photonic crystal nanocavity. *Optics letters*, 39(7):1768–1771, 2014.
- [212] Ki Youl Yang, Dong Yoon Oh, Seung Hoon Lee, Qi-Fan Yang, Xu Yi, Boqiang Shen, Heming Wang, and Kerry Vahala. Bridging ultrahigh-q devices and photonic circuits. *Nature Photonics*, 12(5):297–302, 2018.
- [213] Xiaodong Yang, Charlton J Chen, Chad A Husko, and Chee Wei Wong. Digital resonance tuning of high-q/ v m silicon photonic crystal nanocavities by atomic layer deposition. *Applied Physics Letters*, 91(16):161114, 2007.

- [214] Winnie N. Ye and Yule Xiong. Review of silicon photonics: history and recent advances. *J. Mod. Opt.*, 60(16):1299–1320, 2013.
- [215] Ailun Yi, Yi Zheng, Hao Huang, Jiajie Lin, Youquan Yan, Tianguai You, Kai Huang, Shibin Zhang, Chen Shen, Min Zhou, et al. Wafer-scale 4h-silicon carbide-on-insulator (4h-sic) platform for nonlinear integrated optical devices. *Optical Materials*, page 109990, 2020.
- [216] Xu Yi, Qi-Fan Yang, Ki Youl Yang, Myoung-Gyun Suh, and Kerry Vahala. Soliton frequency comb at microwave rates in a high-q silica microresonator. *Optica*, 2(12):1078–1085, 2015.
- [217] Xu Yi, Qi-Fan Yang, Ki Youl Yang, and Kerry Vahala. Active capture and stabilization of temporal solitons in microresonators. *Optics Letters*, 41(9):2037–2040, 2016.
- [218] SA Zargaleh, B Eble, S Hameau, J-L Cantin, L Legrand, M Bernard, F Margailan, J-S Lauret, J-F Roch, HJ Von Bardeleben, et al. Evidence for near-infrared photoluminescence of nitrogen vacancy centers in 4 h-sic. *Physical Review B*, 94(6):060102, 2016.
- [219] Soroush Abbasi Zargaleh, Sophie Hameau, Benoit Eble, F Margailan, Hans Jürgen von Bardeleben, Jean-Louis Cantin, and Weibo Gao. Nitrogen vacancy center in cubic silicon carbide: A promising qubit in the 1.5  $\mu$  m spectral range for photonic quantum networks. *Physical Review B*, 98(16):165203, 2018.
- [220] Jiehang Zhang, Guido Pagano, Paul W Hess, Antonis Kyprianidis, Patrick Becker, Harvey Kaplan, Alexey V Gorshkov, Z-X Gong, and Christopher Monroe. Observation of a many-body dynamical phase transition with a 53-qubit quantum simulator. *Nature*, 551(7682):601–604, 2017.
- [221] Jingyuan Linda Zhang, Shuo Sun, Michael J Burek, Constantin Dory, Yan-Kai Tzeng, Kevin A Fischer, Yousif Kelaita, Konstantinos G Lagoudakis, Marina Radulaski, Zhi-Xun Shen, et al. Strongly cavity-enhanced spontaneous emission from silicon-vacancy centers in diamond. *Nano Letters*, 18(2):1360–1365, 2018.

- [222] Yong Zhang and Jianwei Wang. Bound exciton model for an acceptor in a semiconductor. *Phys. Rev. B*, 90:155201, Oct 2014.
- [223] Yi Zheng, Mihao Pu, Ailun Yi, Xin Ou, and Haiyan Ou. 4H-SiC microring resonators for nonlinear integrated photonics. *Optics Letters*, 44:5784–5787, 2019.
- [224] Yi Zheng, Minhao Pu, Ailun Yi, Bingdong Chang, Tiangui You, Kai Huang, Ayman N Kamel, Martin R Henriksen, Asbjørn A Jørgensen, Xin Ou, et al. High-quality factor, high-confinement microring resonators in 4h-silicon carbide-on-insulator. *Optics express*, 27(9):13053–13060, 2019.
- [225] Manjin Zhong, Morgan P Hedges, Rose L Ahlefeldt, John G Bartholomew, Sarah E Beavan, Sven M Wittig, Jevon J Longdell, and Matthew J Sellars. Optically addressable nuclear spins in a solid with a six-hour coherence time. *Nature*, 517(7533):177–180, 2015.
- [226] Tian Zhong, Jonathan M Kindem, John G Bartholomew, Jake Rochman, Ioana Craiciu, Evan Miyazono, Marco Bettinelli, Enrico Cavalli, Varun Verma, Sae Woo Nam, et al. Nanophotonic rare-earth quantum memory with optically controlled retrieval. *Science*, 357(6358):1392–1395, 2017.
- [227] James F. Ziegler, M. D. Ziegler, and J. P. Biersack. SRIM - The stopping and range of ions in matter. *Nucl. Instrum. Methods Phys. Res. B*, 268(11-12):1818–1823, 2010.